Development of dielectric multilayer coatings for ultrafast oscillators

Elena Fedulova

München 2016

Development of dielectric multilayer coatings for ultrafast oscillators

Elena Fedulova

Dissertation
an der Physik
der Ludwig–Maximilians–Universität
München

vorgelegt von
Elena Fedulova
aus Protvino, Russland

München, den 21.06.2016

Erstgutachter: Prof. Dr. Ferenc Krausz
Zweitgutachter: Prof. Dr. Jörg Schreiber
Tag der mündlichen Prüfung: 27.09.2016

Whatever may be their use in civilized societies, mirrors are essential to all violent and heroic action.

Virginia Woolf, “A Room of One’s Own”

Zusammenfassung

Laser ermöglichten unter anderem die Untersuchung der molekularen Dynamik auf ultrakurzen Zeitskalen sowie die hochpräzise Mikrostrukturierung im Maschinenbau und in der Zahnmedizin und helfen die Grenzen der sich dynamisch entwickelnden Disziplinen in der Wissenschaft ultrakurzer Prozesse und der Industrie zu erweitern. Derzeit ist das gemeinsame Streben vieler Forschungsgruppen die Skalierung von passiv modengekoppelten Femtosekunden-Oszillatoren zu höchstmöglichen Intensitäten, möglichst kurzen Pulsdauern und hohen Wiederholungsraten bei gleichzeitig stabiler Leistung. Aufgrund der Skalierbarkeit der Leistung kann die Yb:YAG Scheibenlaser-Technologie die Grundlage für die nächste Generation der Femtosekunden-Laseroszillatoren werden. Eine Schlüsselkomponente zur Verbesserung von Scheibenlasersystemen sind speziell entwickelte dielektrische Beschichtungen, die gegenwärtig bereits in eine große Anzahl von Ultrakurzpulslasersystemen integriert sind.

Auf der einen Seite erfordert die Skalierung von Laseroszillatoren zu immer höheren Pulsenergien, Spitzenleistungen und Wiederholungsraten immer höhere negative Gruppengeschwindigkeitssdispersionen im Resonator. Des Weiteren hängt die Erzeugung von kürzeren Pulsen und der Hochleistungsbetrieb von breitbandigen hochdispersiven Spiegeln ab, welche geringe optische Verluste, eine hohe laserindzierte Zerstörschwelle und minimale thermische Effekte besitzen. Diese Arbeit zielt auf die Entwicklung von präzise hergestellten dispersiven Beschichtungen mit den angegebenen Eigenschaften ab. Auch werden zusätzlich mehrere Substratmaterialien untersucht, welche die resonatorinternen thermischen Effekte reduzieren. Zuerst wird ein hochdispersiver Spiegel mit extrem hoher Gruppengeschwindigkeitsdispersion von $-10\,000$ fs^2 vorgestellt. Dieser Spiegel wurde erfolgreich in einem modengekoppelten Yb:YAG-Festkörperoszillator eingesetzt: er liefert 320-fs-Impulse mit einer mittleren Leistung von etwa 4 W, bei gleich gutem Oszillatorverhalten im Vergleich zu einem hochdispersiven Spiegel mit -3000 fs^2.

Auf der anderen Seite sind neue Quellen von Nichtlinearitäten erforderlich um eine stabile Modenkopplung bei ultraschnellen Oszillatoren zu erreichen, welche die Einschränkungen der derzeit existierenden Ansätze überwinden. Der optische

Kerr-Effekt, dies ist die intensitätsabhängige Änderung des Brechungsindex, ist unverzichtbar in Ultrakurzpulslasern und hat so zum Beispiel die Modenkopplung von Lasern und deren spektrale Verbreiterung in den Single-Cycle-Regime der Pulsdauer ermöglicht. Jedoch sind die nicht-linearen Materialien welche für ultraschnelle Laseranwendungen geeignet sind begrenzt. Somit ist ein weiteres Ziel dieser Arbeit die Berechnung und Realisierung von mehrschichtigen dielektrischen Strukturen mit schichtspezifischen Kerr-Nichtlinearitäten. Dadurch können intensitätsabhängige Effekte über spezielle mehrlagige Interferenzbeschichtung angepasst werden. Als Beispiel werden dielektrische nichtlineare Spiegel mit zunehmendem Reflexionsvermögen bei zunehmender Laserintensität demonstriert, welche für die Modenkopplung geeignet sind. Mit einem Pump-Probe Experiment wird gezeigt, dass die Erholungszeit der Kerr-Effekt basierenden Nicht-Linearität schneller ist als die Einhüllende des Laserpulses von 1 ps. Aufgrund ihrer Flexibilität im Design, haben die nichtlinearen mehrlagigen Beschichtungen das Potenzial, bisher ungeahnte Möglichkeiten in der nichtlinearen Optik und im Kurzpulslaserdesign zu ermöglichen.

Die Entwicklung hochdispersiver Spiegel und nichtlinearer, mehrlagiger Beschichtungen erlaubt die Weiterentwicklung ultraschneller modengekoppelter Oszillatoren, insbesondere Yb:YAG-Oszillatoren, hin zu neuen Generationen.

Abstract

Ultrafast laser oscillators have enabled investigation of molecular dynamics at ultrashort time scales, allowed high-precision microstructuring in machinery as well as in dentistry and proceed pushing the limits of dynamically developing disciplines of ultrafst science and industry. Currently, the joint aspiration of many research groups is directed at scaling passively-mode-locked femtosecond oscillators to the highest possible intensities, shortest possible pulse durations and highest possible repetition rates, demonstrating stable performance. Due to its power scalability, thin-disk technology, which most frequently uses Yb:YAG gain medium, may constitute the basis for next-generation femtosecond laser oscillators. The universal key capable of enhancing the possibilities of ultrafast thin-disk laser systems is dielectric multilayer coatings, presently integrated into a great number of laser systems.

On one hand, scaling ultrafast laser oscillators to ever higher pulse energies, peak powers and repetition rates requires ever higher negative group delay dispersion in the cavity. Furthermore, generation of shorter pulses and high-power operation depends on broadband HDMs with low losses, large laser-induced breakdown threshold and minimal thermal effects. This work is aimed at the development of precisely engineered dispersive coatings with the specified properties, additionally considering several substrate materials reducing intracavity thermal effects. Firstly, a highly-dispersive mirror possessing an extremely high group delay dispersion of $-10\ 000\ \mathrm{fs}^2$ is presented. This mirror is demonstrated to successfully operate in a mode-locked Yb:YAG solid-state oscillator, delivering 320-fs pulses with an average power of about 4 W, revealing no degradation in the oscillator behavior compared to a highly-dispersive mirror with $-3000\ \mathrm{fs}^2$.

On the other hand, new sources of nonlinearity are required to achieve stable mode-locking of the ultrafast oscillators, which would allow to overcome the limitations of the currently existing approaches. The optical Kerr effect, i.e. the intensity-dependent change of refractive index, is ubiquitous in ultrafast science and has, for example, enabled the mode-locking of lasers and their spectral broadening into the single-cycle regime of pulse duration. However, the nonlinear ma-

terials suitable for ultrafast laser applications are limited. Thus, another aim of this work is designing and realization of multilayer dielectric optical structures with layer-specific Kerr nonlinearities, which permit tailoring of the intensity-dependent effects. As an example, dielectric nonlinear multilayer coatings with increasing reflectance at increasing laser intensity are demonstrated, which are in principle suitable for mode-locking. By means of thorough diverse characterization, it is shown that the nonlinearity is based on the optical Kerr effect, with the recovery time faster than the laser pulse envelope of 1 ps. Due to high flexibility in design, the presented dielectric nonlinear multilayer coatings have the potential to open hitherto unprecedented possibilities in nonlinear optics and ultrafast laser applications.

Developing highly-dispersive mirrors and nonlinear multilayer coatings allow for advancement of the ultrafast mode-locked oscillators, Yb:YAG oscillators in particular, to a new level.

Contents

List of Figures

List of abbreviations

2PA	Two-photon absorption
ACF	Autocorrelation function
AFM	Atomic force microscope
AOI	Angle of incidence
BBM	Broadband monitoring
CB	Conduction band
CCD	Charge-coupled device
CM	Chirped mirror
CPA	Chirped pulse amplification
CTE	Coefficient of thermal expansion
CVD	Chemical vapor deposition
CW	Continuous wave
DM	Dispersive mirror
FS	Fused silica
FWHM	Full width at half maximum
GD	Group delay
GDD	Group delay dispersion
GTI	Gires-Tournois interferometer
GVD	Group velocity dispersion

HDM	Highly-dispersive mirror
HR	Highly-reflective [mirror]
IBS	Ion-beam sputtering
KLM	Kerr-lens mode-locking
LIDT	Laser-induced damage threshold
MAM	Multilayer amplitude modulator
MPA	Multi-photon absorption
NIR	Near-infrared [radiation]
NMC	Nonlinear multilayer coating
OC	Output coupler
OPCPA	Optical parametric chirped-pulse amplification
PD	Photodiode
PVD	Physical vapor deposition
QWS	Quarter wave stack
rms	Root mean square
ROC	Radius of curvature
SAM	Self-amplitude modulation
SESAM	Semiconductor saturable absorber mirror
SPM	Self-phase modulation
STE	Self-trapped exciton
TD	Thin disk
TIS	Total integrated scatter
TL	Total losses

TOD	Third order dispersion
TOL	Total optical loss
UV	Ultraviolet [radiation]
VB	Valence band
vis	Visible [radiation]
WLI	White light interferometer
XUV	Extreme violet [radiation]

Chapter 1

Introduction

1.1 Motivation

Lasers generating ultrashort light pulses have become a substantial part of the modern scientific, as well as daily, life. The diverse range of ultrafast laser applications spans from new-level imaging techniques [1] to material processing with unprecedented precision [2–4], from time-resolved spectroscopy [5] to highly delicate surgeries in ophthalmology [6] and neurology [7,8]. Furthermore, ultrashort pulses are a unique tool in the research fields of femtochemistry [9, 10], high-resolution spectroscopy [11,12] with extreme ultraviolet (XUV) frequency combs [13,14] and the rapidly developing field of attosecond science [15–18]. More specifically, a closer insight into the microcosm has been evinced due to the ability to trail ultrafast relaxation processes on strikingly short time scales [19–22]. By the same token, ultrashort light pulses have empowered studies of light-matter interactions in tremendously intense laser fields, never achieved previously [23–25]. Advancing laser technology to ever shorter pulses, ever higher repetition rates, ever higher intensities, and ever higher peak as well as average powers holds promise for further pioneering scientific studies together with new industrial applications.

The discovery of laser mode-locking in 1964 [26,27] sparked the development of ultrafast optics. Further on, the breakthrough of Kerr-lens mode-locking (KLM) [28] has brought ultrafast laser technology to a completely different level, making the generation of stable sub-10-fs pulses with peak powers surpassing 3 MW directly from a Ti:sapphire (emission wavelength around 800 nm) laser oscillator feasible [29]. These revolutionary values were achieved by virtue of dispersive dielectric multilayer mirrors (DMs) [30]. The design of the layer sequence enables a highly flexible control of the linear optical properties, such as reflectance, bandwidth, phase and dispersion. Generally speaking, dielectric multilayer coatings, widely exploited in ultrafast laser systems, have played an increasingly important

role in the progress of ultrafast science. High-power lasers, for example, heavily rely on highly-reflective (HR) mirrors. DMs have become indispensable for dispersion control [29, 31–33]. Moreover, DMs have permitted not only the synthesis of subcycle light transients [34, 35], but also shaping the waveform within the wave cycle [22, 36]. Broadband DMs allow for chirp compensation with multiple degrees of freedom, making pulse compression of intense light at sub-terawatt power levels down to 4 fs possible [37]. Multilayer coatings designed for the XUV and soft-X-ray spectral ranges [38–41] are extremely important for attosecond pulse generation [15, 42–44]. Specially tailored multilayer coatings [45, 46] are of great significance for newly arising challenges in developing nonlinear science.

At the same time, femtosecond pulse generation has been developing, seeking for new approaches along with new gain media to enhance pulse characteristics. Third-generation femtosecond technology [47] is currently emerging from a combination of optical parametric chirped-pulse amplification (OPCPA) [48] and pulses with terawatt peak powers from Yb-doped solid-state lasers at kilowatt average powers. Operation of solid-state KLM oscillators comprising the broad gain bandwidth (600−1000 nm) Ti:sapphire active medium [28, 49], in which the shortest (to date) pulses have been generated directly from a laser [50], is technically troublesome in the regime of high average powers and high energy pulses (multi μJ). High-power operation in KLM oscillators is easier to achieve with Yb-doped thin disk (TD concept introduced by Gisesen et al. [51]) technology [52]. In spite of its limited gain bandwidth of about 9 nm [52], the gain material Yb:YAG (emission wavelength around 1030 nm) has been well developed and acquired a prominent position among other TD gain materials [53] due to its excellent power scaling properties [54]. In particular, the Yb:YAG oscillators employed in this work, are at the front edge of the third-generation femtosecond technology.

Regardless of which type of laser technology is employed, high-power femtosecond oscillators have several common requirements. HR and focusing mirrors are necessary to compose the resonators themselves. State-of-the-art laser oscillators rely on two basic effects: a passive amplitude nonlinearity (Kerr-lensing effect, at present) and large amount of negative dispersion. As mirrors are essential to all laser oscillators, the integration of both these effects into mirrors would offer the most compact and advanced implementation of mode-locking. Steps towards compact laser cavities have already been undertaken, and resulted in wide utilization of DMs [30] for dispersion manipulation [29, 31–33]. The next ambitious step is to combine both large dispersion and nonlinearities in mirrors, which represents the global goal of this thesis.

Pursuing one of the specified goals, highly-dispersive mirrors (HDMs) introducing extremely high negative dispersion levels are developed in this work. Higher levels of dispersion in the cavity permit scaling TD ultrafast laser oscillators to higher energies and repetition rates. Including more dispersion by simply increasing the number of bounces off DMs in the cavity leads to the growth of round-trip losses and overall alignment complications. Simultaneously, it is important to take thermal effects into account, likely to arise for high-power third-generation femtosecond technology, and find an optimum dispersion to thermal effects ratio per bounce. To this end, reducing the electrical field inside the multilayer mirrors may bring positive results. Additionally, different substrate materials, allowing heat extraction away from the HDMs, is the first approach considered in this work.

While being made use of in the field of nonlinear optics, dielectric multilayer coatings themselves primarily operate in the linear regime. Typically, efforts are taken to avoid the manifestation of nonlinear effects in the optical elements. For optics implemented in laser oscillators, third harmonics, multiphoton absorption (MPA) or any other losses are commonly considered parasitic as many applications require lossless elements. However, it is possible to exploit nonlinearities in order to create a nearly-lossless device. Thus, the second goal of this thesis is to develop nearly-lossless optical elements as a result of a merger between nonlinear and multilayer optics. These nonlinear elements would need to demonstrate higher reflectance at higher intensities in the cavity – behavior, that can be provided by the optical Kerr effect. The optical Kerr effect is a quasi-instantaneous nonlinear optical phenomenon which results in an intensity-dependent refractive index. Adopting the optical Kerr effect for laser technology has led to various applications, among which are the ultrafast light gate [55], the KLM technique [28], near at hand light modulators presented here and may potentially lead to optical-to-optical computers. However, the selection of nonlinear materials applicable for ultrafast lasers is limited. The specially designed multilayer dielectric coatings presented here possess layer-specific Kerr nonlinearities, which allow the tailoring of intensity-dependent effects. Particularly, the reflectance of such nonlinear multilayer coatings (NMCs) increases with increasing intensity, demonstrating a nonlinear response dominated by the optical Kerr effect. This result shows that it is generally feasible to create lossless elements based on NMCs with desirable properties for future ultrafast applications.

Coating technology [56], creating versatile components for laser oscillators, is a silver bullet for the aforementioned challenges: It can provide not only high negative dispersion levels but can also serve as a nonlinearity source. Existing

in many facilities around the world, coating machines allow for the production of dense layers with excellent homogeneity, high reproducibility and high stability with respect to the environmental conditions, as well as rapid manufacturing and relatively cheap deposition (in the case of magnetron beam sputtering, for example) [57–60]. Developing laser elements based on a combination of linear and nonlinear dielectric multilayer coatings by means of conventional coating techniques may become a turning point for a vast number of laser applications.

1.2 Thesis outline

This thesis is structured as follows: Chapter 2 presents the fundamental optical effects that occur in ultrafast oscillators, including dispersion, the optical Kerr effect and the processes it causes, and the basics of mode-locking. Chapter 3 concludes the introductory part of the thesis and introduces a review of the theoretical approaches to the design of multilayer coatings, existing coating and layer thickness control techniques, as well as the available characterization methods. Chapter 4 introduces the basic principles of dispersive mirrors and further deals with dispersive dielectric multilayer mirrors, analyzing several substrate materials in order to avoid thermal effects inside oscillators operated at high powers, and demonstrating unprecedented levels of dispersion of HDMs. Chapter 5 introduces the idea of applying the optical Kerr effect to multilayer dielectric coatings along with its experimental realization. This chapter demonstrates that the optical coatings can be utilized as a fount of nonlinearity in laser oscillators. Chapter 6 discusses the potential, as well as executed, applications arising from exploiting the optical Kerr effect in multilayer coatings. One of the most thrilling possible prospects is various mode-locking applications. Finally, chapter 7 concludes the thesis and provides an outlook towards the further advancement of multilayer coatings for ultrafast laser oscillators.

Chapter 2

Optical processes in ultrafast oscillators

This chapter is devoted to the basic theoretical principles of the optical processes taking place in ultrafast laser oscillators. In order to create the optics advancing laser systems, it is important to understand how an ultrashort optical pulse propagates through dispersive media contained within the oscillators, such as various laser crystals, glasses and air, which is discussed in section 2.1. A closer insight into the optical Kerr effect, which plays an important role in ultrafast science, is given in section 2.2, followed by the processes resulting from this nonlinear physical phenomenon (section 2.3). Section 2.4 discusses the basics of the mode-locking in general, followed by the fundamental principles of Kerr-lens mode-locking technique, which has recently acquired a great importance.

2.1 Ultrashort pulse propagation and dispersion

The Maxwell wave equation for an isotropic, either linear or nonlinear, medium describes the propagation of an optical pulse through this medium and is given by (ref. [61], p. 566):

$$\left(\frac{\partial^2}{\partial x^2}+\frac{\partial^2}{\partial y^2}+\frac{\partial^2}{\partial z^2}-\frac{1}{c^2}\frac{\partial^2}{\partial t^2}\right)\vec{E}(x,\,y,\,z,\,t)=\frac{1}{\epsilon_0 c^2}\frac{\partial^2}{\partial t^2}\vec{P}(x,\,y,\,z,\,t)\,, \tag{2.1}$$

where $\vec{E}$ is the strength of the electromagnetic field, c is the speed of light and ϵ_0 is the permittivity of free space. Microscopic dipoles aligned with the electric field cause the emergence of the electric dipole moment per unit volume inside the material. This response of the medium is characterized by the electric polarization

$\vec{P}$. Considering a linearly polarized electric field propagating in the z-direction, along with a transfer into the frequency domain through Fourier transformation, allows one to simplify equation 2.1:

$$\left(\frac{\partial^2}{\partial z^2} + \frac{1}{\epsilon_0 c^2}\omega^2 \epsilon(\omega)\right) \tilde{E}(\omega,\, z) = 0\,. \tag{2.2}$$

The complex representation $\tilde{E}$ of the electric field amplitude is convenient to use as its real part yields the measurable electric field. A solution of this reduced wave equation is the Gaussian pulse represented as:

$$\tilde{E}(\omega,\, z) = \tilde{E}(\omega, 0)\, e^{-ik(\omega)z}, \tag{2.3}$$

with the frequency-dependent propagation constant $k\,(\omega) = \frac{\omega}{c} n(\omega)$, determined by the frequency-dependent refractive index of the medium $n(\omega)$ and the angular frequency ω. Propagation in the dispersive medium with a thickness l, an optical pulse acquires a spectral phase:

$$\varphi(\omega,\, z) = k\,(\omega) \times l = \frac{\omega}{c} n\,(\omega) \times l\,. \tag{2.4}$$

The propagation constant $k\,(\omega)$ can be defined by the truncated Taylor series expansion around the central frequency ω_0:

$$k\,(\omega) = k_0 + \underbrace{\frac{\partial k}{\partial \omega}\,|_{\omega_0}}_{\text{GD}}(\omega - \omega_0) + \frac{1}{2}\underbrace{\frac{\partial^2 k}{\partial \omega^2}\,|_{\omega_0}}_{\text{GVD}}(\omega - \omega_0)^2 + \frac{1}{6}\underbrace{\frac{\partial^3 k}{\partial \omega^3}\,|_{\omega_0}}_{\text{TOD}}(\omega - \omega_0)^3 \ldots \tag{2.5}$$

with a constant phase shift $k_0 = \frac{n_0 \omega_0}{c}$. Different order terms in equation 2.5 affect the pulse shape, each in a different manner. The inverse group velocity $\frac{\partial k}{\partial \omega}\,|_{\omega_0} \equiv \frac{1}{\nu_g(\omega_0)}$ describes an overall time delay without affecting the pulse shape – termed group delay (GD). The quadratic term, causing a symmetric temporal broadening of the pulse, can be viewed as the group velocity dispersion (GVD):

$$\text{GVD} = \frac{\partial^2 k}{\partial \omega^2}\,|_{\omega_0} \equiv \frac{\partial}{\partial \omega}\left[\frac{1}{v_g(\omega)}\right]_{\omega_0} = -\frac{1}{v_g^2}\frac{\partial v_g}{\partial \omega}\,|_{\omega_0}\,, \tag{2.6}$$

usually given in fs^2/mm and is a term of interest. Dispersion is of crucial importance for ultrashort pulses generation. The dependence of the group velocity on the wave frequency leads to optical pulse broadening as different spectral parts propagate with different group velocities in the dispersive medium (figure 2.1). This

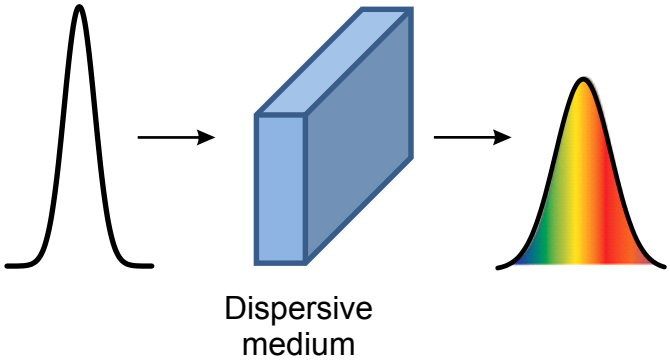

Figure 2.1: Optical pulse broadening after propagating through a dispersive medium (e.g. laser crystal, glass, air): long-wavelength components travel faster than the short-wavelengths ones.

process is sometimes referred to as chirping. In case of normal dispersion, when $\frac{\partial^2 k}{\partial \omega^2} > 0$, the long-wavelength components travel faster than the short-wavelength ones. The cubic term in equation 2.5, third order dispersion (TOD) per unit length, is responsible for an asymmetric pulse shape. The GVD can be used for calculating the duration of a spectral limited pulse with an initial pulse duration τ_0 propagating through a medium of length l:

$$\tau = \tau_0 \sqrt{1 + \left(\frac{4\ln(2) \times GVD \times l}{\tau_0^2} \right)^2} \tag{2.7}$$

Here, the GVD multiplied by the propagation length l in a medium yields the group delay dispersion (GDD):

$$\mathrm{GDD} = \frac{1}{2} \frac{\partial^2 k}{\partial \omega^2} \times l. \tag{2.8}$$

By adjusting the GDD to the specific requirements, it is possible to manipulate the phase response of pulses, which is vital for various laser applications.

2.2 Optical Kerr effect

In recent decades, the optical Kerr effect has played a considerable role in the evolution of ultrafast science. Let us consider the origin of this nonlinear phenomenon.

The electric polarization describes how a medium reacts to an incident light field, as follows from the Maxwell wave equation for an isotropic medium (equation 2.1). This induced medium polarization P[1], described by a Taylor expansion for high electromagnetic field strengths, can be divided into two parts: linear polarization P_{lin} and nonlinear polarization P_{nl}:

$$P = \epsilon_0(\chi^{(1)}E + \chi^{(2)}E^2 + \chi^{(3)}E^3 + \dots) = \underbrace{P^{(1)}}_{P_{lin}} + \underbrace{P^{(2)} + P^{(3)} + \dots}_{P_{nl}}, \tag{2.9}$$

assuming an instantaneous medium response. The coefficients $\chi^{(n)}$ are termed nth-order optical susceptibilities and depend on the medium properties. The nonlinear susceptibilities determine the nonlinear polarization of the medium in terms of the strength of the applied optical-frequency electric field [62]. Equation 2.9 implies that the nonlinear polarization of the medium gives rise to different nonlinear optical effects. Notice that the relative values of the terms increase with increasing field strength and, therefore, with increasing intensity denoted as:

$$I = 2n_0\epsilon_0 cE^2. \tag{2.10}$$

Generally, the second-order susceptibilities are on the order of 10^{-12} m/V, and third-order susceptibilities are on the order of 10^{-22} m^2/V^2 [62], therefore, nonlinear effects primarily manifest themselves only at high optical intensities. In isotropic nonlinear media, the third-order nonlinearity is usually the lowest non-zero nonlinearity as the second-order nonlinearity disappears in media possessing inversion symmetry (liquids, gases, amorphous solids). However, third-order nonlinear optical susceptibility $\chi^{(3)}$ can take place for both centrosymmetric and non-centrosymmetric media. In a dispersionless, isotropic medium, the total induced polarization is given by:

$$P = \epsilon_0\left(\chi^{(1)}E + \chi^{(3)}E^3\right) = \epsilon_0\underbrace{[\chi^{(1)} + 3\chi^{(3)}E^2]}_{\chi_{eff}}E\,, \tag{2.11}$$

[1]For the sake of simplicity, the fields are considered as scalar quantities henceforth.

A refractive index of the medium can be derived from the generally accurate relation:

$$n^2 = 1 + \chi_{eff}\,. \tag{2.12}$$

The term within the brackets in equation 2.11 may be viewed as the effective susceptibility χ_{eff} with the field-induced contribution causing a small, complex modification of the refractive index, the real ($\triangle n$) and imaginary ($\triangle\kappa/2k_0$) part of which can be inferred by introducing equation 2.11 into equation 2.12 [63]:

$$n^2 = (n_0+\triangle n+i\triangle\kappa/2k_0)^2 \approx n_0^2+2n_0\triangle n+in_0\triangle\kappa/k_0 = \underbrace{1+\chi^{(1)}}_{n_0^2}+3\chi^{(3)}E^2\,, \tag{2.13}$$

where n_0 specifies a linear (or low-intensity) refractive index determined by $\chi^{(1)}$. Recall that the third-order susceptibility is generally complex $\chi^{(3)} = Re(\chi^{(3)}) + Im(\chi^{(3)})$, and E^2 is connected to the field intensity I through equation 2.10. With that in mind, comparing the last two expressions in equation 2.13 yields for the real and imaginary corrections of the refractive index:

$$\triangle n = \frac{3}{4n_0^2\epsilon_0 c}\,Re\left(\chi^{(3)}\right) I = n_2 I\,, \tag{2.14}$$

$$\triangle\kappa = \frac{3\omega_0}{2n_0^2\epsilon_0 c^2}\,Im\left(\chi^{(3)}\right) I = \kappa_2 I\,. \tag{2.15}$$

Therefore the refractive index can be expressed as follows[2]:

$$n = n_0 + n_2 I \tag{2.16}$$

with

$$n_2 = \frac{3}{4n_0^2\epsilon_0 c}\,Re\left(\chi^{(3)}\right)\,. \tag{2.17}$$

Formula 2.16 indicates that the refractive index of a medium possessing third-order nonlinearities depends on the optical intensity, which in turn is time and space dependent in a general case. This phenomenon is the optical Kerr effect, a quasi instantaneously occurring nonlinear response of the material. More specifically, the intensity-dependent distortions of the electron clouds (electronic wave functions)

[2] Useful relations are $n_2\,[\frac{m^2}{W}] = \frac{283}{n_0^2}\chi^{(3)}\,[\frac{m^2}{V^2}]$ and $n_2\,[\frac{cm^2}{W}] = \frac{0.0395}{n_0^2}\chi^{(3)}\,[esu]$ (ref. [62], p. 210).

provoke nonresonant variations of nonlinear refractive index in the medium [62]. As it follows from the derivation of equation 2.16, the nonlinear polarization induced in the medium, influencing the properties of the light propagating in this medium, is responsible for the optical Kerr effect. The n_2 defined in equation 2.17 is the second-order nonlinear refractive index of the medium (often referred to as the Kerr coefficient). Typical values for the electronic polarization (for linearly polarized light) are: $n_2 \sim 10^{-16}$ cm^2/W, $\chi^{(3)} \sim 10^{-22}$ m^2/V^2 and a response time of 10^{-15} s (1 fs) (ref. [62], p. 211). Since the nonlinear effect accumulates in the medium during the propagation process, field intensities above 10^9 W/cm^2 may produce noticeable nonlinearities [61].

Two-photon absorption, for example, leads to an intensity-dependent contribution $\kappa_2 I$ to the linear absorption coefficient κ_0. Likewise, an intensity-dependent absorption coefficient is expressed as:

$$\kappa = \kappa_0 + \kappa_2 I \tag{2.18}$$

with:

$$\kappa_2 = \frac{3\omega_0}{2n_0^2\epsilon_0 c^2}\, Im\left(\chi^{(3)}\right). \tag{2.19}$$

Coming back to pulse propagation, the expression 2.5 for the propagation constant k can be modified as:

$$k(\omega) = k_0 + \triangle k + \frac{\partial k}{\partial \omega}\,|_{\omega_0}\,(\omega-\omega_0) + \frac{1}{2}\frac{\partial^2 k}{\partial \omega^2}\,|_{\omega_0}\,(\omega-\omega_0)^2 + \dots, \tag{2.20}$$

where $\triangle k = \frac{\triangle n \omega_0}{c}$ with $\triangle n$ expressed by equation 2.14. Furthermore, with the introduction of the retarded time $\tau = t - \frac{\partial k}{\partial \omega} z$, the pulse envelope function is redefined as $\tilde{E}_0(z,\tau) = \tilde{E}_0(z,t)$. Making use of equations 2.14 and 2.10, the nonlinear contribution to k is given by:

$$\triangle k = \frac{\triangle n \omega_0}{c} = n_2 \frac{\omega_0}{c} I = 2 n_0 \epsilon_0 n_2 \omega_0 |\tilde{E}_0|^2 \equiv \gamma |\tilde{E}_0|^2, \tag{2.21}$$

where the coefficient γ [rad / (W·m)] describes the self-phase modulation (SPM) effect, discussed below in section 2.3.

Finally, the equation describing optical pulse propagation through the dispersive nonlinear medium can be derived as:

$$\frac{\partial \tilde{E}_0}{\partial z} + i\frac{1}{2}\frac{\partial^2 k}{\partial \omega^2}\frac{\partial^2 \tilde{E}_0}{\partial \tau^2} = i\gamma |\tilde{E}_0|^2 \tilde{E}_0, \tag{2.22}$$

which is often referred to as the nonlinear Schrödinger equation. The full computation chain can be found elsewhere (ref. [62], p. 377). Observe, that it is possible for the GVD effects (the term including $\frac{\partial^2 k}{\partial \omega^2}$) to compensate for the SPM effects (the term including γ). The latter is feasible if $\frac{\partial^2 k}{\partial \omega^2}$ and γ have opposite signs. In this case, the shape of the optical pulses propagating through the dispersive nonlinear medium remains unchanged, leading to the formation of temporal solitons. In particular, such solitons are sought for KLM mode-locking [64]. At the same time, for soliton pulse propagation in a lossless dispersive medium, the pulse energy E_p and soliton pulse duration τ_p have to satisfy the following criterion [65]:

$$E_p = \frac{2\,|GDD|/l}{|\gamma|\,\tau_p}. \tag{2.23}$$

Hence, large constant negative values of GDD are essential for KLM. Possible ways of providing GDD control are discussed in section 4.1.

2.3 Processes arising due to the optical Kerr effect

According to formula 2.16, the intensity-induced alterations of the refractive index, influencing light propagation, bring up various self-action processes such as self-focusing [66], self-phase modulation [67], self-amplitude modulation (SAM) [68], self-diffraction, self-steepening etc. The two essential for KLM phenomena, self-focusing and self-phase modulation are discussed below.

Self-focusing

The spatial dependence of the intensity-dependent refractive index results in the self-focusing effect, and is illustrated in figure 2.2. For a Gaussian laser beam, the spatial intensity profile is translated into a spatial refractive index profile: As n_2 is positive in most materials, the refractive index at the central part of the beam is higher compared to the wings. This behavior can be considered as a positive lens, resulting in beam convergence and, eventually, in a catastrophic collapse in one point.

Despite the dependency of the refractive index on the laser intensity, the occurrence of self-focusing is governed by the peak power of the laser pulse [69]. An expression for the critical power P_{cr} for a Gaussian continuous wave (CW) laser beam with a central wavelength λ_0 is given by (ref. [62], p. 329):

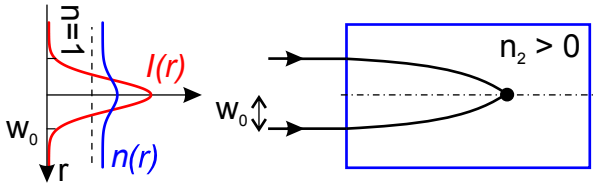

Figure 2.2: Schematics of the laser pulse intensity profile and the according refractive index profile (left): The refractive index at the central part of the beam is higher compared to the wings. Self-focusing effect of a laser beam in a nonlinear optical medium with $n_2 > 0$ (right): A positive lens results in beam convergence and a catastrophic collapse in one point.

$$P_{cr} = \frac{\pi(0.61)^2\lambda_0}{8n_0n_2}\,. \tag{2.24}$$

The characteristic self-focusing distance z_{sf} is estimated as follows (ref. [62], p. 332):

$$z_{sf} = \frac{2n_0w_0^2}{\lambda_0}\frac{1}{\sqrt{P/P_{cr}-1}}\,, \tag{2.25}$$

where w_0 is the Gaussian beam radius – the 1/e radius, at which 63.2% of the maximum intensity is contained.

Another self-action effect, the so called self-trapping of light, takes place when the power of the beam reaches the critical P_{cr} value. During self-trapping, the diffraction (defocusing) and self-focusing processes come to a counterbalance inside a medium, not allowing the laser beam to collapse and consequently preventing the damage of the material. In this situation, the laser beam propagates through the material with a confined diameter, in which case the beam can be viewed as its own waveguide.

Self-phase modulation

While the spatial dependence of the refractive index leads to self-focusing, the time dependence results in self-phase modulation. As a result of SPM, the phase of an optical pulse experiences a modification, specifically for high peak intensity pulses. Under the assumption of an instantaneous response of the nonlinear medium with the length l small enough, so that no reshaping of the optical pulse takes place, the acquired nonlinear phase shift $\triangle\phi(t)$ is given by (ref. [62], p. 375):

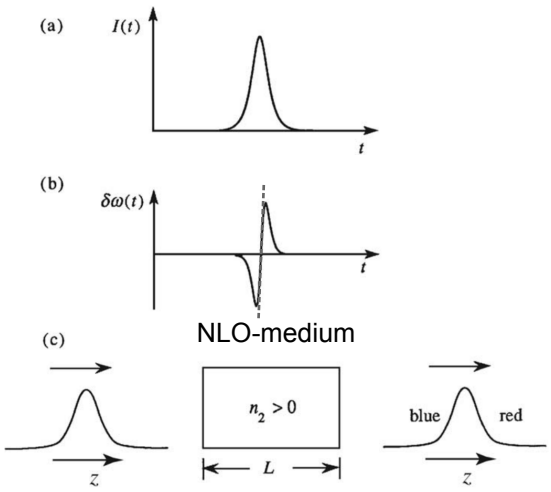

Figure 2.3: Self-phase modulation of an optical pulse: (a) The temporal intensity profile of a Gaussian pulse; (b) The variation in instantaneous frequency of the pulse for the case $n_2 > 0$; (c) SPM observation: The leading edge of the pulse undergoes a shift to lower frequencies (red-shift), whereas the the trailing edge is shifted to higher frequencies (blue-shift). Figure adapted from [62].

$$\triangle\phi(t) = -n_2 I(t)\omega_0 l/c\,. \tag{2.26}$$

An example of a Gaussian pulse shape is shown in figure 2.3(a). Passing through the nonlinear medium, the pulse modulates its own phase because of the time-dependent intensity slope. The instantaneous frequency concept, describing the spectral properties of the transmitted pulse, can be applied if the change of the optical pulse amplitude is slow compared to an optical period. The instantaneous frequency $\omega(t)$ of the pulse is expressed as:

$$\omega(t) = \omega_0 + \delta\omega(t)\,, \tag{2.27}$$

with the change of the instantaneous frequency $\delta\omega(t)$ defined as:

$$\delta\omega(t) = \frac{d}{dt}(\triangle\phi(t)) = -\frac{n_2\omega_0 l}{c}\frac{dI(t)}{dt}\,. \tag{2.28}$$

A depiction of the instantaneous frequency variation is presented in figure 2.3(b) for a medium with a positive nonlinear refractive index. Figure 2.3(c) shows that the leading edge of the pulse ($\frac{dI}{dt} > 0$) undergoes a red shift (to lower frequen-

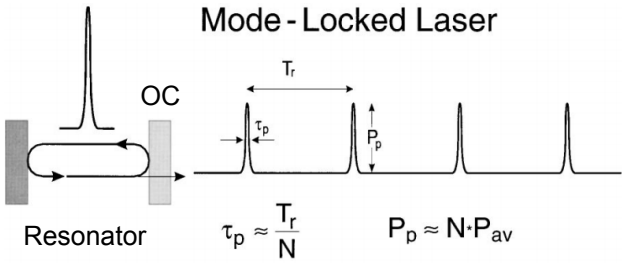

Figure 2.4: Schematic of a mode-locked laser. Resonator contains an output coupler (OC), through which a pulse train is emitted. Resonator round-trip time T_r, pulse duration τ_p, peak output power P_p, average output power P_{av}, number of locked modes N. Figure adapted from [19].

cies, longer wavelengths), whereas the trailing edge ($\frac{dI}{dt} < 0$) is blue-shifted (to higher frequencies, shorter wavelengths). Thus, the spectrum of the pulse normally becomes broader compared to that of the incident pulse. The instantaneous frequency change is called a chirp; an up-chirp for the above described fashion.

Note that for the central part of the pulse, the SPM-induced positive chirp is almost linear, which is widely made use of in pulse compression techniques.

2.4 Basics of mode-locking

In a general case, different longitudinal modes with random phase relations interfere inside an oscillator, and result in a randomly fluctuating output power. When the phases of the longitudinal modes are fixed, i.e. locked, a constructive interference of the oscillating modes takes place. As a consequence, the immense number of adjacent phase-locked longitudinal modes oscillate synchronously, leading to boosts of radiation energy concentrated within time periods of very short duration (figure 2.4). The radiation boosts occur periodically with a period determined by the resonator round-trip time T_r. Through a partially reflecting mirror (output coupler), a small fraction of the pulse energy is coupled out of the oscillator. Hereby, a mode-locked oscillator generates a train of ultrashort pulses [27, 64].

Solid-state (ruby, Nd:glass, Nd:YAG) lasers delivering sub-100-ps pulses formed the first generation of mode-locked lasers, mode-locking of which was achieved either actively or passively. The former technique was implemented through externally governed active loss or frequency modulation [70,71]. The latter technique, allowing more efficient pulse shaping and consequently shorter pulses, relied on a

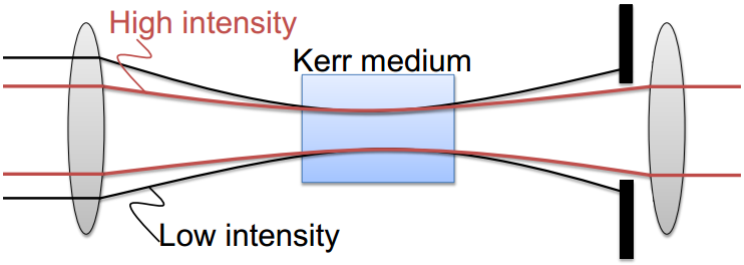

Figure 2.5: Fundamental principle of KLM: The lens influence becomes more severe for smaller beam radii and highly-nonlinear media. Self-focusing takes place for the beam of increased intensity, reducing losses in the cavity via an aperture of suitable size blocking of the low-intensity beam. This ultrafast SAM process triggers the mode-locking, and practically performs as an artificial saturable absorber. Figure adapted from [52].

fast saturable absorber [72,73] providing passive loss modulation [74,75]. Saturable absorbers are designated as fast or slow based on their recovery time compared to pulse duration.

Passive mode-locking methods use a nonlinear optical element with intensity-dependent losses, decreasing for increasing laser pulse intensity. Kerr-lens mode-locking is a technique of passive mode-locking, which utilizes an artificial saturable absorber based on Kerr lensing in the gain medium. Spence et al. [28] were the first to demonstrate this revolutionary technique in 1991, and later that year Piché [76] explained mode-locking operation through the self-focusing process. The optical Kerr effect (equation 2.16) translates the transverse laser beam intensity profile into a lens effect. The higher the light intensity, the stronger the lens effect. The lens influence becomes more severe for smaller beam radii. Self-focusing takes place for the beam of higher intensity, reducing losses in the cavity via an aperture of suitable size, blocking the low-intensity part of the (CW) beam. This ultrafast SAM process triggers the mode-locking, and practically performs as an artificial saturable absorber (figure 2.5).

Under particular conditions, the Haus master equation of mode-locking (ref. [64], p. 9) embraces the nonlinear Schroedinger equation (equation 2.22), leading to soliton solutions. These solutions occur when only the Kerr effect and GVD are considered (equation 2.6). As discussed in the preceding section 2.2, equation 2.22 states that solutions exist only when GDD and the coefficient γ have opposite signs. As the Kerr coefficient n_2, and correspondingly the SPM coefficient is usually positive, a high constant negative level of GDD is required for compensating the

SPM in order to obtain a mode-locked system.

Chapter 3

Multilayer coatings for ultrafast physics applications

Optical multilayer coatings have become an indispensable element of nearly all advanced ultrafast laser systems. Nowadays, multilayer dispersive coatings and high-damage-threshold broadband dielectric coatings are integrated in plenty ultrafast laser oscillators. This chapter is primarily concerned with a sequence of problems that needs to be solved in order to create a particular multilayer coating. First, the coating needs to be designed, the different theoretical approaches for which are discussed in section 3.1. The next step is a deposition of the designed coating, which can be realized by several means, as described in section 3.2. Additionally, section 3.2 considers available methods of thickness control, essential for the coating process, and explains the choice for both the deposition and thickness control techniques used in this work. Once fabricated, it is necessary to characterize the optical coating, inspecting its properties such as reflectance, transmittance, total optical losses and GDD. Section 3.3 lists characterization systems used in this work.

3.1 Design of the multilayer coatings: theoretical approach

Coating designs, as they exist today, first began development in 1958 when Baumeister introduced a merit function to estimate the proximity of designed spectral characteristics to a target, and formulated the design of optical coating problems as an optimization problem [77]. Prior to this, designs were either achieved through adapting microwave theory methods, an area that had already been well established for nearly two decades [78,79], or through the equivalent layers theory, which

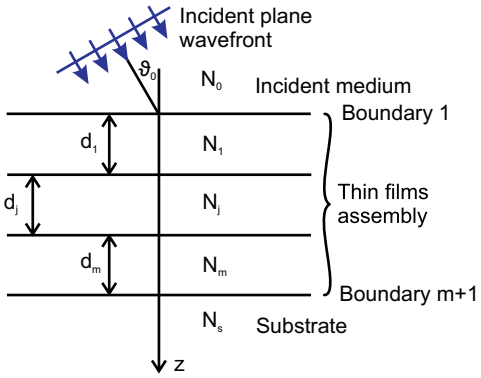

Figure 3.1: Schematic of a multilayer coating. A plane wavefront is incident on an assembly of thin films at an oblique angle of incidence ϑ_0. Z-axis is directed from the incident medium to the substrate. Symbols $N_1 \ldots N_m$ and $d_1 \ldots d_m$ denote the refractive indices and thicknesses of the individual layers, respectively. The refractive indices of the incident medium and of the substrate are designated as N_0 and N_s respectively. The interfaces between the thin films assembly and the incident medium and the substrate are denoted by the boundary 1 and boundary *m+1* respectively.

was summarized along with its cohesion with other design methods by Thelen [80]. In its early stages, Baumeister's merit function only allowed for the optimization of a given suitable starting design. However, at present, this procedure, generally known as refinement [81], is the most common out of modern multilayer optical coating design techniques. Typically the final design is obtained through the convergence of the refinement method to the local minimum of the merit function, which is close to the initial design. However, for the reason that there are no feasible starting designs for many important design problems, nonlocal design approaches were investigated. The Fourier transform technique [82–84], the needle optimization technique [85, 86] and the gradual evolution technique [87, 88] are all extremely effective and enable one to obtain theoretical designs with the required spectral characteristics while avoiding the problem of convergence at a local minimum. Note, however, that there is no universal recipe, and the most appropriate routine needs to be found empirically when solving a particular design problem.

In order to formulate the design problem, a multilayer coating consisting of m thin homogeneous and isotropic layers on a thick substrate is considered (figure 3.1). Normally, a film is considered to be thin in the case when full interference effects are observable in the reflected or transmitted light. Such a case is referred to as coherent. Whether the case is coherent or incoherent depends on whether the phase relationship between different beams is constant or not, which is dictated

by the nature of the light, by the light detector and the film quality. Here, the coherent case is discussed.

The optical admittance η (tilted implying oblique incidence) at a boundary between two media (e.g. boundary 1 in figure 3.1) is introduced as follows:

$$\begin{aligned} \eta_s &= \mathcal{Y} N \cos\vartheta \quad \text{for } s\text{-polarizatrion} \\ \eta_p &= \mathcal{Y} N / \cos\vartheta \quad \text{for } p\text{-polarizatrion,} \end{aligned} \tag{3.1}$$

with the optical admittance of free space $\mathcal{Y} = \sqrt{\frac{\epsilon_0}{\mu_0}} = 2.6544 \times 10^{-3}$ S. Here, the refractive index N (complex in a general case) and the angle ϑ stand for either N_0 and ϑ_0 of the incident medium or N_1 and ϑ_1 for the exit medium (e.g. the first layer) as appropriate.

For either direction of polarization, the amplitude reflection r and transmission t coefficients are:

$$r = \frac{\eta_0 - \eta_1}{\eta_0 + \eta_1} \tag{3.2}$$

and

$$t = \frac{2\eta_0}{\eta_0 + \eta_1}\,. \tag{3.3}$$

In order to avoid fundamental difficulties [89], the incident medium is considered to be absorption-free, which means η_0 is real, then the intensity transmission and reflection coefficients (transmittance T and reflectance R) are given by:

$$R = \left(\frac{\eta_0 - \eta_1}{\eta_0 + \eta_1}\right)\left(\frac{\eta_0 - \eta_1}{\eta_0 + \eta_1}\right)^* \tag{3.4}$$

$$T = \frac{4\eta_0 \mathrm{Re}(\eta_1)}{(\eta_0 + \eta_1)(\eta_0 + \eta_1)^*}\,, \tag{3.5}$$

where * denotes a complex conjugation procedure.

The reflectance of a multilayer is obtained through the optical admittance concept. The arrangement is displayed in figure 3.1, where a plane wavefront is incident on an assembly of thin films at oblique angle of incidence (AOI) ϑ_0. The physical thicknesses of the layers are denoted by d_1 through d_m and their refractive indices by N_1 through N_m. The refractive indices of the incident medium and of the substrate are designated as N_0 and N_s respectively. Now, the thin film assembly (between boundaries 1 and *m+1* in figure 3.1) is substituted with a single surface, possessing an optical admittance Υ, given by the ratio of the normalized

tangential magnetic field C and electric field B amplitudes:

$$\Upsilon = C/B\,. \tag{3.6}$$

The general characteristic matrix of an assembly of m layers according to the Abeles matrix method is [89, 90]:

$$\begin{bmatrix} B \\ C \end{bmatrix} = \left\{ \prod_{j=1}^{m} \begin{pmatrix} \cos\delta_j & (i/\eta_j)\sin\delta_j \\ i\eta_j \sin\delta_j & \cos\delta_j \end{pmatrix} \right\} \begin{bmatrix} 1 \\ \eta_s \end{bmatrix}, \tag{3.7}$$

where $\delta_j = \frac{2\pi}{\lambda} N_j d_j \cos\vartheta_j$ is the j-th layer phase thickness with angle of refraction ϑ_j and the wavelength of the incident light in vacuum λ; η_s is the substrate admittance. It should be noted, that the correct order of the product of individual characteristic matrices, in the case where m is the layer closest to the substrate, is:

$$\begin{bmatrix} B \\ C \end{bmatrix} = [M_1]\,[M_2]\ldots[M_m] \begin{bmatrix} 1 \\ \eta_s \end{bmatrix}, \tag{3.8}$$

where M_1 is the matrix for layer 1, M_2 is the matrix for layer 2 etc. The general characteristic matrix of an assembly of m thin layers, saliently important in optical thin-film engineering, establishes the basis of the majority of the calculations. Then the basic formulas for calculating spectral characteristics of a multilayer coating are given as follows:

$$R = \left(\frac{\eta_0 B - C}{\eta_0 B + C}\right)\left(\frac{\eta_0 B - C}{\eta_0 B + C}\right)^* \tag{3.9}$$

$$T = \frac{4\eta_0 \mathrm{Re}(\eta_s)}{(\eta_0 B + C)(\eta_0 B + C)^*}\,. \tag{3.10}$$

The phase shift on reflection, defined for the front surface of the assembly, is expressed by:

$$\varphi_r = \arctan\left(\frac{\mathrm{Im}\left[\eta_s(BC^* - CB^*)\right]}{\eta_s^2 BB^* - CC^*}\right) \tag{3.11}$$

and the phase shift on transmission, detected between the emergent wave at its exit from the assembly and the incident wave at its entry, by:

$$\varphi_t = \arctan\left(\frac{\text{-Im}\left[\eta_0 B + C\right]}{\text{Re}\left[\eta_0 B + C\right]}\right). \tag{3.12}$$

In order to solve an inverse[1] design problem one needs to determine the number of layers of a multilayer coating, and refractive indices and thicknesses of each layer, which provide the required target spectral properties. The parameters m, n_j and d_j for $j = 1, \ldots, m$ are hence referred to as the design parameters.

A multilayer coating with reflectance and phase shift characteristics close in some respect to the target spectral characteristics, denoted $\tilde{R}(\lambda)$ and $\tilde{\varphi}(\lambda_j)$ respectively, are often as good as can be achieved, as typically there is no exact solution to meet the target [91]. The set of physical layer thicknesses can be described through a vector X where:

$$X = \{d_1, d_2, \ldots, d_m\}. \tag{3.13}$$

Now, the reflectance shall be denoted by $R(X, \lambda)$ and the phase shift by $\varphi(X, \lambda_j)$ under the assumption that the other design parameters (m and n_j) are fixed. Treating the wavelength as a discrete set of L points $\lambda_1, \lambda_2, \ldots, \lambda_L$ is necessary since it is not possible to compute $R(X, \lambda)$ or $\varphi(X, \lambda_j)$ using a continuous function over the considered spectral region. The most common way to estimate the deviation between the resultant and the target characteristics is by using a weighted mean square deviation on the introduced wavelength mesh [92]:

$$F(X) = \frac{1}{L}\sum_{j=1}^{L}\left\{\left[\frac{R(X, \lambda_j) - \tilde{R}(\lambda_j)}{\triangle R_j}\right]^2 + \left[\frac{\varphi(X, \lambda_j) - \tilde{\varphi}(\lambda_j)}{\triangle \varphi_j}\right]^2\right\}, \tag{3.14}$$

where $\triangle R_j$ and $\triangle \varphi_j$ are design tolerances. The merit function *F(X)* is governed by the vector X. As already mentioned, introducing *F(X)* enables the design problem to be defined as an optimization problem, which is currently the most popular general approach for designing multilayer optical coatings. It is also worthwhile to point out that the total design thickness is of significant importance for successful approximation of the target spectral characteristics, particularly when dealing with abrupt features (such as edge filters, bandpass filters, etc.).

All the designs presented in this thesis were obtained using a commercial OptiLayer software package [93]. The software utilizes the aforementioned powerful

[1] A direct design problem defines the spectral properties of the multilayer structure based on the known number of layers, refractive indices and thicknesses of each layer.

approaches such as needle optimization and gradual evolution algorithms [86–88].

3.2 Coating techniques and layer thickness control

There is a considerable amount of processes used for the deposition of optical coatings. The most common ones take place in vacuum and are classified as physical vapor deposition[2] (PVD). In this class of processes, the thin film is formed in the solid phase as a result of direct condensation from vapor. PVD processes are classified based on the methods used for producing the vapor and on the energy involved in the thin films deposition and growth.

Due to its simplicity, flexibility and relatively low cost, as well as to a vast amount of existing deposition systems, thermal (or vacuum) evaporation has been the widely-used PVD method for a long time [56]. In thermal evaporation, the vapor is produced by simply heating the evaporant (material to be deposited). The vapor then condenses as a solid film on a substrate, kept at a temperature below the melting point of the evaporant. The position of the spot can be varied by supplementary magnetic fields derived from coils in order to be placed in the center of the crucible. However, thermal evaporation possesses major disadvantages, especially in regard to the microstructure of the films. Layer microstructure defines the properties of optical thin films and the manner they diverse from those of the same bulk material. Typically, thermally evaporated thin films have columnar structure, with the columns following the direction of growth, normal to the substrate surface. The columns, the shape of which is more or less cylindrical with a bottom diameter of several tens of nanometers, are packed in a nearly hexagonal way with gaps in between, which are basically pores running across the entire film. The large areas of column surface forming the pores are exposed to the surrounding air. The porous layers with lower refractive indices are likely to show a so-called vacuum shift: Pores exposed to ambience are filled with water, the refractive index of the thin film increases and the spectral curves shift to the longer wavelengths [79, 94, 95]. Packing density, defined as a ratio volume of solid part of the film (i.e. columns) to the total volume of the film (i.e. pores and columns), is a parameter of a great importance. For thermally evaporated thin films it commonly

[2]The term chemical vapor deposition (CVD) is reserved for a group of techniques where the composition and properties of the film being grown differ substantially from the components of the vapor phase.

ranges from 0.8 to 0.95. Packing density lower than 1 indicates a reduction of the refractive index compared to that of the bulk material, the columns are formed of.

Therefore, for high-performance specialized coatings other processes, such as sputtering, have been developed. In sputtering, the vapor is produced by bombarding a target with energetic particles (most commonly ions) in order to cause the ejection of the atoms and molecules from the target. The energy of such vapor particles is considerably higher than that of the products of thermal evaporation and has a significant impact on the condensation and film-growth processes. In particular, the films produced by sputtering are usually much more dense and solid. In other kinds of PVD, additional energy derived from direct bombardment by energetic particles supplies the condensation of thermally evaporated material. Such processes, along with sputtering, are generally referred to as energetic ones. A metallic target is used in the conventional form of sputtering, so that it conducts and the bombarding ions are derived from a direct current discharge near the target. In the magnetron sputtering process, this discharge may be confined by crossed electric and magnetic fields. The magnetron sputtering technique is the most common process applied in optical coatings. One of the main advantages of magnetron sputtering is the much longer path length of the electrons. This means that the discharge can be sustained at a relatively low pressure (0.3 Pa or 0.3×10^{-2} mbar for example) compared to that required for conventional sputtering in the absence of the magnetic field. Twin magnetron targets connected to opposite poles of a mid-frequency power supply (known as mid-frequency sputtering, or twin/dual magnetron sputtering) avoid both "target poisoning" and "disappearing anode" – two issues common for normal single-target sputtering. In brief, target poisoning arises due to molten droplets in the target material caused by stored charge in insulating film patches of a high capacitance, which are formed by oxidation or nitriding. An insulating film gradually covering an anode from one coating run to another is essentially the reason for the disappearing anode phenomenon. The arrangement of alternating anode and cathode solves both of these problems.

Despite the fact that PVD methods are prevalent among the variety of deposition processes used for optical coatings, the utilization of CVD has been gradually rising. Electrically induced plasma in the active vapour is probably the most common way to trigger the chemical reactions between the precursors (starting materials) forming the material of the coating. These processes are classified as plasma enhanced ones [56]. The most advanced form of sputtering techniques, known as ion-beam sputtering (IBS) [96], utilizes a separate chamber to generate the ions that afterwards are extracted and directed towards the target. This

method provides a very high degree of film purity. The optical coatings with the lowest published losses (1 ppm or less) have been obtained via this process [97,98]. Ion-beam sputtering is slow compared to most other processes and is mainly used for coatings where low loss is the critical criterion.

There are many issues in the preparation of and during the coating process that need to be taken care of: choosing suitable materials, cleaning substrates, designing a proper substrate–holder geometry to provide the required distribution accuracy, and more. However, layer thickness monitoring and control is the main remaining problem as the other issues have been reasonably resolved. Refractive index and optical thickness are the most important parameters.

Presently, there is no method of measuring the refractive index of exactly that portion of a film which is being deposited. Such measurements can be made later, but for closed loop control, dynamic measurements are essential. Therefore, normally, deposition parameters affecting refractive index are controlled in a way that the refractive index produced for any given material, or mixture of materials, is as consistent as possible. The value of the refractive index obtained a posteriori is used in the coating design. The results of this procedure are usually satisfactory results, albeit far from ideal. Nowadays, no better method has been developed.

The physical thickness of a layer can easily be measured and controlled. Among a variety of methods, the most frequently used are based on either optical measurements of reflectance or transmittance, measurement of the total deposited mass by the quartz-crystal microbalance, or on time deposition control. Optical monitoring systems include a light source illuminating a test substrate and a detector analyzing the reflected or transmitted light. The deposition of the layer proceeds according to the results of this analysis. A shutter inserted in front of the evaporation sources is a common way to stop the layer deposition as sharply as possible. There is an assortment of various optical monitoring techniques, both operator controlled and automatic, capable of different levels of errors (which scale from being just sufficient for the simplest designs to 0.2–0.3 nm) described by Macleod (see ref. [99] and references therein).

The principle of monitoring by the quartz-crystal microbalance is to expose the crystal to the evaporant stream and to measure the change in its resonant frequency as the film deposits on its surface and changes the total mass [100]. The frequency change is then converted internally into a measure of film thickness using known film constants. It is possible to conduct the measurement of mass thickness with an accuracy of around 2% for a typical layout [99]. The sensitivity of the crystal decreases with increasing mass, and the total amount of material which can be

Figure 3.2: The Helios magnetron sputtering system of LEYBOLD OPTICS (BÜHLER AG) integrates the intermittent deposition technique in a chamber that is never opened to atmosphere except when servicing is necessary. Figure adapted from [56].

deposited before the crystal must be replaced is limited. Implementing a multiple crystal head solves this problem. Alignment is much easier than that for optical monitors, however the dimensional stability requirements are as strict.

The stability of the the energetic processes, especially sputtering, in terms of refractive index and other properties allows for control of layer thicknesses by time, or, alternatively, by the number of substrate turn-table rotations. For example, Gibson et al. [101] have reported run-to-run reproducibility of ± 0.3 % in the TiO_2/SiO_2 edge filter characteristics for the visible region, manufactured by the close-field magnetron sputtering technique.

As already mentioned, the very stable sputtering technique renders very consistent thicknesses and therefore, makes precise time-controlled monitoring of layer thicknesses possible [59]. Magnetron sputtered thin films demonstrate packing density of almost unity, which means that the thin film properties are nearly the same as those of bulk material. For these reasons, the method for multilayer structures production used in this work was the magnetron sputtering technique (figure 3.2) equipped with broadband in-situ monitoring (BBM) [102], providing additional control. The plant is equipped with two TwinMags magnetron targets and a plasma source for plasma/ion-assisted reactive middle-frequency dual-magnetron

sputtering. Layers at deposition rates of 0.4 nm/s allow for rapid manufacturing as well as the production of extremely dense (near intrinsic solid density), smooth and amorphous layers with high reproducibility. Helios plant covers the spectral range from 250 to 3000 nm; substrate diameters up to 100 mm are suitable for coating. A fused silica (FS) or a B270 glass substrate is typically used as a test witness sample during the process.

3.3 Characterization of the multilayer coatings

In order to improve performance of DMs one needs to precisely characterize manufactured samples. The main parameters such as reflectance, transmittance, total optical losses and GDD need to be quantified. Losses in thin films are of particular importance in the laser field where they determine the limiting performance of multilayers.

The first indicators of a successful deposition process is a good correspondence of the measured reflectance and transmittance of the coating to the designed ones. An industrial spectrophotometer Perkin Elmer Lambda 950 is capable of measuring both transmittance and reflectance (via an integrating sphere) at different AOIs in the wavelength range from 175 nm to 3300 nm. According to the specifications supplied by the company, the device provides a wavelength accuracy of ± 0.08 nm for ultraviolet/visible (UV/vis) range and (± 0.3 nm for near-infrared spectral region, NIR), and a UV/vis resolution of ≤ 0.05 nm (≤ 0.2 nm for NIR). Spectrophotometric measurements yield a good general representation of the spectral performance of a fabricated multilayer structure. However, the accuracy of the reflectance obtained by this method is often limited to fraction of a percent (~ 0.1 %). Higher precision is ensured by an industrial lossmeter based on the cavity ring-down technique (NovaWave Technologies LossPro) measuring total optical loss at available AOIs of either 7.5° or 45°. The measurements can be performed at 808 nm, 1030 nm and 1550 nm. Total optical loss on the scale of a few parts per million (ppm) can be accurately measured via this method [103]. Minimum instrument precision is typically less than 1 % of the total measured loss (data from the manual). Although, it is reliable in the low-loss approximation only ($L < 1000\,\text{ppm}$) and is limited by the speed of the electronics, which makes cavities with total optical losses larger than 0.1 % difficult to measure. If the measured optical characteristics drastically differ from the designed ones, another batch needs to be coated with the corrections obtained from the mismatch analysis. Otherwise, if the measured and designed spectra of an optical coating are within acceptable

tolerance, the next step is to conduct GD and GDD measurements.

A good match between theoretical and experimentally acquired data for GD and GDD, characteristics of great importance, validates a proper performance of the produced DMs. Nowadays, a white light interferometer (WLI) technique [104–107], usually based on the two-armed Michelson interferometer, is widely used for measuring dispersion characteristics of DMs. The sample under investigation is placed in one of the interferometer arms. The reference mirror, placed in the other arm, is moved and a resulting interferogram (interference pattern) is recorded for each position. Obtained data is subsequently processed and provides GD and GDD curves of the sample. In this work, a home-built WLI, allowing measurements of the GDD over a large bandwidth from 320 nm to 2150 nm and providing a spectral resolution of 2.2 nm, was used [108, 109].

Another important parameter is the surface quality of the substrates. Low surface quality of the substrates leads to high scattering losses, which in turn means bad performance of the optical coating deposited on such low quality substrates. In order to examine the surface roughness of both uncoated and coated substrates, an industrial atomic force microscope (AFM) from Fries Research and Technology (FRT) providing an accuracy of 0.1 nm was used.

In case this comprehensive characterization of an optical coating, DMs as well as other specially tailored coatings, yields adequate results, the coating is considered successful and ready to be utilized.

Chapter 4

Highly dispersive optics for ultrafast oscillators

Highly-dispersive mirrors (HDMs) have become a key tool in the field of ultrafast physics over the last two decades [30, 110–112]. Presently, the majority of femtosecond lasers include dispersive mirror optics which allow precise control of GDD characteristics.

Diode-pumped solid-state TD laser technology has the potential of achieving the highest peak powers directly from laser oscillators [51]. Due to its power scalability, TD technology may constitute the basis for next-generation femtosecond laser oscillators [47], as they have already permitted the generation of sub-picosecond pulses at unprecedented power levels in the multi-100-W average power and near-100-MW peak power range [54, 113–116]. The first high-power KLM TD oscillator providing values such as an average power of 45 W and a pulse duration of 250 fs directly available from the oscillator at a repetition rate of 40 MHz (corresponding to a pulse energy of 1.1 μJ and peak power of 4.5 MW) was demonstrated in 2011 [117]. Recently, such a system has been scaled up to an average output power of 270 W and a pulse duration of 210–330 fs at 18.8 MHz repetition rate (corresponding to a pulse energy of 14.4 μJ and peak power of 38 MW) in the mode-locked regime, operating in ambient air [54]. Mode-locked operation in the regime of anomalous dispersion was realized by 8 bounces each on two HD folding mirrors with a GDD of $-3000\,\mathrm{fs}^2$ each [112], introducing a total roundtrip GDD of $-48\ 000\,\mathrm{fs}^2$. Furthermore, a compact KLM Yb:YAG TD oscillator (footprint 70 cm by 40 cm without a laser diode) delivering 215-fs pulses with 75-W average power and 1.4-MW peak power at a high repetition rate of 260 MHz has been reported [118]. Successful operation and the advancement of such systems heavily relies on the ability of HDMs to provide high dispersion levels.

For high-power intra- and extra-cavity applications, a combination of several

parameters is important. These include a high constant GDD level for SPM compensation, a large bandwidth, low scattering losses, low thermal effects to avoid mirror radius curvature distortions, as well as a high damage threshold. Local changing of the radius of curvature leads to a change in the focal lengths in the resonator, which might cause a reduction of the DT and a malfunction of the oscillator.

This chapter focuses on the basic principles (section 4.1), design, fabrication, characterization and implementation of optics considering different substrate materials (section 4.2), and reaching new levels of dispersion in HDMs (section 4.3) towards finding the best possible solution to the aforementioned issues.

4.1 Dispersive mirrors: operational principles

As already emphasized in chapter 2, the ability to control the dispersion is of great importance. To this end, methods based on different concepts are commonly applied: Diffraction gratings [119], prism pairs [120], dispersive mirrors [30,121–123], or a combination thereof [124,125]. A pair of diffraction gratings has allowed successful pulse compression [119], however these gratings possess rather high losses. Widely used since their discovery, prism pairs were the first to provide negative GDD with low losses, albeit the prisms possess unwanted nonlinearities. On the contrary, dispersive mirrors (DMs) with high reflectance and approximately constant GDD over unprecedented broad bandwidths have been enabled by progress in the design and fabrication of dispersive coatings at that time [126,127]. Two operational principles of DMs, resonance effect and penetration effect, are discussed below.

Resonance effect

Dielectric multilayer mirrors, designed as Gires-Tournois interferometers (GTI), were used to manipulate the net cavity dispersion for the first time [121]. The main property of these GTIs is a frequency-dependent optical phase shift, due to which a GD between resonant and non-resonant frequencies is introduced (figure 4.1(a)). This effect is often referred to as resonant storage. Large amounts of GDD can be introduced through this resonant storage. However, the operational spectral bandwidth of the GTI mirrors is relatively narrow, owing to their nature.

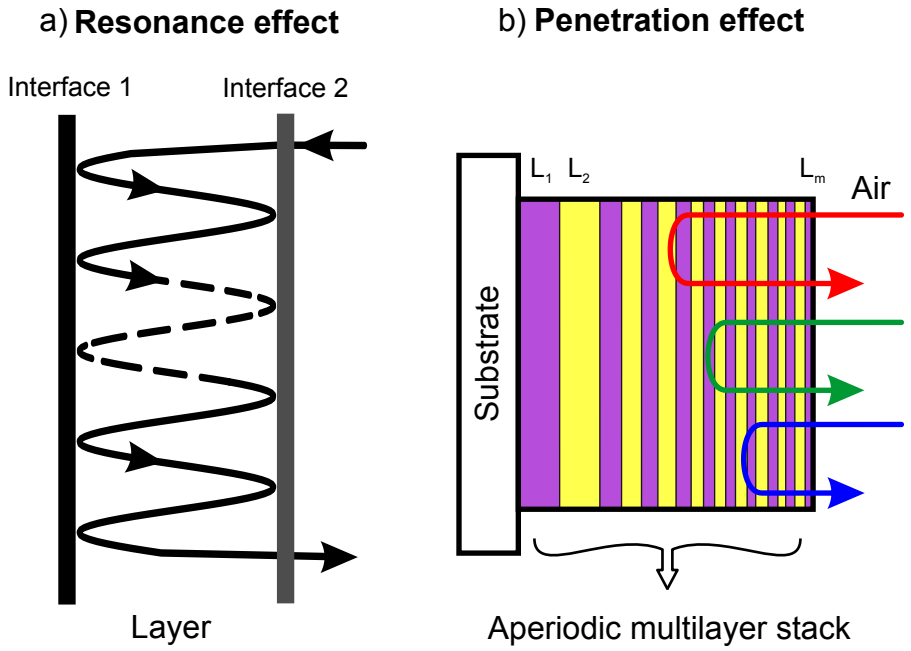

Figure 4.1: Basic principles of multilayer dispersive mirrors: (a) **Resonance effect**. Two layer interfaces separated by a half-optical thickness distance resonantly enclose the incident resonant wave. These nanoscale GTIs built into the multilayer structure can introduce large amounts of GD and GDD between resonant and non-resonant frequencies due to the frequency-dependent optical phase shift [128]. (b) **Penetration effect.** Optical layer thicknesses of a multilayer stack are gradually decreasing with increasing layer number (L_1, L_2... L_m), which results in different penetration depths for different wavelengths before being reflected. This "penetration effect" is caused by the constructive interference of the coherent beams partly reflected from each interface between low- (e.g. yellow bars) and high- (e.g. violet bars) index materials of the aperiodically arranged multilayer stack. Shorter wavelengths (indicated by a blue arrow) are reflected in the upper layers of the structure. Whereas, longer wavelengths (indicated by a red arrow) penetrate deeper and are reflected deeper in the structure. Since the longer wavelengths leave the mirror structure later compared to the shorter ones, an increasing with increasing wavelength (decreasing frequency) GD emerges, resulting in negative GDD.

Penetration effect

DMs, initially introduced as chirped mirrors (CMs) by Szipöcs et al. in 1994 [30], have become more and more prominent in dispersion compensation techniques due to their ability to control second- as well as higher orders of dispersion with unprecedented precision [58, 129]. If the dispersion needs to be controlled over a narrow spectral range only, it is possible to produce DMs with reflectance exceeding 99.9% [110, 112]. As a further advantage, DMs are easier to build into an optical setup compared to prisms and gratings [110].

The basic operational principle of a DM [30] is depicted in figure 4.1(b) and can be described as follows. As a consequence of the gradual modulation of optical layer thicknesses of a conventional mirror, for example in quarter wave stack (QWS), with respect to the layer number, different wavelengths penetrate to different depths before experiencing the reflection. This "penetration effect" is caused by the constructive interference of the coherent beams partly reflected from each interface between low- and high-index materials of the aperiodically arranged multilayer stack. In particular, shorter wavelengths are reflected in the upper layers of the structure, whereas longer wavelengths penetrate deeper before reflection. Since the longer wavelengths leave the mirror structure later compared to the shorter ones, an increasing GD with increasing wavelength (decreasing frequency) emerges, resulting in a negative (anomalous) GDD (see equation 2.6).

A set of DMs (compressor) allows for the compression of amplified pulses, broadened in a dispersive medium (stretcher) prior to amplification. Ideally, the dispersion introduced by the DMs should be equal to the dispersion of all the components inside the particular laser system, but with an opposite sign. The described technique, enabling amplification of ultrashort laser pulses up to the peak powers of 10^{15} W, is termed chirped pulse amplification (CPA) [130]. Both the resonance and penetration effects were simultaneously utilized in broadband HDMs for all-dispersive CPA, which resulted in nearly ideal Gaussian beam profiles of 19.1-fs-pulses [128].

Multilayer coatings discussed in this work are based on a combination of resonance and penetration effects.

4.2 Substrates for highly-dispersive mirrors

Surface defects are merely a divergence from the smooth flat surfaces of the ideal film which lead to scattering losses. Surface defects can be due to roughness of the

substrate surface which tends to be reproduced at each interface in a multilayer. Superior surface quality of substrates (flatness and parallelism) is required for use with ultrafast lasers. Furthermore, when operating at high average powers, distortions may arise at mirror surfaces. For example, the change of a mode profile and beam-pointing drifts, indicating a slow and time-dependent misalignment of the cavity, has been observed in a CW cavity comprising HDMs deposited onto fused silica substrates (GDD values of -1000 fs^2 and -3000 fs^2 [112]) at intracavity power levels above 1 kW [52]. Although, a solely thermal origin of these power-dependent effects could not be identified, the reported temperature rise was 10–20°C. In order to minimize the thermal effects appearing intracavity, one needs to consider different substrate materials which might aid transferring the heat away from the coated surface.

The performance of such materials as FS, copper, silicon, sapphire and nickel plated copper was investigated in this section to find the ideal characteristics for substrates. The properties of these materials are summarized in table 4.1. FS is a widely used substrate material, even though its thermal conductivity coefficient is rather small. Sapphire substrates demonstrating high surface quality are common as well. The thermal conductivity of this material is significantly higher than that of FS. Metal substrates can transfer heat better than FS substrates, although the roughness of metals is somewhat high (usually 10–50 nm [131]). Nickel plating supposedly prevents the copper from oxidizing and allows the surface to be better polished. It should be mentioned, that some undesirable effects can appear seeing that the thermal expansion of metals is relatively high. In spite of the low coefficients of thermal expansion of ultra low expansion glass ULE ($0\pm30\times10^{-9}/K$) and extremely low expansion glass ceramic Zerodur ($0.05\pm0.1\times10^{-6}/K$), the thermal conductivity coefficients of these materials are comparable to that of FS (1.31 W/(m·K) for ULE; 1.46 W/(m·K) for Zerodur) [132, 133]. Thus, ULE and Zerodur remain outside the present discussion.

HDMs with a designed GDD value of -3000 fs^{2}and a designed reflectance of 100% for a wavelength range of 1025–1035 nm (entitled HD1302 in house, HDM2 in ref. [112]) were deposited onto the aforementioned substrates with the help of the magnetron sputtering technique described in section 3.2. These mirrors were already successfully implemented in several Yb:YAG TD oscillators [52,54,112]. As an example, the designed and measured data for the HDM coated on a FS substrate obtained with the WLI and the lossmeter described in section 3.3 is presented in figure 4.2. The comparison of the theoretical and experimental evidence reveals a good agreement.

Substrate material	Thermal conductivity coefficient, W/ (m·K)	Thermal expansion linear coefficient, 10^{-6} /K	σ_{rms}, nm
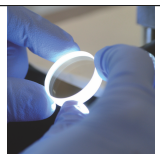 Fused Silica (FS), SiO_2	1.4 [134], 1.46 [135]–3 [136]	0.54 [135]	0.7±0.1
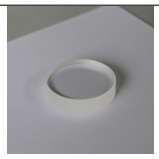 Sapphire, Al_2O_3	35.1, 33 [137], 35–40 [135]	5.6, 5 [137], 5.8 [135]	0.4±0.1
 Silicon, Si	80–150 [135], 149 [138]	2.56 [139], 4.7-7.6 [135]	0.6±0.1
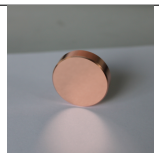 Copper, Cu	401 [138]	16.5 [138]	1.7±0.1
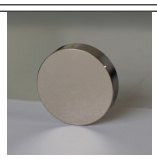 Nickel-plated copper, Ni-plated Cu	~400*	~17*	1.5±0.1

*No data was found for nickel-plated copper in the available sources and was therefore assumed to be close to that of pure copper.

Table 4.1: Thermal properties and surface roughness of the substrates under consideration; the listed data is for room temperature (25°C). The values of surface roughness σ_{rms} for a randomly chosen area of 7×7 μm were obtained experimentally with AFM described in section 3.3. The diameter of the substrates is 25.4 mm. Thickness of the substrates is 6.35 mm, except for Si substrate with a thickness of 3 mm.

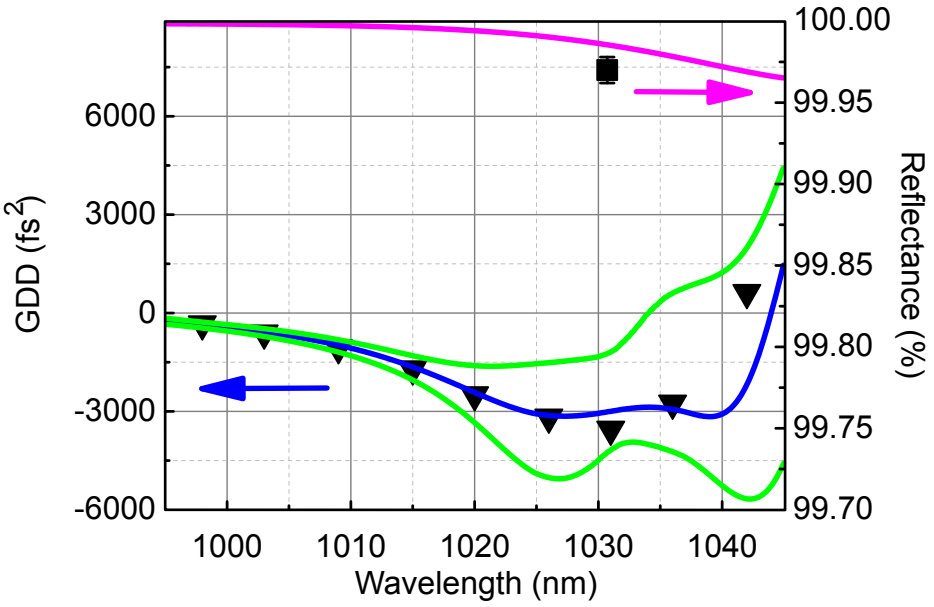

Figure 4.2: Comparison of the designed and measured data for the HDM with –3000 fs^2 [112] coated on a FS substrate: The designed GDD for 3° angle of incidence (blue curve), error bars ± 0.5 nm (green curves); the measurement performed with a WLI at 3° angle of incidence (black triangles). The designed reflectance for 7.5° angle of incidence (magenta curve), the square at 1030 nm represents the measurement performed with a lossmeter at 7.5° angle of incidence.

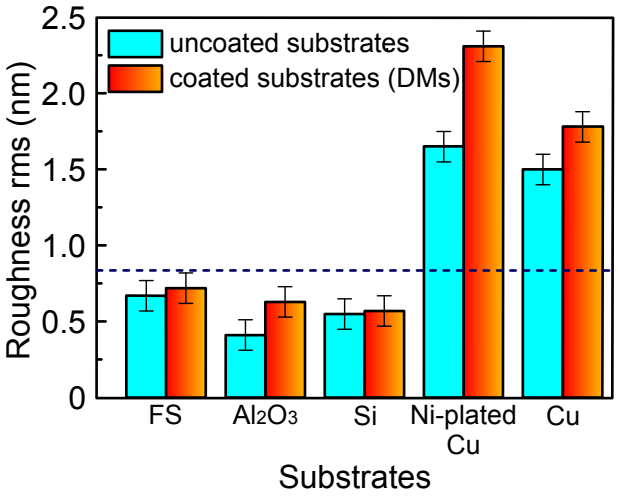

Figure 4.3: Comparison of surface roughness σ_{rms} for a randomly chosen area of 7×7 μm of uncoated (light blue bars) and coated substrates (red-orange bars). The measured area is not the same for uncoated and coated substrates. The dark blue dashed line is set at 0.84 nm.

Next, all the samples were characterized with the AFM and the lossmeter reported in section 3.3. The rms (root mean square) surface roughness σ_{rms} defined as the rms deviation of the surface from the mean surface level for a randomly chosen area of 7×7 μm of both the uncoated and coated substrates (listed in table 4.1) is displayed in figure 4.3. The measured area was not the same for uncoated and coated substrates. One can see that FS, sapphire and silicon substrates possess quite similar roughness (σ_{rms} below 0.84 nm) which is barely affected by the coating process. At the same time, the initially relatively high (σ_{rms} above 1.5 nm) roughness of uncoated copper and nickel-plated copper substrates increases after the deposition of the multi-thin films onto the surfaces. The polishing process consists partly of a smoothing out of irregularities in the surface by moving the substrate. If the grinding (which always precedes the polishing) has been too coarse, then the deeper pits during the polishing are filled in with material which is only loosely bonded to the surface. During the heating and then coating of the surface, this poorly bonded material breaks away, leaving a patch of surface that is etched in appearance and often possesses well-defined boundaries. This might be the case here. Nevertheless, the examined metal surfaces show rather high quality (usually σ_{rms} of metals is 10–50 nm).

The reflectance R, transmittance T, absorbance A and scattered losses S in a

multilayer structure are connected by the relationship:

$$R + T + A + S = 100\%, \tag{4.1}$$

where $T + A + S$ is the total optical loss TOL measured by the lossmeter. For the DMs under consideration, A is assumed to be insignificantly small during the design process, therefore the total optical loss may be expressed as following in this particular case:

$$TOL = T + S. \tag{4.2}$$

The optical scattering is mainly determined by the surface roughness. The functional relationship between total integrated scatter (TIS, the total amount of light scattered by a surface) and surface roughness is given by [140, 141]:

$$TIS = R_0 \left[1 - \exp \left\{ - \left(\frac{4\pi\sigma_{\text{rms}} \cos\vartheta_i}{\lambda} \right)^2 \right\} \right], \tag{4.3}$$

where R_0 is the theoretical reflectance of the surface, ϑ_i is the AOI on the surface and λ is the wavelength of the incident light. Taking into account equation 4.3, the final theoretical estimation of TOL depending on the surface roughness σ_{rms} is brought to the following expression:

$$TOL = T_0 + R_0 \left[1 - \exp \left\{ - \left(\frac{4\pi\sigma_{\text{rms}} \cos\vartheta}{\lambda} \right)^2 \right\} \right], \tag{4.4}$$

where T_0 is the theoretical transmittance of the surface. Figure 4.4 shows the dependence of TOL for the multilayer structures (figure 4.2) coated onto different samples on the surface roughness σ_{rms}. The values are averaged over a number of substrates and measurements. As expected, the coating on the copper and Ni-plated copper substrates have quite significant losses of about 7000 ppm ($R = 99.3\,\%$, measured via the spectrophotometer described in section 3.3), which despite their excellent conductivity, unfortunately makes them inappropriate for application in Yb:YAG oscillators. Alternatively, the DMs deposited on FS, silicon and sapphire substrates demonstrate quite good surface quality and low losses (minimum $R = 99.968\,\%$, measured via the lossmeter described in section 3.3). The estimated correspondence of the total optical loss to a surface roughness of up to 3 nm (blue curve in figure 4.4) was obtained by implementing the following parameter values into equation 4.4: $T_0 = 0.01959\,\%$, $R_0 = 99.98041\,\%$, ϑ_i=7.5°,

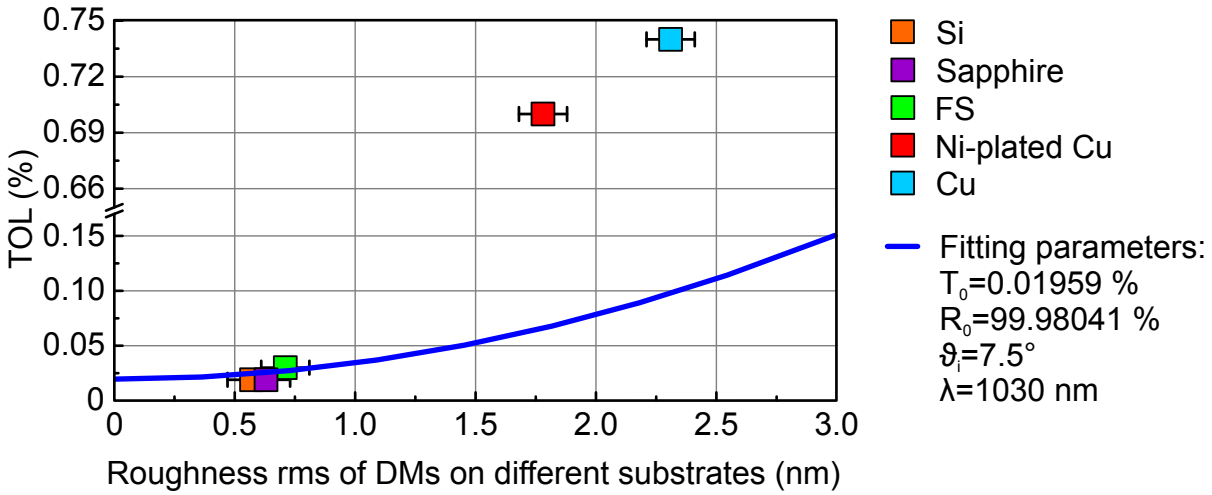

Figure 4.4: Dependence of the total optical loss TOL of the HDMs with –3000 fs^2 on the surface roughness σ_{rms} (the legend assigns the substrates used). Blue curve represents the simulated total optical loss TOL using equation 4.4 (the legend enumerates the parameters used). The values are averaged over a number of substrates and measurements.

λ=1030 nm. As one can notice, the simulated curve nicely fits the measured data for the DMs coated on FS, silicon and sapphire substrates, whereas the total optical loss of the DMs deposited on Cu and Ni-plated Cu is much higher than the predicted values. Although all the mentioned substrates were coated during the same process, such discrepancies might be justified by the fact that the surface quality of the whole area (25.4 mm) of Cu and Ni-plated Cu substrates (and thus, the DMs deposited onto them) is in reality worse than σ_{rms} of an arbitrarily selected area of 7×7 μm.

According to the performed investigations, the silicon (thermal conductivity coefficient 80–150 W/(m·K)) and sapphire (thermal conductivity coefficient 33–40 W/(m·K)) substrates appear to be the best candidates for high-power applications in Yb:YAG oscillators. FS substrates are commonly used substrates, however the poor thermal conductivity coefficient of this material is insufficient.

4.3 Highly-dispersive mirror with −10 000 fs^2

Scaling passively-mode-locked femtosecond laser oscillators to ever higher pulse energies calls for ever higher negative GDD in the cavity (as discussed in section

2.2). Meeting this requirement with an increasing number of bounces off dispersive mirrors tends to increase alignment sensitivity, round-trip losses, and an overall complexity of the system. Advancing femtosecond oscillator technology to higher peak as well as average powers relies on the development of HDMs with higher levels of dispersion. Generally, the larger the required bandwidth, the smaller the achievable mean value of GDD in dispersive mirrors [110, 112]. Recent studies [142] have shown that there are certain limitations for the maximum achievable negative value of GDD, which depend on the total thickness of coatings and the layer material combination. For multilayer structures based on the material pair Ta_2O_5/SiO_2 this value reaches −7000 fs^2 for a thickness of 9.8 μm. Today, state of the art coating technology allows the production of coatings with total physical thicknesses larger than 10 μm and reaching of even higher levels of GDD. Here an achievement of the maximum possible negative GDD allowed by this total design thickness and its successful application in an Yb:YAG TD oscillator is described. Data presented in this section has been published in E. Fedulova et al. Optics Express 23, 13788−13793 (2015).

4.3.1 Design considerations and production process

An implementation of a single HDM with a GDD of −10 000 fs^2 is a challenge due to the high sensitivity of the design performance to manufacturing errors. In view of this fact additional considerations had to be made. A method to circumvent manufacturing errors is presented in ref. [143], which can be considered as a generalization of the highly efficient needle optimization and gradual evolution techniques [86–88]. The "robust synthesis procedure" described in that work was used here. The beauty of this approach is that it takes manufacturing errors into consideration during the design process.

The design was optimized to have a GDD of −10 000 fs^2 and reflectance of 100 % (entitled HD1499 in house) for the wavelength range 1025–1035 nm. According to ref. [142], where the limits for the maximum achievable negative value of the GDD have been studied, the target GDD of −10 000 fs^2 is achievable for the specified spectral range and for the chosen thin film materials with modern coating technology. The layer thicknesses of the optimized multilayer structure are shown in figure 4.5.

The dependencies of the refractive index on wavelength is described by the Cauchy formula:

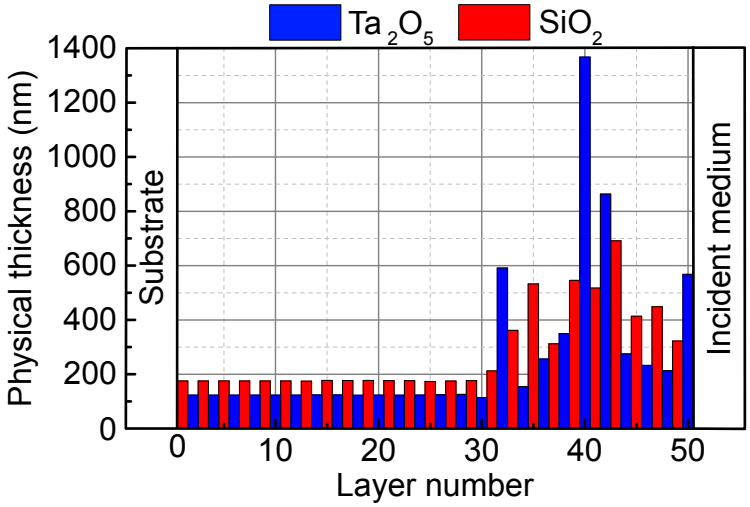

Figure 4.5: Physical thicknesses of the individual layers of the HDM with –10 000 fs^2. Red bars represent the low refractive index material SiO_2. Blue bars represent the high index material Ta_2O_5. The layers are displayed starting from a substrate. The bottom layer #1 is closest to the substrate, the top layer #50 is closest to the incident medium (air).

$$n(\lambda) = n_\infty + \frac{A}{\lambda^2} + \frac{B}{\lambda^4}\,, \tag{4.5}$$

where λ is the wavelength expressed in microns. The coefficients n_∞, A and B for the substrate and coating materials are presented in table 4.2. The design obtained via the robust procedure described above consists of 15 pairs of alternating quarter-wave layers (corresponding to the central wavelength of 1030 nm) of Ta_2O_5 and SiO_2, the material pair which is usually used for low loss coatings with relatively small bandwidths (200–300 nm), and 20 chirped top layers, resulting in 50 layers and a total thickness of 13.7 μm. Production of the multilayer design was achieved

	n_∞	A	B
FS	1.4433	4.06×10^{-3}	6.94818×10^{-6}
SiO_2	1.4653	0.0	4.71080×10^{-4}
Ta_2O_5	2.0657	1.6830×10^{-2}	1.686×10^{-3}
Nb_2O_5	2.2185	2.1827×10^{-2}	3.99968×10^{-3}

Table 4.2: Cauchy coefficients for the substrate and layer materials.

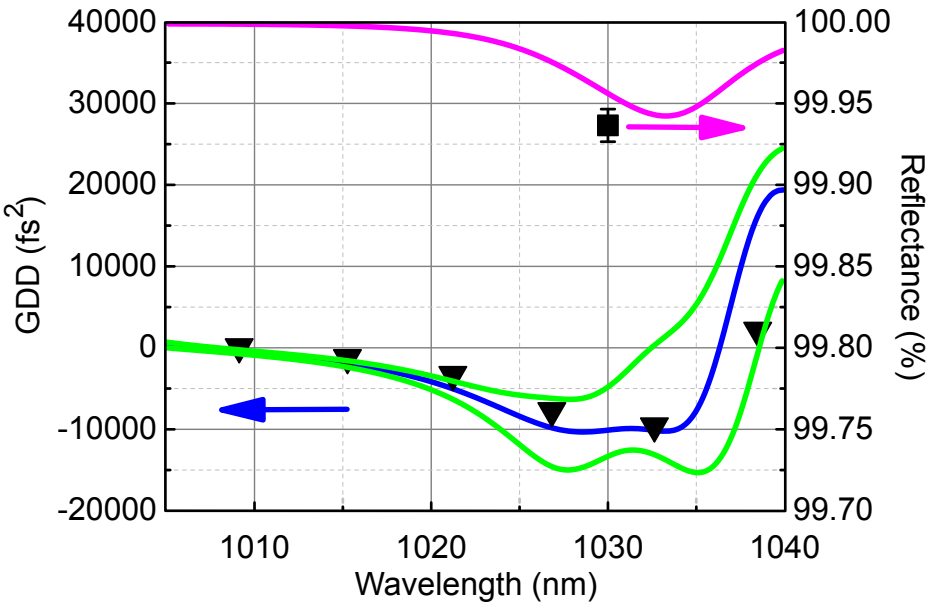

Figure 4.6: Comparison of the designed and measured data for the new HDM with –10 000 fs²: The designed GDD for AOI=3° (blue curve), error bars ± 0.5 nm (green curves); the measurement performed with a WLI at AOI=3° (black triangles). The designed reflectance for AOI=7.5° (magenta curve), the square at 1030 nm represents the measurement performed with a lossmeter at AOI=7.5°.

with the magnetron sputtering technique described in section 3.2. A standard FS substrate with a diameter of 25.4 mm and a thickness of 6.35 mm was used during the coating process. The produced samples were characterized with the help of the home-built WLI and the lossmeter (see section 3.3). The comparison of the designed and measured data is presented in figure 4.6, revealing a good agreement between theory and experiment. Most importantly, the agreement is particularly good in the relevant (1025–1035 nm) wavelength range. The result proves the feasibility of robust HDMs with negative GDD relying on physical thicknesses in excess of 10 μm.

4.3.2 Implementation in Yb:YAG TD oscillator

The advantage of having only one mirror providing the GDD is that fewer mirrors can be used to build a working cavity. This improves the stability and simplifies the alignment since fewer degrees of freedom need to be taken into account and fewer surfaces are prone to optical damage. The use of fewer mirrors also establishes the

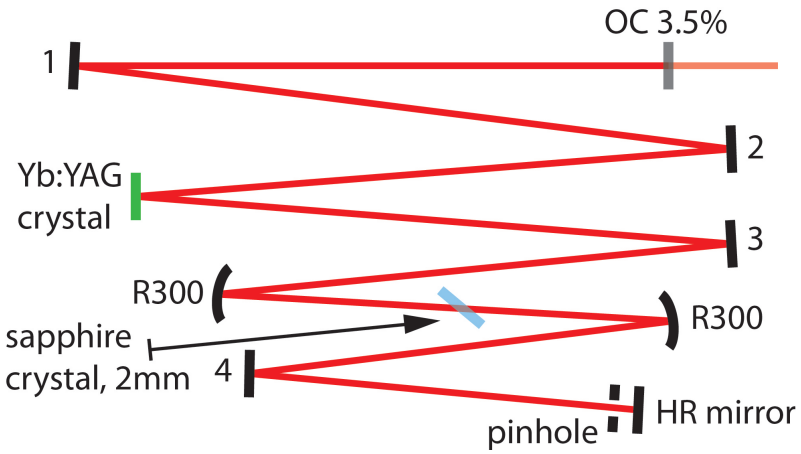

Figure 4.7: Schematic of the oscillator built for testing the intracavity behavior of the new HDM with –10 000 fs^2. The oscillator is a basic diode-pumped KLM Yb:YAG TD laser. OC, output coupler. R300, HR mirrors with radius of curvature ROC=300 mm. Mode-locking was achieved by hard aperture KLM with the sapphire crystal and a pinhole. Mirrors 1 to 4 were either a set of 4 known DMs with a total roundtrip GDD of –20 000 fs^2 or 3 HR mirrors and the new HDM with the same amount of GDD. During the measurements the oscillator ran at 33.7 MHz repetition rate with an output power of ~4 W.

possibility to build shorter cavities with higher repetition rates.

The first application of the newly-created HDM (for more details see ref. [144]), a source of GDD required to implement stable KLM in an Yb:YAG TD laser, is presented here. The basics of the KLM method were discussed in section 2.4. In order to test the new HDM four standard DMs from [110] (3 bounces on −3000 fs^2 mirrors and 1 bounce on a −1000 fs^2 mirror in a reference setup) were replaced by three highly-reflective (HR) mirrors and the new HDM (test setup), providing the equivalent GDD, namely −20 000 fs^2 per roundtrip. The beam radius (at 1/e^2) at the new HDM surface was 1.24 mm. The oscillator used was a basic diode-pumped Yb:YAG TD oscillator in which mode-locking was achieved by hard-aperture KLM with a 2-mm sapphire crystal serving as the nonlinear Kerr medium (figure 4.7). The oscillator was operated in the mode-locked regime at a repetition rate of 33.7 MHz with an average output power of approximately 4 W.

The spectra and the autocorrelation functions (ACF) of the pulses were measured for both setups. Figure 4.8 provides evidence that the measured curves fit the expected sech^2-function well. The spectra are centered around a wavelength of 1030.5 nm with a full width at half maximum (FWHM) of 4.2 nm in the reference

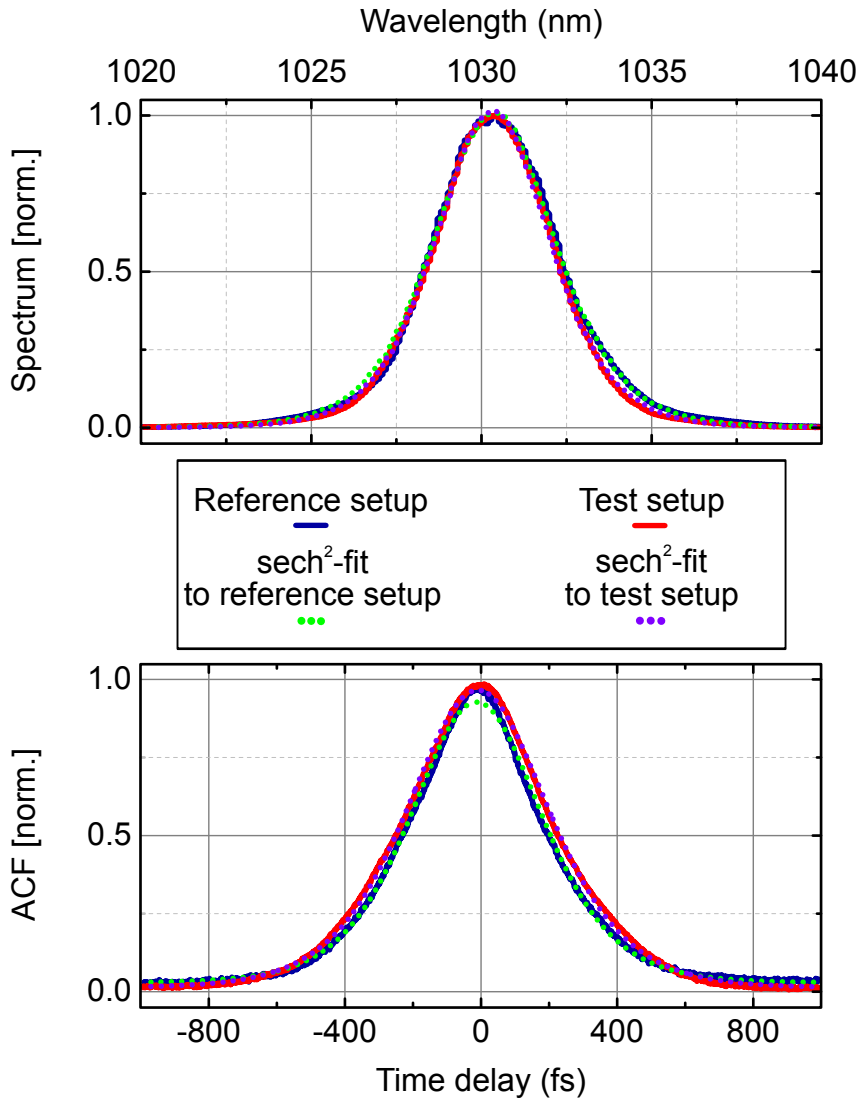

Figure 4.8: Comparison of spectra (top) and autocorrelations (bottom) of a basic KLM Yb:YAG oscillator working with the known mirror set and with the new HDM with –10 000 fs^2. In both graphs the color coding as follows: measured data with reference setup (blue solid curve), measured data with test setup (red solid curve), fitted sech^2-function to reference data (green dashed curve), fitted sech^2-function to test data (violet dashed curve). The spectra are centered around a wavelength of 1030.5 nm with a FWHM of 4.2 nm in the reference case and 3.9 nm in the test case. Pulse durations of 290 fs and 320 fs in the reference and test setup respectively were calculated from their autocorrelation via $\tau_\mathrm{p} = \tau_\mathrm{ac}/1.543$, where τ_p is the FWHM of the pulse intensity and τ_ac is the FWHM of the intensity autocorrelation.

case and 3.9 nm in the test case. Pulse durations of 290 fs and 320 fs in the reference and test setup respectively were calculated from their autocorrelation via $\tau_p = \tau_{ac}/1.543$ (ref. [1], p. 477), where τ_p is the FWHM of the pulse intensity and τ_{ac} is the FWHM of the intensity autocorrelation. Since realignment of the cavity between the two experiments is unavoidable it cannot be concluded that the slight difference in spectral width and pulse duration is solely attributed to the advanced HDM.

The main benefit of the HDM developed in the present study is the possibility to obtain high negative GDD in a single optical element. The HDM under consideration operates perfectly in a laser system and exhibits total optical losses of 600 ppm. HDMs having a GDD of -4000 fs^2 with total optical losses of 1000 ppm and a GDD of -3000 fs^2 with total optical losses of 300 ppm were demonstrated in ref. [112] (see figure 4.2). The presented HDM possesses over twice the GDD without the expense of introducing further losses.

It should be noted that although the output peak power was rather low (about 0.4 MW), the experiments described were performed in order to demonstrate a feasibility of both a successful production and implementation of the HDM with an extremely high value of GDD in the wavelength range of 1025–1035 nm. A standard FS substrate was used due to the same reason. Also, it is important to mention that the rather large thickness of the produced coating may lead to a reduction in the damage threshold or to thermal effects, such as expansion and deformation of the coating at higher intracavity powers. The exact laser induced damage threshold (LIDT) determination for the new HDM operated in the intracavity was obstructed due to dust particles located both on top and inside the coating, unwanted appearance of Q-switching and possible degradation of the coating over long time operation. HDMs with a GDD of –10 000 fs^2 possessing higher damage thresholds and negligible thermal effects are in the process of development.

In summary, silicon and sapphire substrates have been found to be best suited for high-power applications in Yb:YAG oscillators if one desires to minimize the thermal effects appearing in the intracavity. Furthermore, a single HDM with a GDD reaching the value of –10 000 fs^2 in the wavelength range 1025–1035 nm has been presented. The recently reported robust technique has been used in order to circumvent manufacturing errors and to produce a challenging, rather thick (13.7 μm) coating with a large negative GDD for a central wavelength of 1030 nm. The produced HDM was successfully utilized in an Yb:YAG TD oscillator, operating at 33.7 MHz repetition rate with an output power of about 4 W with no conclusive degradation in the oscillator performance, which resulted in a pulse du-

ration of 320 fs. Employing fewer mirrors providing the required amount of GDD implies undeniable advantages, such as improved stability and simplification of the alignment of a working cavity. Using fewer mirrors with larger GDD provides the possibility to build shorter femtosecond laser systems with higher repetition rates and higher pulse energy levels in femto- and in the near future, attosecond physics applications.

Chapter 5

Nonlinear effects in dielectric multilayer coatings

Dielectric multilayer coatings are fundamental to almost all kinds of laser systems and have therefore significantly contributed to progress in optics. High-power lasers, for example, heavily rely on HR mirrors, and DMs are indispensable for dispersion control in ultrafast science. The design of the dielectric coatings enables a highly flexible control of almost the entire range of linear optical properties, such as reflectance, bandwidth, phase and dispersion. Nonlinear optics, however, is still mostly based on bulk materials with mm-sized dimensions. A prominent mechanism is the optical Kerr effect, which can be viewed as an intensity-dependent change of refractive index (see chapter 2). Two technologically important consequences of the Kerr effect are self-focusing, used for laser mode-locking, and self-phase modulation, used for compressing laser pulses to few-cycle duration. The quasi-instantaneous response time of several femtoseconds of the Kerr effect [62] is essential for both applications. Adopting the optical Kerr effect for laser technology has enabled a plethora of ultrafast applications, ranging from the ultrafast light gate [55] to spawning the revolutionary KLM technique [28], from near at hand light modulators presented here to potential all-optical computers. Previous implementations of nonlinear multilayer mirrors have not been based on the Kerr effect, but rather relied on nonlinear absorption [145] or frequency conversion [146]. However, a lossless element is essential for many applications, in particular within lasers or enhancement cavities. To this end, dielectric oxide films with low losses (in contrast to metals) come into sight as promising sources of nonlinearity. Moreover, dielectric materials are appealing as they are highly resistant to laser damage, can excellently withstand abrasion and environmental influence, as well as due to the maturity of available deposition technologies.

In this chapter, a comprehensive research at the intersection of several fields:

thin film coatings, nonlinear optics and ultrafast physics, is realized. It experimentally demonstrates dielectric optical coatings with nonlinear behavior dominated by the optical Kerr effect, created in order to produce a device with almost instantaneous nonlinearity and, preferably, low losses. This idea has not, to date, transcended theoretical investigations [147]. In many simulations foreshowing a strong nonlinear response of dielectric multilayer structures, authors have used materials (often not specified) with overestimated values for Kerr coefficients [148–152]. In reality, the fundamental challenges of experimental observation of the optical Kerr effect emerge from the comparatively small nonlinear refractive indices of dielectric materials [62, 153, 154] and the necessity to work at high intensities. Here, the design guidelines for creating multilayer structures in which the overall optical response is made extremely sensitive to slight changes of the layer refractive indices are presented. The result is a Kerr-effect-driven dielectric multilayer element with intensity-dependent reflectance and transmittance. Specifically, reflectance increases at higher intensities, making the device potentially useful for mode-locking applications. This result holds the prospect for devices purely based on dielectric materials and the optical Kerr effect—nonlinear multilayer coatings (NMCs)—allowing nearly-lossless operation for future applications [155].

This chapter introduces the novel NMC elements for the NIR spectral region, the particular choice of the dielectric materials for which is justified in section 5.1. Further on, the design considerations and production of the NMCs are treated in section 5.2. Finally, the explicit nonlinear, pre-damage, Kerr effect-driven behavior of the manufactured NMCs is thoroughly studied using different approaches such as laser characterization (section 5.3), spectrophotometry (section 5.4) and the pump-probe technique (section 5.6). Additionally, some possibly relevant effects previously observed in multilayer coatings are briefly addressed in section 5.5. Partly, data presented in this chapter has been published in E. Fedulova et al. Optics Express 24, 21802-21817 (2016).

5.1 Optical Kerr effect in multilayers

The optical Kerr effect in a medium results in an almost instantaneously occurring intensity-induced change in the refractive index, and is described by equation 2.16 (section 2.2):

$$n = n_0 + n_2 I \,.$$

Here n_0 is the linear refractive index, n_2 [cm^2/W] is the second-order nonlinear refractive index, and I [W/cm^2] is the light intensity. For example, in a quartz crystal with n_0=1.5 and n_2=3 $\times 10^{-16}$ cm^2/W, a light intensity of about 10^9 W/cm^2 can cause observable nonlinearities [61]. The typical response time for the nonlinearity induced by the electronic polarization is 1 fs [62]. Through simulations, a significant reflectance increase of dielectrics dominated by the optical Kerr effect along with an increasing absorption has been deduced [147]. In order to enhance the impact of the optical Kerr effect, the optical characteristics of an NMC design need to be sensitive to slight changes in refractive index, considering that the nonlinear refractive indices of dielectric materials used for optical coatings are rather small (see table 5.1). Moreover, as discussed previously (see section 2.4) the GDD of the elements must be uniformly flat if utilized for mode-locking of lasers. In other words, the goal is to create a new class of multilayer structure with enhanced sensitivity to slight changes in refractive index, based on the Kerr effect and possessing controlled constant GDD over the desired wavelength range.

It has been established that the factors determining the nonlinear optical response of the simple oxides are very complex. However, it has been shown that the nonlinear refractive index increases with increasing linear refractive index and decreasing bandgap energy, which is attributed to an increase in metallicity [154]. Based on this observation, it has been suggested that materials containing PbO, TiO_2, Sb_2O_3, CdO, Ta_2O_5, Nb_2O_5, CeO_2, TeO_2, V_2O_5, Bi_2O_3, MoO_3, WO_3, MnO, Fe_2O_3, CoO, and NiO in appropriate amounts would be promising materials for nonlinear optics.

Previously, it has been shown that the nonlinear refractive index depends on the proximity of the test wavelength to the bandgap, and scales in proportion to the inverse fourth power of the bandgap energy E_g [156]:

$$n_2 \sim E_g^{-4} \tag{5.1}$$

For transparent crystals and glasses, n_2 is normally on the order of 10^{-16}–10^{-14} cm^2/W [157]. SiO_2, with the bandgap energy E_g~8.3 eV, has a relatively low nonlinear refractive index of 3 $\times 10^{-16}$ cm^2/W [157], whereas some chalcogenide glasses exhibit several hundred times higher values. Semiconductor materials also possess rather high nonlinear index values.

There are several oxide materials available for the the magnetron beam sputtering technique, which is the method of choice, as stated previously (see section 3.2). These oxide materials, together with their respective bandgaps, linear and

nonlinear refractive indices at the indicated wavelengths are summarized in table 5.1. The linear refractive indices are taken from the online database [158], and might differ slightly from the indices obtained with the Helios plant described in section 3.2. It is also important to keep in mind that the nonlinear indices were measured for bulk materials only, and these values can only be used as an estimate for the according thin film properties.

The first three oxides in the table 5.1, TiO_2, Nb_2O_5 and Ta_2O_5, are the best candidates out of the presented group of the coating materials due to their low bandgap energies. The nonlinear refractive index of bulk rutile TiO_2 is known to be 30 times that of silica (see table 5.1). However, TiO_2 appears to be a tricky material to sputter: Producing titania thin films of good quality is challenging since this material has several states with different optical properties (such as rutile or anatase for instance). Moreover, the relatively slow deposition rates cause instability in the coating process, which evokes instability of the refractive index of magnetron-sputtered TiO_2 (it lies in the range of 2.15–2.45 in our case). Apart from this issue (which has possible solutions as described in [167]), TiO_2 is an extremely attractive material to use in view of its high nonlinearity and vanishing two-photon absorption (2PA) around 800 nm [159].

Adair et al. [153] have presented both measured and calculated nonlinear refractive indices (in esu units) of a significant number of bulk optical materials. However, thorough studies of nonlinear refractive indices of the dielectric materials Nb_2O_5 and Ta_2O_5 widely used for multilayer dielectric coatings have not been reported in the available literature. Moreover, the thin film properties of all the coating materials remain unexplored. Dimitrov and Sakka have computed the coefficients n_2 (in esu units) for many oxides including TiO_2, Nb_2O_5 and Ta_2O_5 [154]. Although, when comparing the nonlinear refractive indices (in cm^2/W, not esu units) of Nb_2O_5 and TiO_2, they turn out to be equivalent [154]. Up to now, Tai et al. have determined n_2 in a Ta_2O_5 rib waveguide (sputtered 1 μm thick film on a Si wafer with a 2 μm thick buffer SiO_2 layer) at 800 nm based on SPM induced spectral broadening to be 7.23×10^{-15} cm^2/W at 800 nm [163]. Nevertheless, the works of Tai et al. and Dimitrov and Sakka [154] together with the bandgap energies of Nb_2O_5 and Ta_2O_5 allow one to assume that the typical values of n_2 for these high-index dielectric materials are on a scale of $(1\text{–}9)\times10^{-15}$ cm^2/W (using equation 5.1).

Further advantages of Ta_2O_5 are its transparency over a broad spectral range, which drastically reduces 2PA [168], and its high laser damage threshold. The linear absorption for a single layer of Ta_2O_5, produced by the same magnetron

Coating material	Linear refractive index n_0 @ 1030 nm	Nonlinear refractive index n_2, cm^2/W	Bandgap energy E_g, eV
TiO_2 (Titanium dioxide, Titania)	2.48	2.1×10^{-15} [154], 7.9×10^{-15} @ 800 nm [159], 9×10^{-15} @ 1060 nm [153]	3 [154], 3.3 [160]
Nb_2O_5 (Niobium pentoxide)	2.26	2.1×10^{-15} [154]	3.4 [154, 161], 3.49 [162]
Ta_2O_5 (Tantalum pentoxide, Tantala)	2.08	7.23×10^{-15} @ 800 nm [163], 2.6×10^{-15} [154]	3.8 [160], 4 [154]
HfO_2 (Hafnium dioxide, Hafnia)	2.08	not found	5.1–6 [164][a]
ZrO_2 (Zirconium dioxide, Zirconia)	2.12	1.2×10^{-15} @ 1060 nm [153]	5–7 [165], [164][a]
Al_2O_3 (Aluminium oxide, Sapphire)	1.76	2.9×10^{-16} @ 1060 nm [153], 4×10^{-16} [154]	6.5 [160], 6.2–7 [164][a]
SiO_2 (Silicon dioxide, Silica, Quartz)	1.45	2.2×10^{-16} [166], 2.7×10^{-16} @ 1500 nm [157], 3.1×10^{-16} @ 1060 nm [153]	8.3 [160], 8.9–9 [164][a]

Table 5.1: Coating materials available for magnetron beam sputtering. The values for linear refractive indices n_0 are taken from the online database [158]. If originally presented in esu, the values for n_2 in cm^2/W were calculated via $n_2\left[\frac{cm^2}{W}\right] = 4.19\times10^{-3}\frac{n_2[esu]}{n_0}$ [157]. The values for nonlinear refractive indices n_0 are presented for a wavelength of 1030 nm unless stated differently.

[a] and references therein

sputtering plant used in this work, has been estimated to be $\sim 0.8 \times 10^{-3}$ [145]; the linear absorption for Nb_2O_5 is usually somewhat higher. Despite the latter fact and the fact that the threshold fluence for Nb_2O_5 has been found to be slightly lower compared to that of Ta_2O_5 [169], it remains a promising material with its high nonlinear index. Therefore, Ta_2O_5 and Nb_2O_5 were chosen as two different high-index materials for the first realizations of the new dielectric multilayer devices. The linear absorption for a single layer of SiO_2, which was used as the low-index material, has been found to be $\sim 10^{-4}$ [145].

5.2 Design, fabrication and characterization of NMCs

In the past, considerable attention has been given to different types of nonlinear optical materials and devices [170] for their ability to tailor the intensity, as well as the spatial and temporal profile of laser pulse trains. Silicon [171, 172], silicon-organic [173] and silicon-inorganic hybrids [174] possessing rather large nonlinear refractive indices, together with phase-change materials [175] are of high interest for ultrafast all-optical signal processing. A mirror structure, the nonlinear optical response of which is mostly governed by the electric field distribution inside the embodied gold film, may be useful for all-optical applications [176]. The nonlinear response of dielectric dispersive mirrors in the visible spectral range has been shown to be dominated by 2PA [145]. An optimized stack of dielectric thin films has been demonstrated to generate the third harmonic [146]. In contrast to all previous works, this thesis is concerned primarily with multilayer dielectric structures for the near-infrared spectral region (namely 1030 nm) operating at high intensities on the order of 10^9 W/cm^2.

5.2.1 Design considerations

It is possible to exploit the optical Kerr effect to develop 1) devices working in transmission and 2) devices working in reflection. Furthermore, there can be several types of elements operating in reflection: a) devices working in the middle of the reflectivity zone, and b) devices whose design is extremely sensitive to a change of refractive index. The GDD of such structures must be carefully tailored and remain constant over the desired wavelength range if used for mode-locking of lasers. As a matter of fact, the slope of a conventional QWS mirror can be

interpreted as a device of type b). Although, the GDD of a QWS mirror is zero at the central wavelength, a standard 6.35 mm FS substrate may cause self-focusing complications (see subsection 5.3.1). To emphasize the difference in the design approaches, it is important to state that the possible refractive index modifications are taken into account during the design process in our case. This is not the case when designing a conventional QWS mirror where only constant refractive indices are usually considered.

An important advantage of the a-type NMC (figure 5.1(a)), designed for operation in reflection, is its broad bandwidth, which can result in the generation of pulses in the range of several fs, although an absolute increase of reflectance is unlikely to exceed several percent. The second type (graphs (b) and (c) in figure 5.1) of NMCs, on the other hand, is extremely responsive to an intensity increase. The working range of the edge filter design is the edge itself (figure 5.1(b)), the position of which can be easily adjusted by varying the AOI of the incident light, thus influencing the modulation depth of the device. However, the estimated bandwidth of the edge filter design (figure 5.1(b)) is 10 nm, which would limit the pulse duration down to 100–200 fs (at 1030 nm). Additionally, it is possible to create an edge filter with an opposite slope resulting in decreasing reflectance (increasing transmittance) for increasing laser intensity. Another example is a so-called "resonant structure" (figure 5.1(c)) consisting of two QWS mirrors and a full-wave cavity in between (Fabry-Perot filter). A salient feature of a resonant structure is the electric field enhancement in the cavity. The latter fact means that much lower intensities are required for approaching the nonlinear regime. It is also evident that the rising slope of a resonant structure can be used to achieve decreasing reflectance (increasing transmittance). More complicated multiresonant structure embodiments can be designed in order to further amplify the optical Kerr effect.

The edge filter design (figure 5.1(b)), extremely sensitive to small refractive index variations in the transition zone between high and low reflectance around 1030 nm, was chosen for the first implementation of the NMC idea [155]. The Abeles matrix method [89, 90], discussed in section 3.1, for a given wavelength λ determines the initial reflectance R_i of an m-layer structure through the physical thicknesses of the layers $d_1, ..., d_m$, and the AOI ϑ:

$$R_i = R\,(d_1, ..., d_m;\, n_H,\, n_L;\, \lambda;\, \vartheta), \tag{5.2}$$

where n_H and n_L are the refractive indices of the high-index and low-index materials comprising the multilayer stack, respectively. In simplified form, the optical

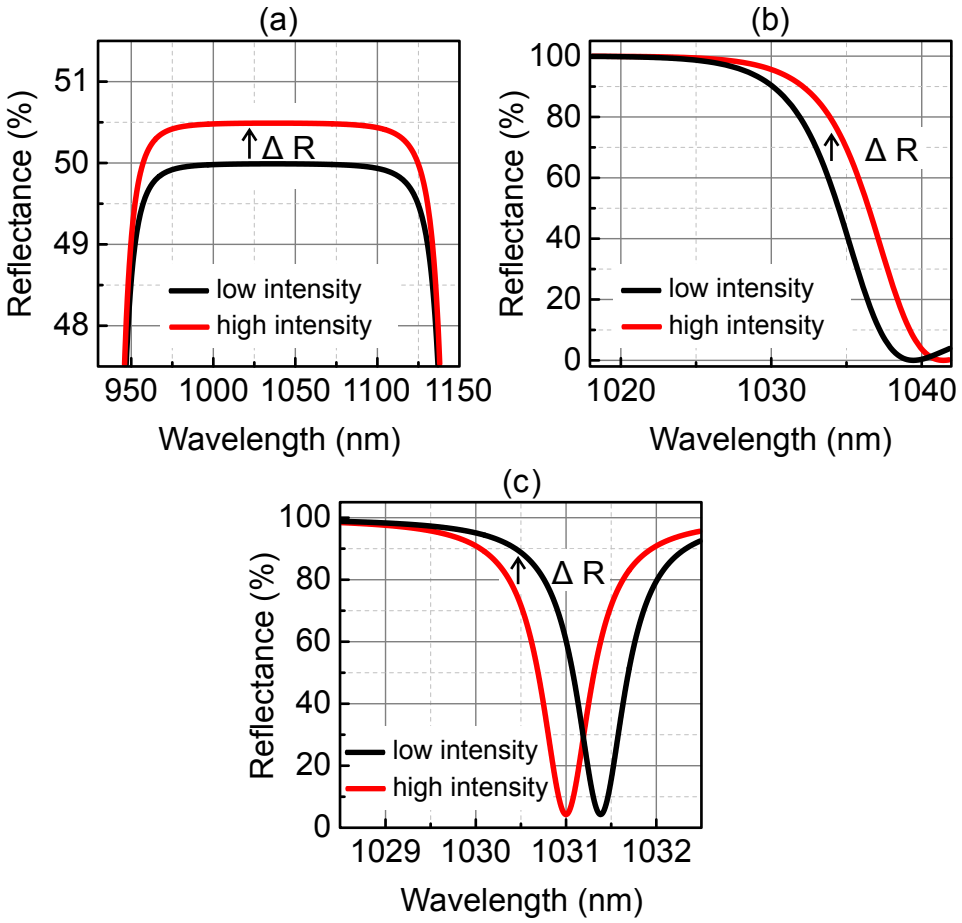

Figure 5.1: The optical Kerr effect illustration. Examples of designs enhancing the observable optical Kerr effect: (a) An example of a broadband NMC working in the middle of the reflectivity zone, (b) Edge filter – an example of an NMC whose design is extremely sensitive to refractive index variations, (c) Resonant structure – another example of an NMC whose design is extremely sensitive to refractive index variations.

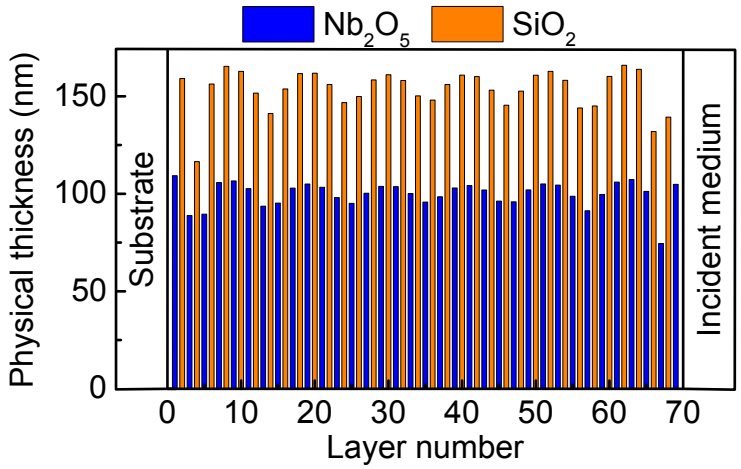

Figure 5.2: Physical thicknesses of the individual layers of F502. Orange bars represent the low refractive index material SiO_2. Blue bars represent the high refractive index material Nb_2O_5. The layers are displayed starting from the substrate. The bottom layer #1 is closest to the substrate, the top layer #69 is closest to the incident medium (air).

Kerr effect in multilayer coatings can be described as follows. The incident laser beam interferes with itself in the multilayer structure and, consequently, manifests a standing wave distributed along the coordinate perpendicular to the coating surface. Due to the presence of such a standing wave, a weak increase in layer refractive indices, corresponding to the field intensity profile, emerges in accordance with equation 2.16. The latter can also be considered as an additional microstructure, which in turn leads to an increase in reflectance of the whole multilayer structure from R_i at low intensities up to its final value R_f at higher intensities:

$$R_f(I) = R_i + \triangle R(I), \tag{5.3}$$

where $\triangle R(I)$ is the modulation depth of the NMC (see figure 5.1(b)).

The first realization of an NMC (F502) with a central wavelength of 1030 nm consisted of 69 alternating layers of the dielectric materials Nb_2O_5 as the high-index material and SiO_2 as the low-index material (figure 5.2), resulting in a total physical thickness of 8.7 μm. Another realization, F503 (figure 5.3) was obtained with the dielectric materials Ta_2O_5 and SiO_2, with a total physical thickness of 9.2 μm. As this was a first proof of principle study, the GDD curves of both NMCs F502 and F503 were not optimized and remain uncontrolled. In contrast to the initial two, the next realization of an NMC, F504 was designed to have

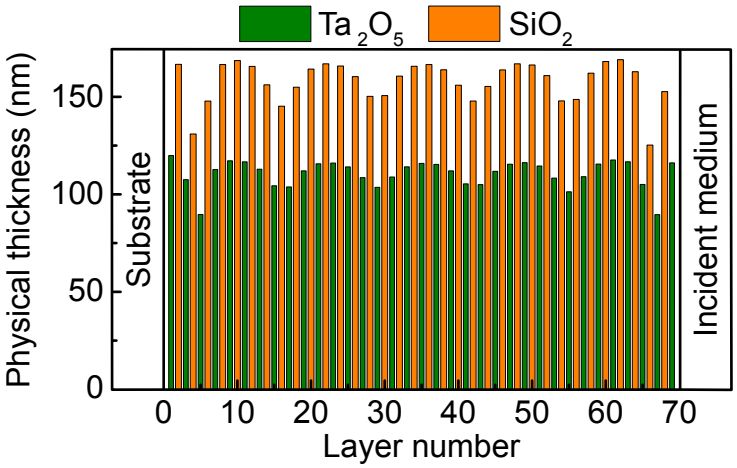

Figure 5.3: Physical thicknesses of the individual layers of F503. Orange bars represent the low refractive index material SiO_2. Green bars represent thehigh refractive index material Ta_2O_5. The layers are displayed starting from the substrate. The bottom layer #1 is closest to the substrate, the top layer #69 is closest to the incident medium (air).

an optimized flat GDD of -5000 fs^2 over the wavelength range 1024–1033 nm, essential for potential laser applications. The design NMC F504 corresponds to a central wavelength of 1030 nm and consists of 69 alternating layers of Ta_2O_5 and SiO_2, resulting in a total thickness of 9.3 μm (figure 5.4).

The presented designs are highly sensitive to manufacturing errors; a slight change of any layer thickness would shift the central wavelength of the slope drastically. As already noted, the position of the slope can be simply tuned via the AOI. Therefore, all three NMC designs were tailored for a non-zero AOI = 20°. An advantage and at the same time an alignment challenge of the edge filters when used in a setup originates from this angular sensitivity. Figure 5.5 depicts how the slope position of the F504 design changes remarkably when the AOI is varied in a minor range from 19° to 22° at a wavelength of 1030 nm.

5.2.2 Fabrication and characterization of NMCs

The designed multilayer structures were deposited on two kinds of FS substrates: 1) 145 μm thick, 10 mm diameter and 2) 6.35 mm thick, 25.4 mm diameter by means of the magnetron sputtering technique described in section 3.2. The produced samples were characterized with the help of the industrial spectrophotometer (Perkin Elmer Lambda 950) and the WLI (see section 3.3). The comparison of the

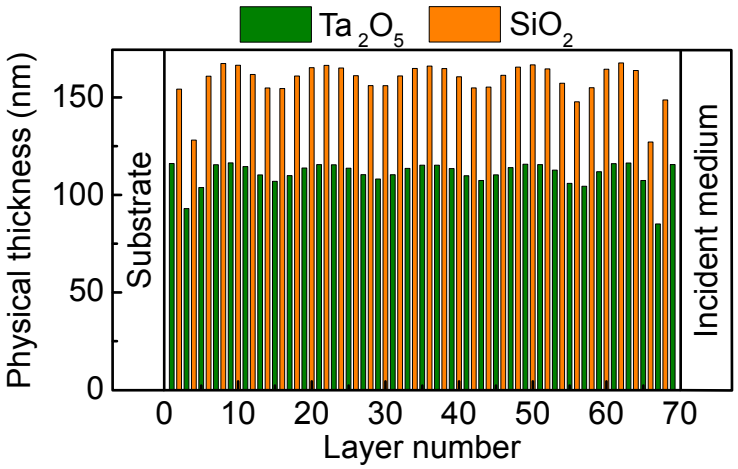

Figure 5.4: Physical thicknesses of the individual layers of F504. Orange bars represent the low refractive index material SiO_2. Green bars represent the high refractive index material Ta_2O_5. The layers are displayed starting from the substrate. The bottom layer #1 is closest to the substrate, the top layer #69 is closest to the incident medium (air).

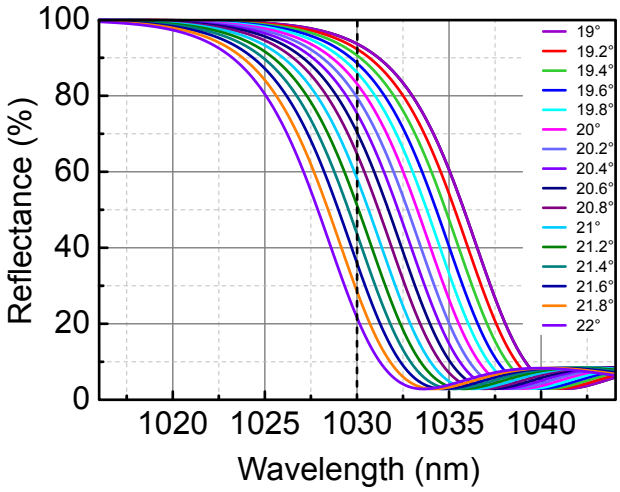

Figure 5.5: Theoretical angular sensitivity for the target design of F504 in the range from 19° to 22°. The legend enumerates different angles of incidence.

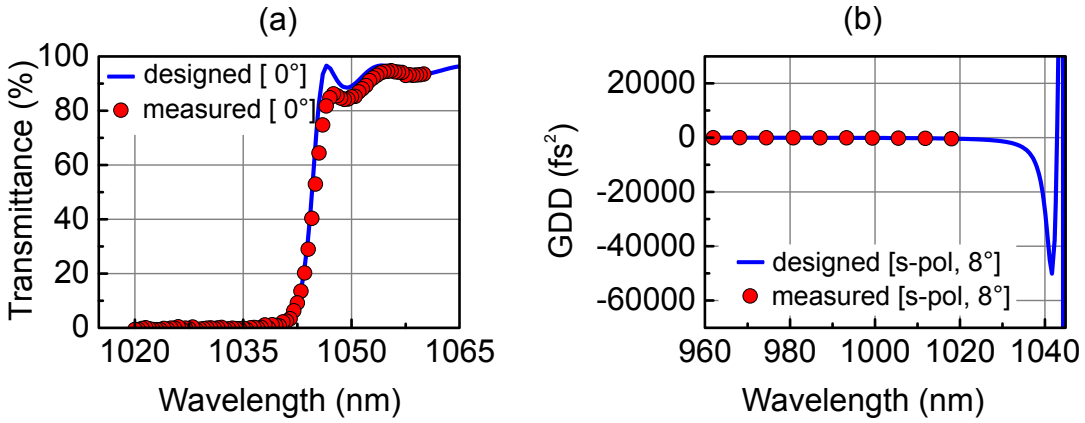

Figure 5.6: Comparison of the designed and measured data for F502: (a) The designed transmittance (blue curve) and the measured data (via spectrophotometer, red circles) at AOI=0°, (b) The designed GDD (blue curve) and the measurement performed with a WLI (red circles) for s-polarized light at AOI=8°.

designed and measured data is presented in figures 5.6–5.8, revealing imperfect agreement between theory and experiment data, as expected. The measured data matches the theoretical curves at different AOIs. This mismatching is, however, not important as it can easily be compensated for by tuning the AOI of the incident light at an NMC. Note also that even though the slit size of the spectrophotometer was set to the minimal 1 nm size, it might not have been possible to detect the proper steepness of the slope of the deposited NMCs.

5.3 NMCs with intensity-dependent reflectance

5.3.1 Laser characterization: experimental setup

The pre-damage behavior of the NMCs F502, F503 and F504 coated on 145 μm-thick substrates was studied experimentally with the setup shown in figure 5.9. The measurement setup included a Yb:YAG TD regenerative amplifier (central wavelength 1030 nm, pulse duration 1 ps, pulse energy 400 μJ) with a repetition rate of 50 kHz and a spatially Gaussian beam profile [177]. The pulse intensity was gradually varied with a half-wave plate followed by a polarization cube placed in front of the focusing lens.

All the optics described in this thesis were characterized in the pre-damage regime, therefore a way to detect the laser induced damage threshold (LIDT), in

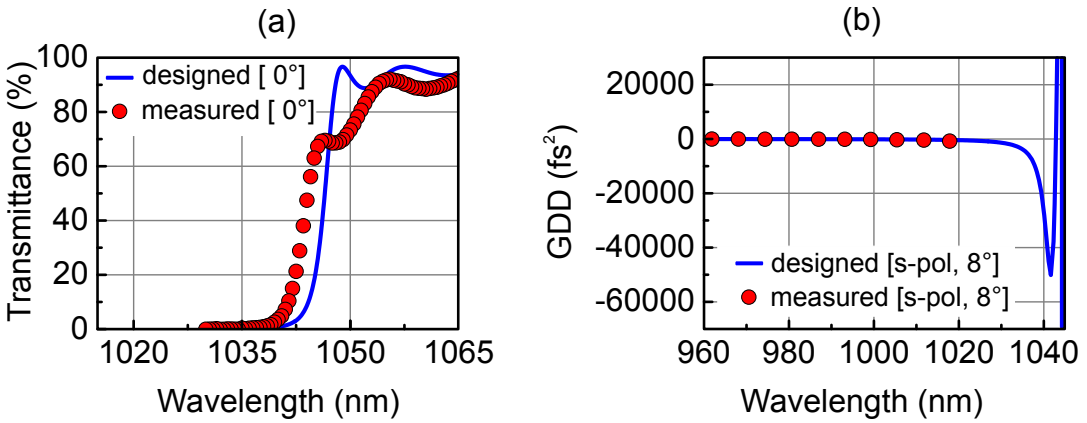

Figure 5.7: Comparison of the designed and measured data for F503: (a) The designed transmittance (blue curve) and the measured data (via spectrophotometer, red circles) at AOI=0°, (b) The designed GDD (blue curve) and the measurement performed with a WLI (red circles) for s-polarized light at AOI=8°.

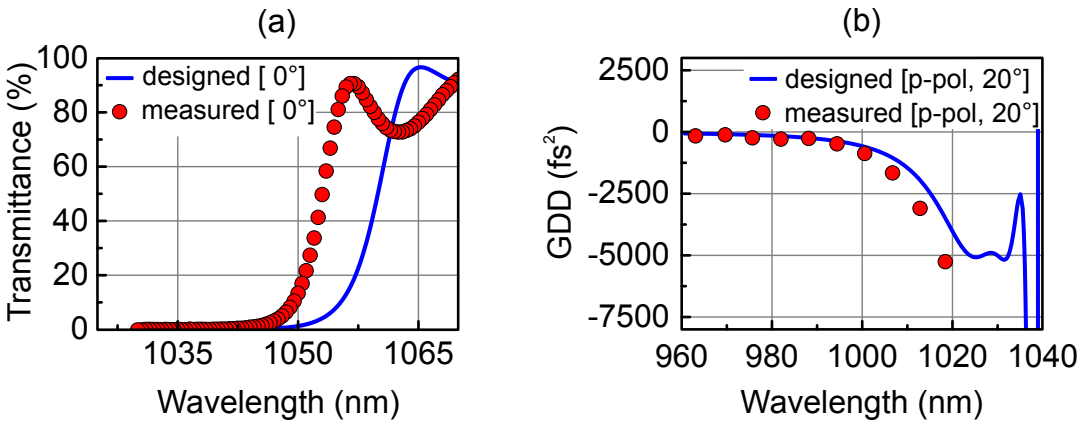

Figure 5.8: Comparison of the designed and measured data for F504: (a) The designed transmittance (blue curve) and the measured data (via spectrophotometer, red circles) at AOI=0°, (b) The designed GDD (blue curve) and the measurement performed with a WLI (red circles) for p-polarized light at AOI=20°.

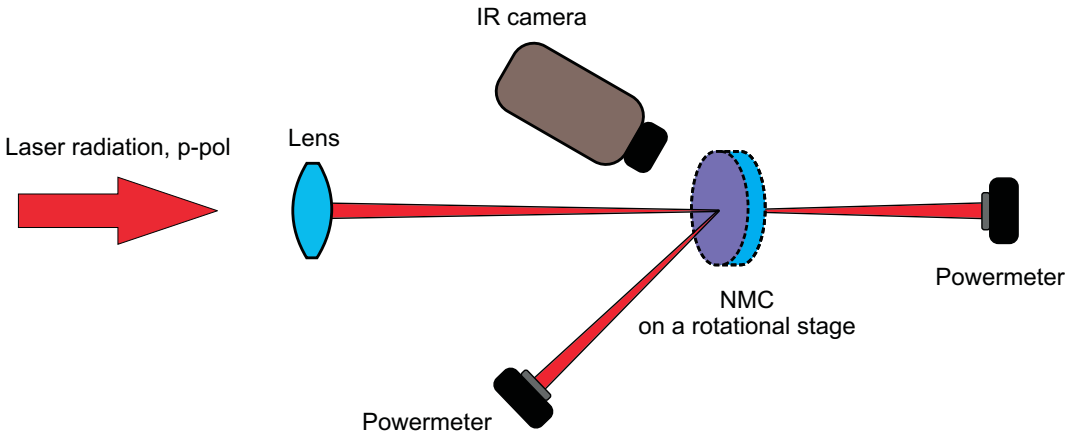

Figure 5.9: Schematic of the setup for measuring the change of reflectance, transmittance and relative temperature of the NMCs at increasing laser intensity. Laser radiation source is Yb:YAG TD regenerative amplifier: 1030 nm central wavelength, 50 kHz repetition rate, 1 ps pulse duration.

order to accordingly stop the measurements, was required. There are several standard and a few other methods of defining LIDT used by different groups [178–182], among which are: measurements based on plasma emission, and Nomarski microscopy – detecting any visible permanent sample modification. A rapid change of the scattering behavior of the sample has been used as a damage indicator by different authors [160, 183–185]. When illuminated with a laser beam, the surface of the sample reflects most of the light in a certain direction; there is only a small amount of scattered light. As damage occurs, the surface area exposed to a laser beam is altered to a crater-like topology, which results in a rapid increase of the scattered light. This rapid increase of the scattered light can be detected by a photodiode (PD) or a charge-coupled device (CCD) camera placed nearby the sample. The increase in surface scattering of the laser light at damaged sites has nowadays become a routine exploited in damage detection [186]. A comparison of the experiments exploiting different damage determining techniques have proven this method to be accurate with adequately small error [187]. Consequently, a strong escalation of the scattered light from the sample surface (figure 5.10), monitored with a CCD camera (IDS Imaging Development Systems GmbH), served as an indication of damage occurrence in the presented experiments [186].

The p-polarized laser beam was focused on a sample in order to provide inten-

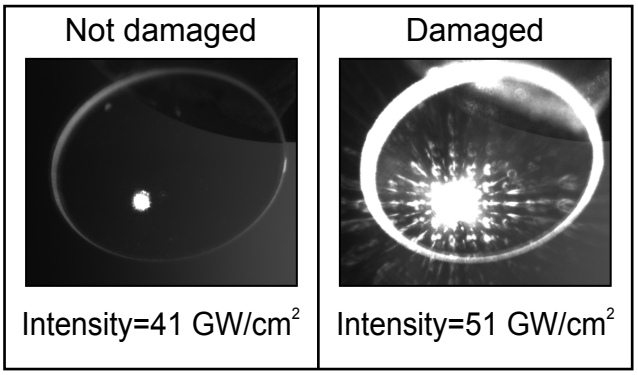

Figure 5.10: An example of a CCD camera image for NMC F502 at an incident laser intensity of 41 GW/cm^2 (not damaged sample) and 51 GW/cm^2 (damaged sample). The breakdown was observed as a distinct change of the scattered light off the illuminated spot.

sities up to slightly below the LIDT of the NMCs. Note that the peak intensity $\hat{I}$ for a Gaussian pulse, both temporally and spatially in the transverse direction, was calculated as follows [188]:

$$\hat{I} = \left(\frac{\pi}{2}\right)^{-\frac{3}{2}} \frac{\bar{P}}{f_{rep}\,\tau_p\,w_0^2}\,, \tag{5.4}$$

where $\bar{P}$ is the average power[1], f_{rep} is the repetition rate, τ_p is the pulse duration, and w_0 is the Gaussian beam radius – the $1/e^2$ radius, at which 86.5% of the maximum intensity is contained. For the sake of convenience, in future the peak intensity will be referred to simply as intensity. Notice also that the intensity values presented in this thesis should only be used as a guide due to imperfect beam radius estimation. Equation 5.4 may also be related to the pulse energy E_p, defined by the relation $E_p = \bar{P}/f_{rep}$ and the peak power $\hat{P}$, given by $\hat{P} = 0.94\,E_p/\tau_p$ for a Gaussian-shaped pulse. It should be mentioned that peak powers not higher than 75 MW (average power 4 W) were used for sample characterization, and the beam waste w_0 at the sample was rather large (about 180 μm at $1/e^2$ level).

Let us estimate possible self-focusing effects in FS substrates. For FS the critical power, according to equation 2.24, is P_{cr} ∼75 MW at 1030 nm. Plugging this value of the critical power and w_0 ∼180 μm at $1/e^2$ level (130 μm at 1/e level) into equation 2.25, we arrive at z_{sf} ∼10 mm. Thus, no self-focusing would occur in 6.35-mm FS substrates in this experimental geometry. On the other hand, many systems

[1]Dash ($^-$) is henceforth omitted.

operate at lower intracavity peak powers of 5–40 MW [117] requiring much tighter focusing, which may cause self-focusing over the 6.35-mm propagation distance of a standard fused silica substrate. In such thick substrates, self-focusing processes may alter the properties of the transmitted beam, which is detrimental for the potential laser applications. In order to characterize the potentially applicable laser components, the NMCs deposited on the particularly thin (145 μm) substrates were used over the course of the laser characterization.

Both the reflected and transmitted average power values were measured for each incident power value via a powermeter PM-10 (COHERENT). The reflectance R and transmittance T of the NMCs were obtained as follows:

$$R = \frac{P_{ref}}{P_{inc}} \times 100\%\,, \; T = \frac{P_{tr}}{P_{inc}} \times 100\%\,, \tag{5.5}$$

where P_{ref}, P_{tr} and P_{inc} are the measured reflected, transmitted and incident average powers respectively. The total losses TL were afterwards computed as:

$$TL = 100\% - R - T. \tag{5.6}$$

The relative temperature change of the sample was monitored during the measurements via an IR camera (FLIR SC 300 Series camera A325) with a measurement accuracy specified to ±2°C or ±2% of reading. The IR camera realized an additional control in monitoring damage occurrence, as the relative temperature increased rapidly at the onset of damage. The IR camera was set to measure the temperature difference $\Delta\,Temp$ between the spot where the laser hit the sample surface and the ambient medium. The IR camera was positioned in front of the sample at an angle of 30ř relative to its normal, so that a free path for the laser beam was ensured. The sample was placed on a rotational stage in order to adjust the angle of incidence and achieve different initial reflectance R_i to initial transmittance T_i ratios (R_i/T_i) at low intensities.

5.3.2 Laser characterization: experimental results

The measurements were performed in different sessions spanning over several months. Figures 5.11 and 5.12 illustrate the pre-damage behavior of the NMCs F502 (Nb_2O_5/SiO_2), F503 (Ta_2O_5/SiO_2) and F504 (Ta_2O_5/SiO_2, GDD = $-5000\,fs^2$) carried out using the setup described in the preceding section for R_i/T_i of 25/75, 50/50 and 80/20. The plots reveal evidence that the reflectance of all three samples increases, the transmittance decreases, the relative temperature grows with

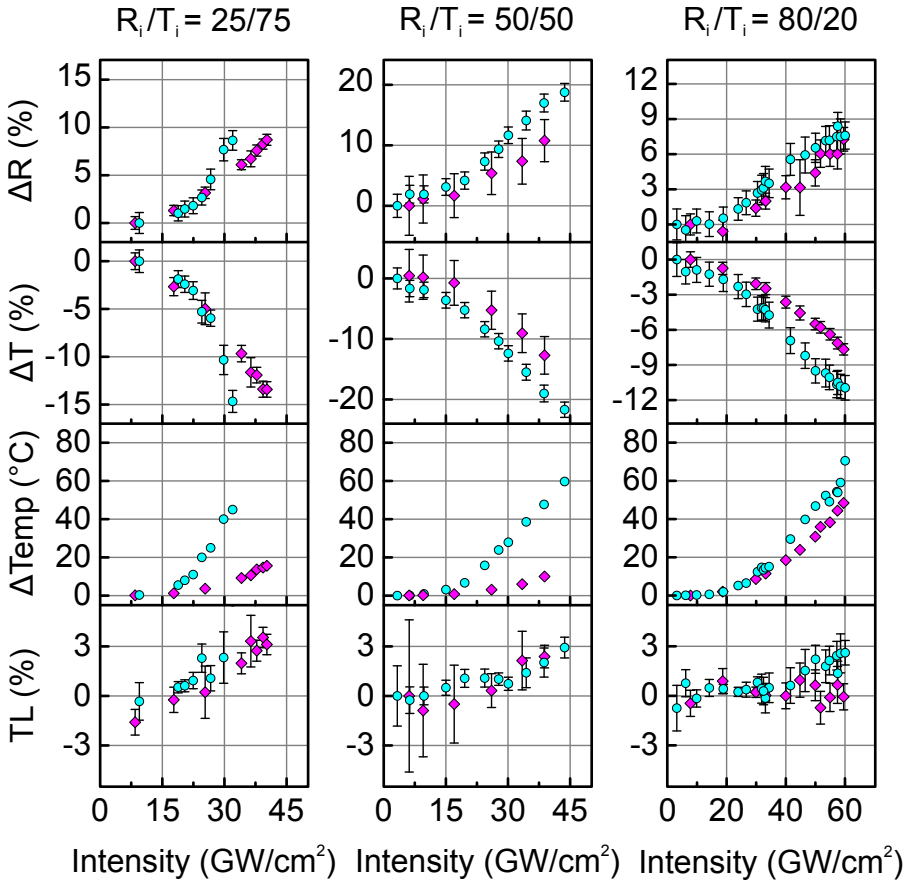

Figure 5.11: Change of reflectance, transmittance, relative temperature and total losses of NMCs F502 (magenta diamonds) and F503 (blue circles) for the ratios R_i/T_i of 25/75, 50/50 and 80/20. The last measurement point in each set of measurements is the point after which the damage occurred.

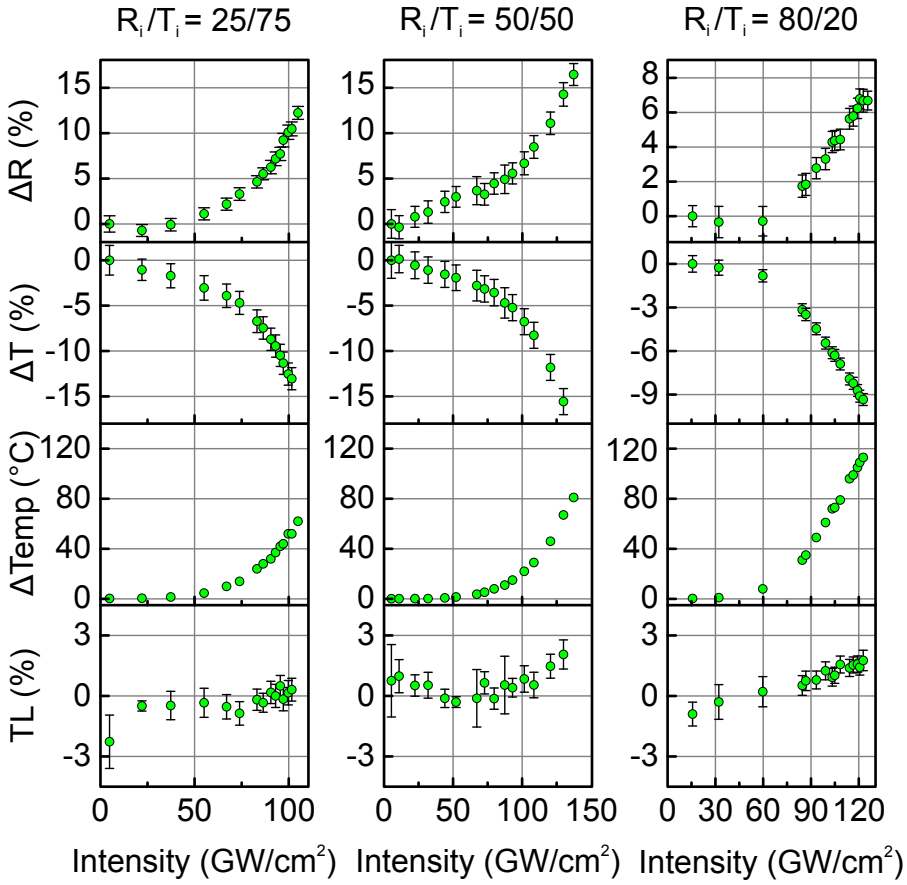

Figure 5.12: Change of reflectance, transmittance, relative temperature and total losses of NMC F504 for the ratios R_i/T_i of 25/75, 50/50 and 80/20. The last measurement point in each set of measurements is the point after which the damage occurred.

the incident intensity; the total losses are on the scale of measurement error.

The observed temperature growth could be justified by absorption, inevitable even in multilayer structures of high quality [189]. The discussion of the origin of absorption lies outside the present discussion, however, among the possible causes, the following might be important: multiphoton absorption (MPA) processes, dust particles and impurities, native defects (shallow traps, see section 5.5) [190], self-trapped excitons (deep traps, see section 5.5) subsequently leading to long-lived color center formations [182,191,192], or a complex combination thereof. At intensities on the order of 10^9 W/cm^2, absorption processes become relevant and result in the temperature increase. However, the extent to which absorption contributes to the total losses is not quantifiable as the latter lies within the measurement error (figures 5.11 and 5.12), which allows one to conclude that absorption is not the dominant process in the present case. On the other hand, the modulation depths for all F502, F503 and F504, both in reflectance and in transmittance, are well-defined and are certainly larger than the errors (figures 5.11 and 5.12).

It is also to be noted, that the measured relative temperature increase scales exponentially with the laser intensity. Comparable temperature dependence on the incident intensity in Ta_2O_5 thin films has been observed by Mero et al. [182] and has been attributed to incubation effects (discussed below in section 5.5) for the multi-pulse exposure case. The researchers [60, 160, 187, 193] usually try to avoid incubation effects by reducing the repetition rate of the laser or moving the sample after each shot. However, for the 1-ps pulses used here most of the change in the damage threshold occurs due to either the first or second pulses [194,195].

The modulation depths of the NMCs are determined by the AOI (according position of the edge), which also defines the initial proportion R_i/T_i. Additional measurements were performed for NMC F502 at intensities ranging from 3 GW/cm^2 up to 63 GW/cm^2 (5% below the LIDT observed at 66 GW/cm^2 in this case) for different levels of R_i. As indicated in figure 5.13, the maximum modulation depths are observed for the central part of the slope: for R_i levels of about 30–50 %. It is evident, that the edge filter design is highly responsive to an intensity increase, and $\triangle R$ can reach 16 % under particular conditions (for $R_i/T_i = 50/50$).

The observed behavior was reversible, no hysteresis phenomena were present. The measured values remained the same regardless of the acquisition order. Figure 5.14 illustrates a representative measurement for NMC F504. First, the intensity was gradually increased (green circles), and varied arbitrarily (black circles) afterwards.

From these and other measurements it can be concluded that the damage inten-

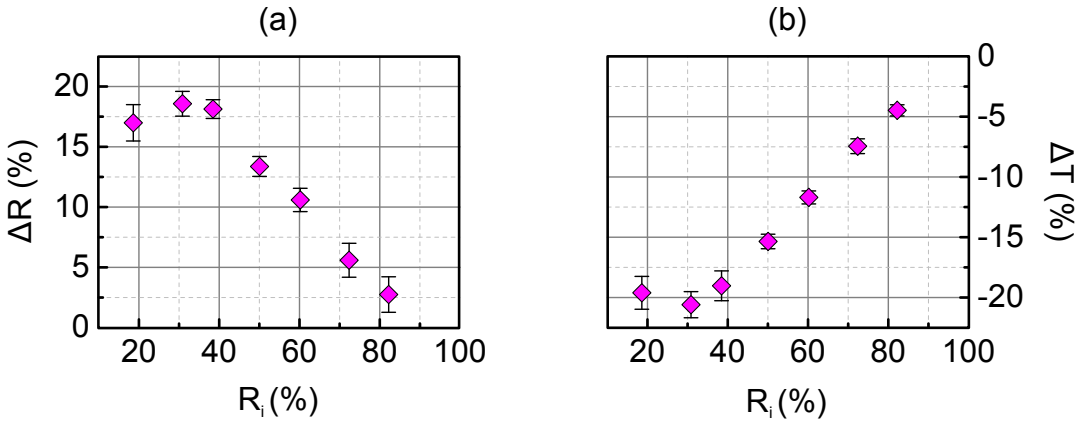

Figure 5.13: Dependence of the reflectance increase (a) and transmittance decrease (b) on the initial reflectance level R_i for NMC F502. The changes were measured over the intensity range 3 - 63 GW/cm^2, damage occurred at about 66 GW/cm^2. Data was kindly provided by T. Amotchkina.

sity for different samples of NMCs F502 varies between 30 and 110 GW/cm^2, for F503 – between 40 and 250 GW/cm^2, and for F504 – between 80 and 170 GW/cm^2. Random dust particles are present inside the coatings, and could explain such a significant discrepancy of the LIDT values. For comparison, the damage threshold intensity for an HDM consisting of 20 pairs of Ta_2O_5/SiO_2 [112] (see figure 4.2) placed in the same setup reached a value of 200 GW/cm^2. Usually, the damage threshold of Nb_2O_5/SiO_2 coatings is lower compared with that of Ta_2O_5/SiO_2 coatings [169], which is mostly the case for the results presented here as well (figures 5.11 and 5.12, compare the last measurement points). Note also, that the thin (145 μm) substrates cannot be polished as well as the standard (6.35 mm) ones, which might explain the reduced damage threshold values.

5.4 Temperature influence

As a temperature rise of the samples irradiated by the laser was observed (figures 5.11 and 5.12), studies were conducted in order to analyze the influence of temperature on the NMCs performance. Both theoretical estimations and experimental investigation were carried out and are presented in this section.

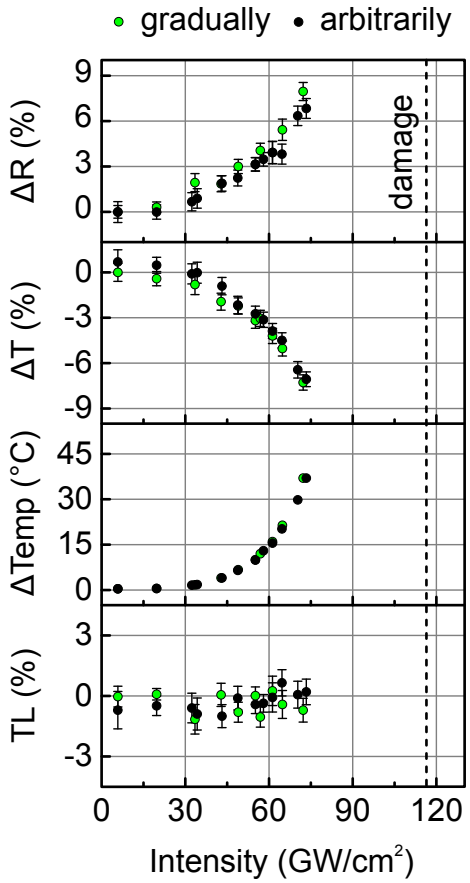

Figure 5.14: Reversibility of the nonlinear behavior of NMC F504 for the initial ratio $R_i/T_i = 50/50$. The intensity was varied both gradually (green circles) and arbitrarily (black circles). The dashed line is set at 116 GW/cm^2 – the intensity where damage occurred.

5.4.1 Theoretical estimations

The materials are known to expand in response to a change in temperature [196]. Optical coatings expand when heated as well. For an accurate characterization, it is necessary to determine the evolution of the optical properties of each layer material composing the multilayer stacks in response to a change in temperature. Therefore, knowledge of the physical parameters describing each dielectric material, such as the coefficient of thermal expansion α (CTE) and the thermo-optic coefficient β is required. Franc et al. have nicely summarized the thermo-mechanical and optical parameters for several optical coating materials (ref. [197] and references therein). The coefficients α and β for the dielectric materials used in this study are shown in table 5.2. However, these parameters have mainly been determined for single layers and are in general different for multilayer stacks. Moreover, the coefficients α and β of a single layer always depend on the deposition process. Thus, the coefficients α and β for the NMCs presented here most probably differ from those in the literature. Nevertheless, they suit well for theoretical estimations of the temperature impact.

As evident from table 5.2, Nb_2O_5 is more susceptible to temperature than Ta_2O_5: The CTE for the former is 1.6 times larger, and the thermo-optic coefficient is an order of magnitude higher than that of Ta_2O_5. One can estimate the change in reflectance due to thermal effects $\triangle R_{temp}$, for a certain temperature rise $\triangle Temp$, based on the coefficients above:

$$\begin{aligned} \triangle R_{temp} \;=\; & R\,(d_1(1+\alpha_1\cdot\triangle Temp),\ldots,\, d_m(1+\alpha_m\cdot\triangle Temp); \\ & n_H+\beta_H\cdot\triangle Temp,\, n_L+\beta_L\cdot\triangle Temp;\, \lambda;\, \vartheta) - R_i\ , \end{aligned} \tag{5.7}$$

where the coefficients n_H and n_L are, for instance, described by the Cauchy formula (equation 4.5) stated in section 4.3. Figure 5.15 demonstrates that the temperature rise has a considerable effect on the NMC F504 at $\triangle Temp = 113°C$ (observed during the laser characterization, see figure 5.12), and the reflectance increases by 4.7 % at a wavelength of 1030 nm from $R_i = 80$ %. The theoretical estimations based on the parameters given in table 5.2 will be presented in subsection 5.4.3 along with the experimental results.

Layer material	Thermal expansion coefficient α, K^{-1}	Thermo-optic coefficient β: dn/dT
SiO_2	0.51×10^{-6} [159, 198]	8×10^{-6} [159]
Ta_2O_5	3.6×10^{-6} [198–200]	2.3×10^{-6} [201]
Nb_2O_5	5.8×10^{-6} [200]	$\mathbf{1.43\times10^{-5}}$ [200]

Table 5.2: Thermo-mechanical and optical parameters for the layer materials at room temperature.

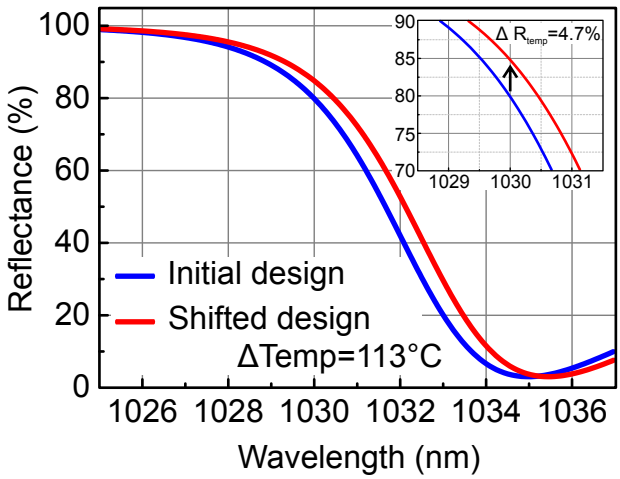

Figure 5.15: Comparison of the initial design at room temperature (blue curve) and the thermally shifted design ($\triangle Temp$ = 113°C, red curve) for NMC F504. The inset shows that the reflectance at 1030 nm increases by 4.7 % due to the temperature rise.

5.4.2 Spectrophotometric measurements

Next, in order to estimate the temperature influence experimentally, the NMCs F502, F503 and F504 coated on FS substrates of 25.4 mm diameter were placed into an oven (for 2–2.5 hours at 100°C, 100°C and 150°C respectively) and were afterwards characterized with the help of the industrial spectrophotometer Perkin Elmer Lambda 950 described in section 3.3 and a portable FLIR E5 camera (with the measurements accuracy of ±2°C or ±2 % of reading). The minimal slit size of 1 nm of the spectrophotometer was chosen, the data interval was set to 0.1 nm, the integration time was 0.48 s; the samples were measured at AOI=0°. Both the reflectance spectra and the absolute temperature of the samples were recorded starting from the maximal temperature (red curves in figure 5.16(a-c)) down to the ambient air temperature (blue curves in figure 5.16(a-c)). Figure 5.16(a-c) experimentally confirms that a temperature rise unavoidably causes a shift of the edge position to longer wavelengths i.e. in the same direction as the optical Kerr effect (see figure 5.1(b)). Essentially, the steeper the edge of the NMC (enhancing the optical Kerr effect), the more susceptible it is to temperature shifts.

The measured data in figure 5.16(d-i) allows one to estimate the dependence of $\triangle R$ on temperature for all the NMCs (violet diamonds for F502, cyan-blue circles for F503 and green circles for F504) at two levels of R_i/T_i (50/50 and 80/20).

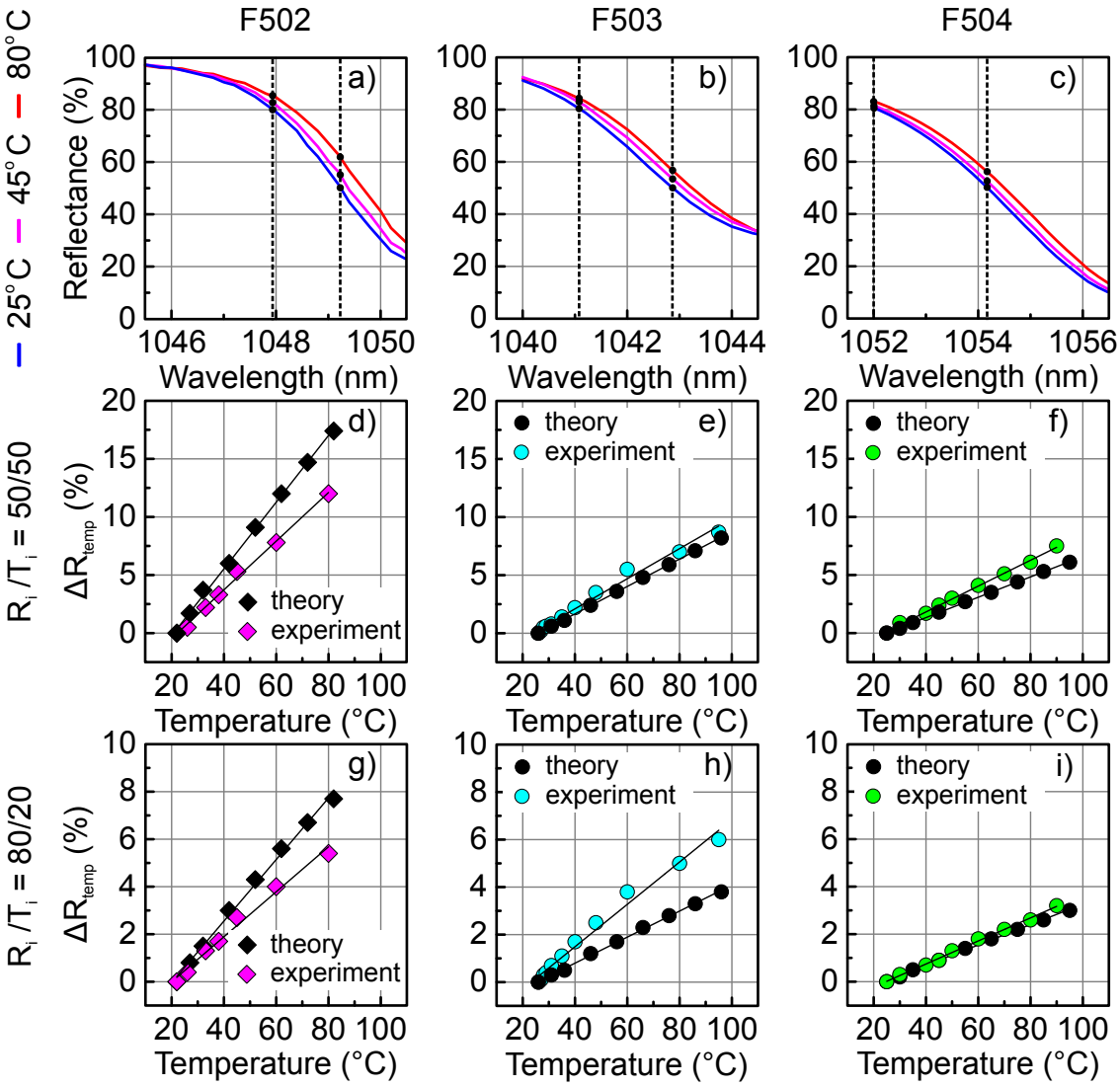

Figure 5.16: Comparison of temperature influence for NMCs F502 (first column), F503 (second column) and F504 (third column). First row presents reflectance spectra of F502 (a), F503 (b) and F504 (c): Spectra measured at AOI=0° shift to longer wavelengths with increasing temperature enumerated by the legend. Black circles positioned at dashed lines set for two cases of R_i/T_i of 50/50 and 80/20 show the increase of reflectance due to the temperature rise. Second row presents reflectance increase due to temperature rise for F502 (d), F503 (e) and F504 (f) for the case of R_i/T_i of 50/50 based on experimental (magenta diamonds, blue or green circles, accordingly) and literature estimations (black diamonds and circles, accordingly). Third row presents reflectance increase due to temperature rise for F502 (g), F503 (h) and F504 (i) for the case of R_i/T_i of 80/20 based on experimental (magenta diamonds, blue or green circles, accordingly) and literature estimations (black diamonds and circles, accordingly). Solid black lines are linear fits of both experimental and literature estimations.

Theoretical appraisals for $\triangle R$ (black diamonds for F502 and black circles for F503 and F504 in figure 5.16(d-i)) based on literature coefficients, were computed by virtue of equation 5.7 for the temperature values measured in the experiment (see subsection 5.3.2) at the same two levels of R_i/T_i. As indicated in figure 5.16(d-i), the theoretical and experimental estimates correlate quite well for NMC F504, while the data for NMC F502 does not quite agree. This discrepancy may be the result of more reliably defined coefficients for Ta_2O_5 thin films compared to those for Nb_2O_5 as more studies have been performed for Ta_2O_5 thin films than for films composed of Nb_2O_5 (e.g. see ref. [197] and references therein). Furthermore, one can notice that the sample F504 is less prone to temperature effects than F502. The theoretical and experimental approximations for F503 for $R_i/T_i = 50/50$ match well (figure 5.16(e)), but, surprisingly, not for $R_i/T_i = 80/20$ (figure 5.16(h)). This observation could be vindicated by the likely different edge slopes of the designed and produced multilayer structures for NMC F503. The results obtained above indicate that while increasing the intensity of the incident laser pulses does result in an increase in the reflectance of the NMCs, it cannot be solely attributed to the optical Kerr effect.

5.4.3 Laser-induced temperature modulation

In order to experimentally exclude the impact of temperature on the NMCs, a chopper wheel was introduced into the setup described above (in front of the lens, figure 5.9). When the laser beam is modulated by a chopper wheel (10% duty cycle), the incident average power drops by approximately a factor of ten (as well as the induced temperature modulations) while the incident peak intensity remains the same. Figure 5.17 displays the surface temperature of NMC F502 measured by the IR camera (FLIR SC 300 Series camera A325) with (chopper on) and without (chopper off) laser beam modulation.

Figure 5.18 shows the decoupling of the temperature-induced and nonlinear behavior for F502 obtained using the setup shown in figure 5.9 with the incorporated chopper wheel. The temperature-induced modulation depths $\triangle R_{temp}$ for F502 (red triangles in figure 5.18) were computed with the help of the experimentally determined linear slope of the dependence of R on $Temp$, mentioned above (figure 5.16(d, g)). Next, these $\triangle R_{temp}$ estimations were subtracted from both the modulation depths measured with the chopper $\triangle R_{ch}$ (blue diamonds in figure 5.18(b, d)) and the total modulation depths measured without the chopper $\triangle R_{tot}$ (violet diamonds in figure 5.18(a, c)). Thus, the nonlinear change in reflectance was

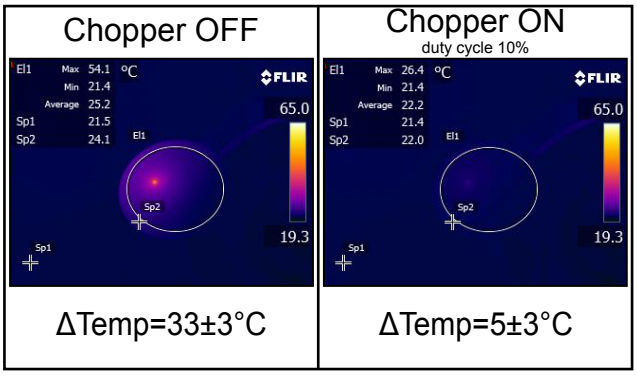

Figure 5.17: An example of an IR camera image for NMC F502 at 47 GW/cm^2, with and without laser beam modulation (chopper).

obtained as follows:

$$\triangle R_{nl} = \triangle R_{tot} - \triangle R_{temp}^{tot} \text{ or } \triangle R_{nl} = \triangle R_{ch} - \triangle R_{temp}^{ch}\,, \tag{5.8}$$

where $\triangle R_{temp}^{ch}$ and $\triangle R_{temp}^{tot}$ are the temperature-induced modulation depths with and without the chopper, respectively. Analogous estimations were performed for the NMCs F503 and F504 and yield similar results (figures 5.19 and 5.20 respectively). The negative values seen in figures 5.18-5.20 can be vindicated by an increased error budget of the powermeter at low intensities.

Finally, the "pure" nonlinear changes estimated in this manner for all the NMCs correspond to the measured values of modulation depths of reflectance in absence of temperature growth within the experimental uncertainty (figures 5.18–5.20). The temperature impact appears to be almost 50% (or even more depending on the value of R_i/T_i) of the observed modulation depths in reflectance and transmittance for the unmodulated laser radiation case (chopper off in figures 5.18–5.20). Basically, the experimentally observed nonlinear pre-damage behavior of the studied elements appears to be an interplay of the temperature-induced and nonlinear effects in these particular NMC realizations. Nevertheless, it is possible to circumvent the temperature influence by introducing an optical modulator. Thus, the modulation depths measured in this way can be regarded as "pure" nonlinear effect estimations. Notice, that the nonlinear effect of about 6% occurs at 50% edge of the filter F504 (figure 5.20). At 80% of the same edge filter, the effect is about 3%. These values might not seem large, however, one can conclude that they are quite significant if one takes into consideration that the nonlinear coefficients of dielectrics are estimated to be on the order of 10^{-15} cm^2/W (as discussed in

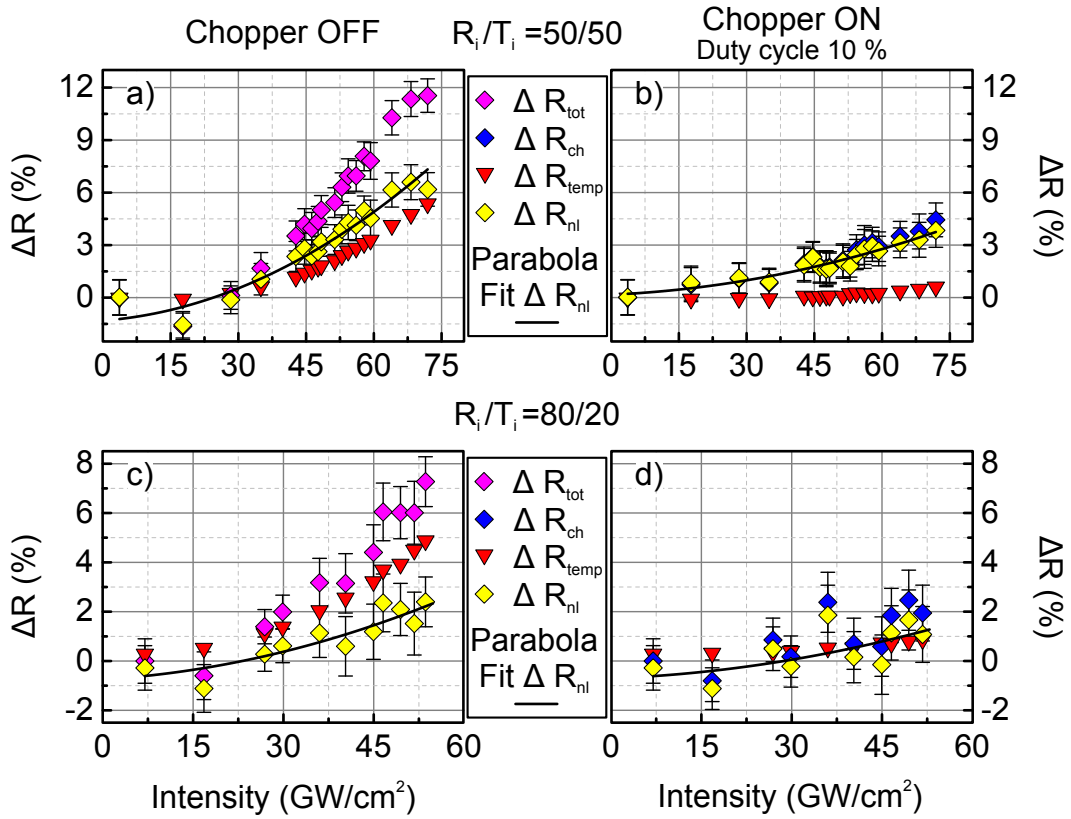

Figure 5.18: Estimation of the "pure" nonlinear effect for NMC F502: Estimated nonlinear $\triangle R_{nl}$ (yellow diamonds) is obtained as a result of subtracting the temperature-induced $\triangle R_{temp}$ (red triangles) from the total measured $\triangle R_{tot}$ (a,c: magenta diamonds) without chopper and $\triangle R_{ch}$ (b,d: blue diamonds) with the chopper for two cases of R_i/T_i of 50/50 (upper panels) and 80/20 (lower panels). The error bars represent standard deviations. Parabola fits (solid black curves) serve as a guide to the eye.

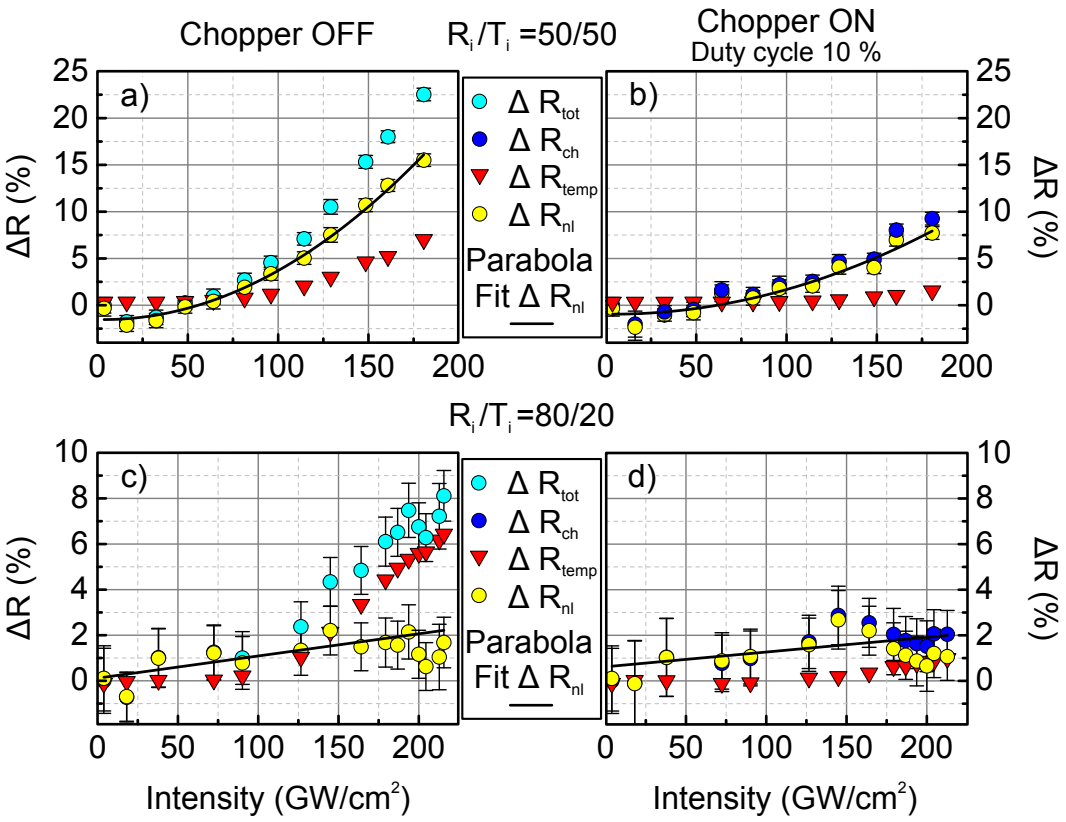

Figure 5.19: Estimation of the "pure" nonlinear effect for NMC F503: Estimated nonlinear $\triangle R_{nl}$ (yellow circles) is obtained as a result of subtracting the temperature-induced $\triangle R_{temp}$ (red triangles) from the total measured $\triangle R_{tot}$ (a,c: cyan-blue circles) without chopper and $\triangle R_{ch}$ (b,d: blue circles) with the chopper for two cases of R_i/T_i of 50/50 (upper panels) and 80/20 (lower panels). The error bars represent standard deviations. Parabola fits (solid black curves) serve as a guide to the eye.

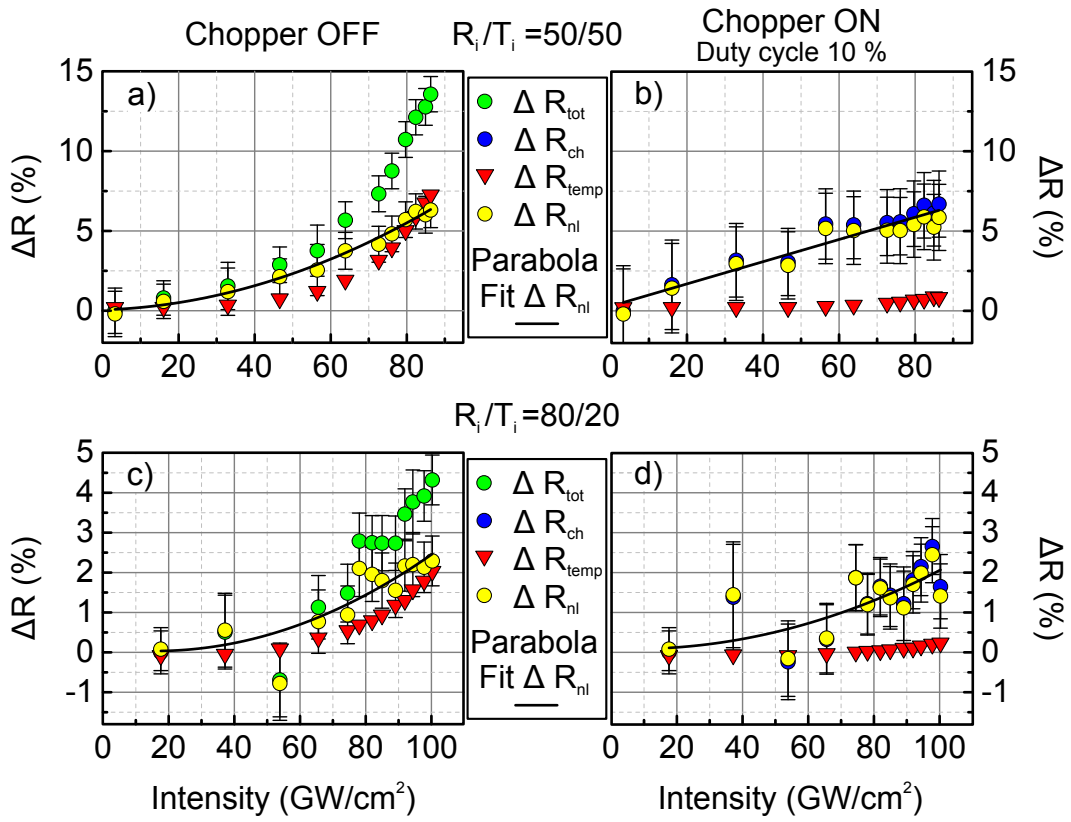

Figure 5.20: Estimation of the "pure" nonlinear effect for NMC F504:Estimated nonlinear $\triangle R_{nl}$ (yellow circles) is obtained as a result of subtracting the temperature-induced $\triangle R_{temp}$ (red triangles) from the total measured $\triangle R_{tot}$ (a,c: green circles) without chopper and $\triangle R_{ch}$ (b,d: blue circles) with the chopper for two cases of R_i/T_i of 50/50 (upper panels) and 80/20 (lower panels). The error bars represent standard deviations. Parabola fits (solid black curves) serve as a guide to the eye.

section 5.1) and a typical change in refractive index is not higher than 0.01.

5.5 Some remarks on self-trapped excitons and incubation effects in the multilayer coatings

As already pointed out, the characterization of optics was conducted in the pre-damage regime. Nevertheless, it is worthwhile to discuss several issues related to the LIDT. Optical damage (also referred to as breakdown) can generally be defined as a permanent change of the optical properties of a material [202]. There are several different physical mechanisms that can cause laser induced damage [62]. The actual damage occurrence depends on the laser parameters such as pulse duration, central wavelength, number of pulses, as well as properties on the sample such as surface quality and bandgap energy. The critical plasma density in the conduction band (CB) is commonly assumed to be the criterion of damage onset [178,179,203,204], for the reason that the free electron density exceeding the critical plasma density makes the material highly absorbing. It is also generally known that a decrease in damage threshold with increasing number of incident pulses S irradiating the same spot (see for example ref. [205]) is caused by the accumulation of defects at fluence values below the single pulse damage fluence F_1 (1-on-1). Typically, the threshold reduces with increasing S before saturating at a particular level F_∞ (infinite number of pulses damage fluence). The mentioned defects can be native defect states as well as laser induced defects (traps). It is then easier for subsequent pulses to excite these defects rather than stimulate electrons from the valence band (VB) to the CB, which results is a decreased damage threshold. The formation of a defect state possessing a large binding energy within picoseconds or faster, depending on the oxide material, has been observed during femtosecond time-resolved pump-probe experiments [187]. These laser induced intermediate levels are most likely related to self-trapped excitons (STEs), which are known to appear in wide-gap dielectric materials [206].

In ideal ionic crystalline bulk materials, electrons and holes can spontaneously form localized states in the bandgap by self-trapping [207]. The electron-hole couple can in turn trap a complementary charge to generate a transient state, the STE. Through atomic displacements, STEs can subsequently develop into

long-lived states, called color centers (also known as F-center, from the original German Farbzentrum) [191, 192, 208–210]. The life times of such color centers can reach minutes, hours, and even months at room temperature [209, 210]. In optical coatings, which are in fact neither entirely crystalline nor amorphous, the picture is much more complicated [211]. First, the thin film deposition techniques result in pre-exisitng (native) defects [190], which can create mid-gap states (shallow traps). Vacancy and interstitial ions are examples of native oxide defects. Shallow traps can manifest themselves as small tails in the transmission spectrum near the bangap observed in oxide films [182]. Second, optical excitation of dielectric materials can produce additional defects similar to what has been studied in pure crystalline bulk materials i.e. it can lead to STEs and subsequently color center formation [191, 192, 209, 210].

The widely reported observation of a decreased damage threshold fluence of dielectric materials for multipulse exposure compared to single-pulse illumination is known to be an incubation (or cumulative) effect [191, 205, 212]. The aforementioned long-lived lattice defects are likely to contribute to material incubation since they can accumulate during multipulse laser excitation. Shallow traps (usually native defects) lie within a one-photon resonance of the CB, whereas deep traps (either native or laser induced) are more than one photon energy below the CB and can be excited by MPA. Shallow traps can be occupied by the CB electrons with high efficiency. Laser induced deep defects in dielectric oxide materials have been concluded to be STEs. Once in the CB, an excited electron can either relax straight to the VB or decay into shallow and deep traps. The number of possibly re-excitable states grows with the number of pulses. The populated traps decrease the LIDT for pulses following the first one in a train.

Usually, the authors [60, 160, 187, 193] try to avoid incubation effects by reducing the repetition rate of the laser or moving the sample after each shot for subpicosecond pulses. However, for the 1-ps pulses used here, most of the change in the damage threshold was recognized to occur between the first and second pulses [194, 195]. Through simulations, the effect of shallow traps has been ratified to be the reason for the latter fact. The effect of shallow traps is the consequence of the weakening contribution of MPA to producing the critical electron density for longer pulse durations (opposed to 50 fs). The intensity at the damage threshold decreases with increasing pulse duration. Subsequently, the importance of linear absorption and avalanche ionization rises. Note, that the effect of shallow traps at longer pulse duration may restrain the effect of deep traps but the former does not exclude the latter; the combined effect of both shallow and deep mid-gap states

always results in a reduced LIDT.

5.6 Time-resolved measurements of the optical Kerr effect in multilayers

Pump-probe measurements, presented in this section, were performed in order to fully verify the Kerr-based nature of the nonlinear response of the NMCs.

5.6.1 Pump-probe experimental setup

The experiments were performed with a degenerative pump-probe setup (figure 5.21) with the aforementioned laser source. The incoming pulse was divided by a beam splitter into pump and probe pulses, and the latter was sent through a variable delay line. The delay line step resolution was 0.01 mm which resulted in 67 fs step in the time domain. The probe beam was attenuated by a factor of 100 with respect to the pump in order to measure only pump-induced reflectance changes. Both pulse replicas were focused on the sample by lenses, and the reflected probe pulse was detected by a photodiode. To examine an approximately uniformly excited region of the sample, the probe was focused onto a spot significantly smaller than the area of the pump (about a factor of 2 smaller). The probe beam remained s-polarized whereas the polarization of the pump was rotated through 90° after propagating through a half-wave plate and a polarization cube, which decreases the possibility of a pronounced so-called "coherence spike" appearing [213]. Many scientific groups have reported on observing a peak around zero delay time (figure 5.22), termed coherence spike (known as coherent interaction or coherent nonlinearity as well) in pump-probe femtosecond measurements [187, 215–217]. The possible presence of the coherence spike needs to be taken into account because the measurement results achieved with the pump-probe method may contain artefacts which can falsely be attributed to the sample response. The photodiode was set to detect s-polarization by employing another half-wave plate and a cube immediately before the detector, hence reducing the influence of unwanted scattered light (figure 5.21). The pump pulse was mechanically modulated by a chopper and the pump-induced reflectance modulation of the probe was detected by a lock-in amplifier in order to increase the signal-to-noise ratio. The setup is capable of a sensitivity up to $\Delta R/R = 10^{-4}$ at 1 kHz [218]. The linear reflectance R_i of the samples was measured separately by a powermeter. The time response measure-

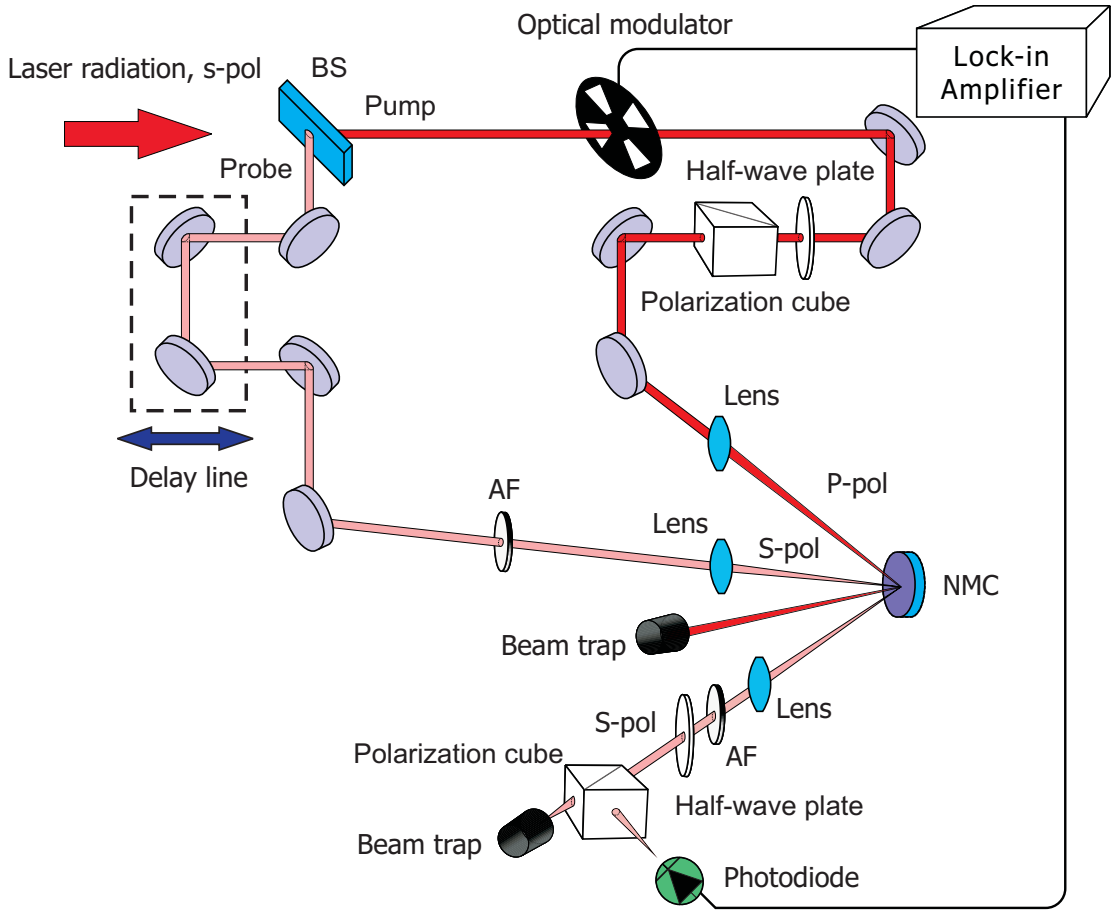

Figure 5.21: Schematic of a degenerate pump-probe setup. BS, beam splitter; AF, attenuating filter. Laser radiation source is a Yb:YAG TD regenerative amplifier: 1030 nm central wavelength, 50 kHz repetition rate, 1 ps pulse duration. The incoming pulse is divided by a beam splitter into pump and probe pulses; the latter is sent through a variable delay line. The probe beam is attenuated (by a factor of 100) with respect to the pump. Both pulse replicas are focused on the sample by lenses, and the reflected probe pulse is detected by a photodiode. To examine an approximately uniformly excited region of the sample, the probe was focused onto a spot significantly smaller than the area of the pump. The probe beam remains s-polarized whereas the polarization of the pump is rotated through 90° one after propagating through a half-wave plate and a polarization cube, which decreases the possibility of a pronounced coherence spike appearing [213]. The photodiode is set to detect s-polarization by employing another half-wave plate and a cube immediately before the detector, hence reducing the influence of unwanted scattered light. The pump pulse is mechanically modulated by a chopper and the pump-induced reflectance modulation of the probe is detected by a lock-in amplifier in order to increase the signal-to-noise ratio.

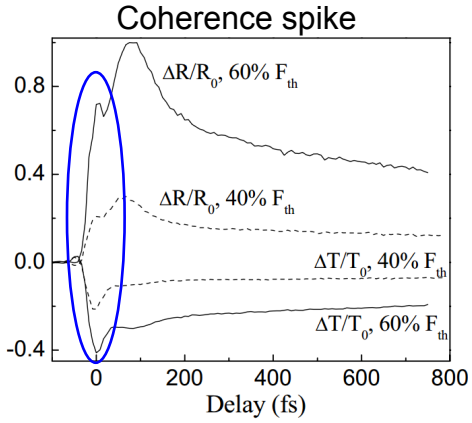

Figure 5.22: Coherence spike observation: The peaks around zero delay time in the measured signals are ususally referred to as coherence spikes (marked by the blue ellipse). Figure adapted from [214].

ments of the NMCs were performed at approximately 85% of the damage threshold intensity.

In order to ensure the reliability of the pump-probe measurements, the time recovery of semiconductor saturable absorber mirror (SESAM, ref. [219]) M4937 [52] was obtained with the help of the assembled pump-probe setup. Figure 5.23 contrasts SESAM M4937 and the NMC F504. The SESAM M4937 demonstrates the two-time-scale response typical for SESAMs [219–221]. It is also evident, that the NMC F504 recoveres much more rapidly.

5.6.2 Pump-probe measurements

Time-resolved recovery curves of the NMCs F502 (Nb_2O_5/SiO_2), F503 (Ta_2O_5/SiO_2) and F504 (Ta_2O_5/SiO_2, GDD $= -5000$ fs^2) for different values of R_i/T_i are presented in figures 5.24–5.26 respectively. Due to the fact that the source pulse duration is 1 ps, any possible coherence spike, typically on the order of 5–20 fs, cannot be resolved. The detected relative changes of R are presented in the normalized view as these values are most probably affected by the presence of the coherence spike, and thus are not of interest. Figures 5.24–5.26 provide evidence that the reflectance change disappears very quickly after the pulse for both initial conditions.

Over the course of the measurements, the recovery of NMC F504 was consistently below the 1 ps sensitivity of the detection system (for the cases R_i/T_i 50/50 and

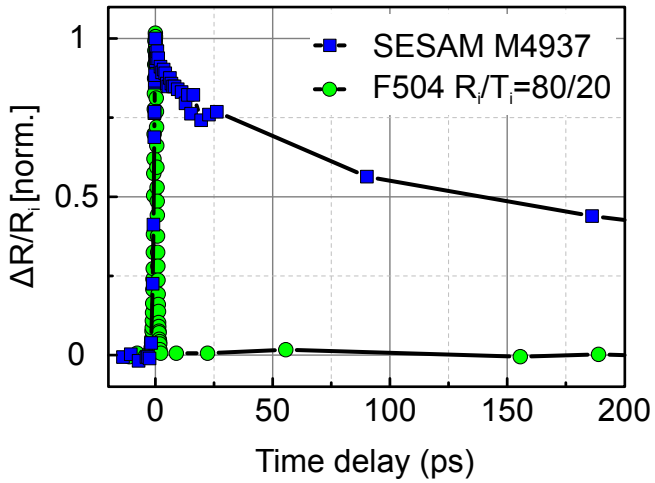

Figure 5.23: Time response of SESAM M4937 (R_i = 98.4 %), hit by a 1-ps pulse at zero time delay, obtained with the described pump-probe setup. The time response of the NMC F504 for R_i/T_i = 80/20 is provided for comparison as well.

80/20). The response time of NMCs F502 and F503, however, contained some features observed after the pump pulse is gone. Figure 5.27 depicts the statistics of the pump-probe measurements for all three NMCs for $R_i/T_i = 90/10$ collected over several months performed at different sites of the sample surfaces. The ACF of the laser source used in the experiments was measured with the help of a commercial autocorrelator (A · P · E pulseCheck 15). The measured ACF was then fitted by the expected Gaussian function with τ_{ac} =1.46 ps, from which the pulse duration τ_p =1 ps can be calculated via $\tau_\mathrm{p} = 0.707 \cdot \tau_{ac}$ (ref. [1], p. 477). The normalized time response of the three NMCs is compared to the Gaussian fitted ACF (solid black curves in the right panels of figure 5.27). The short time behavior in figure 5.27 makes it obvious that the recovery of the NMC F504 entirely follows the 1-ps pulse. Much slower temperature effects, usually occurring within seconds, cannot contribute to response of NMCs on 1 ps time scale. Thus, at least for F504, the "pure" change in reflectance measured previously (figure 5.20) is fully related to the nonlinear time response with an upper limit of 1 ps. For comparison, the nonlinear response of a metallodielectric mirror [176] does not fully recover after a delay of 16 ps.

To date, it is not clear whether the witnessed "tails", which can be seen in the long time behavior in figure 5.27, have physical explanation or not. In case the "tails" can be regarded as artifacts (e. g. due to some electronics issue),

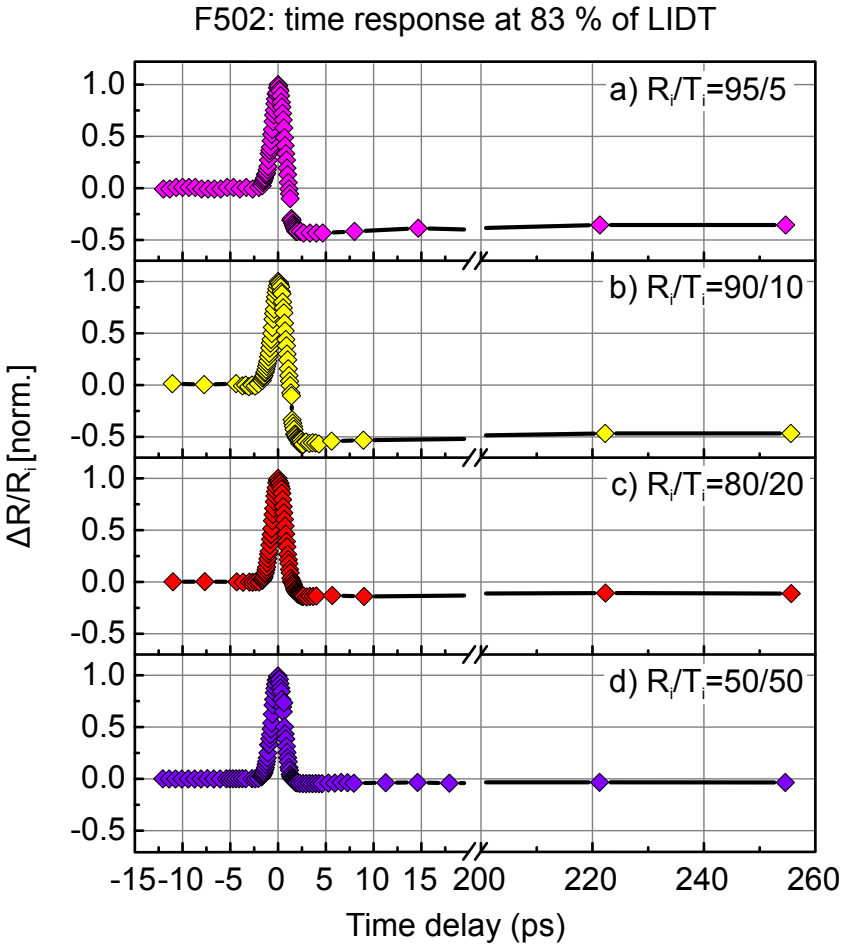

Figure 5.24: Time response of NMC F502 at 83% of LIDT, hit by a 1-ps pulse at zero time delay for the cases of R_i/T_i of 95/5 (a), 90/10 (b), 80/20 (c), 50/50 (d).

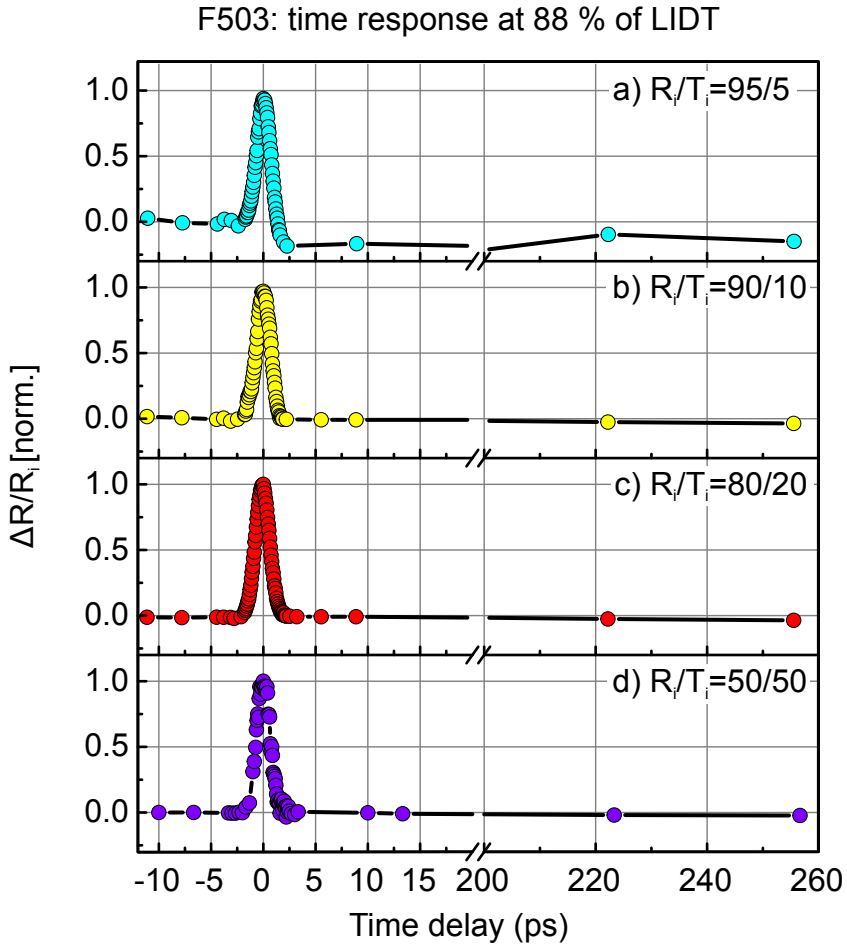

Figure 5.25: Time response of NMC F503 at 88% of LIDT, hit by a 1-ps pulse at zero time delay for the cases of R_i/T_i of 95/5 (a), 90/10 (b), 80/20 (c), 50/50 (d).

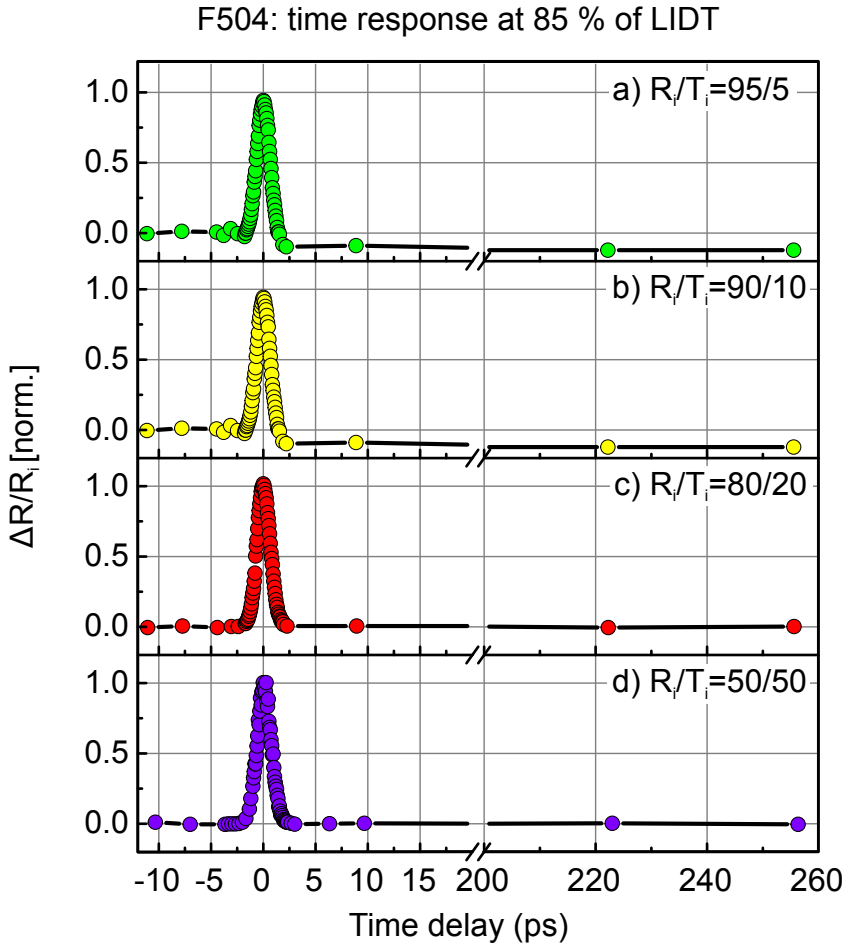

Figure 5.26: Time response of NMC F504 at 85% of LIDT, hit by a 1-ps pulse at zero time delay for the cases of R_i/T_i of 95/5 (a), 90/10 (b), 80/20 (c), 50/50 (d).

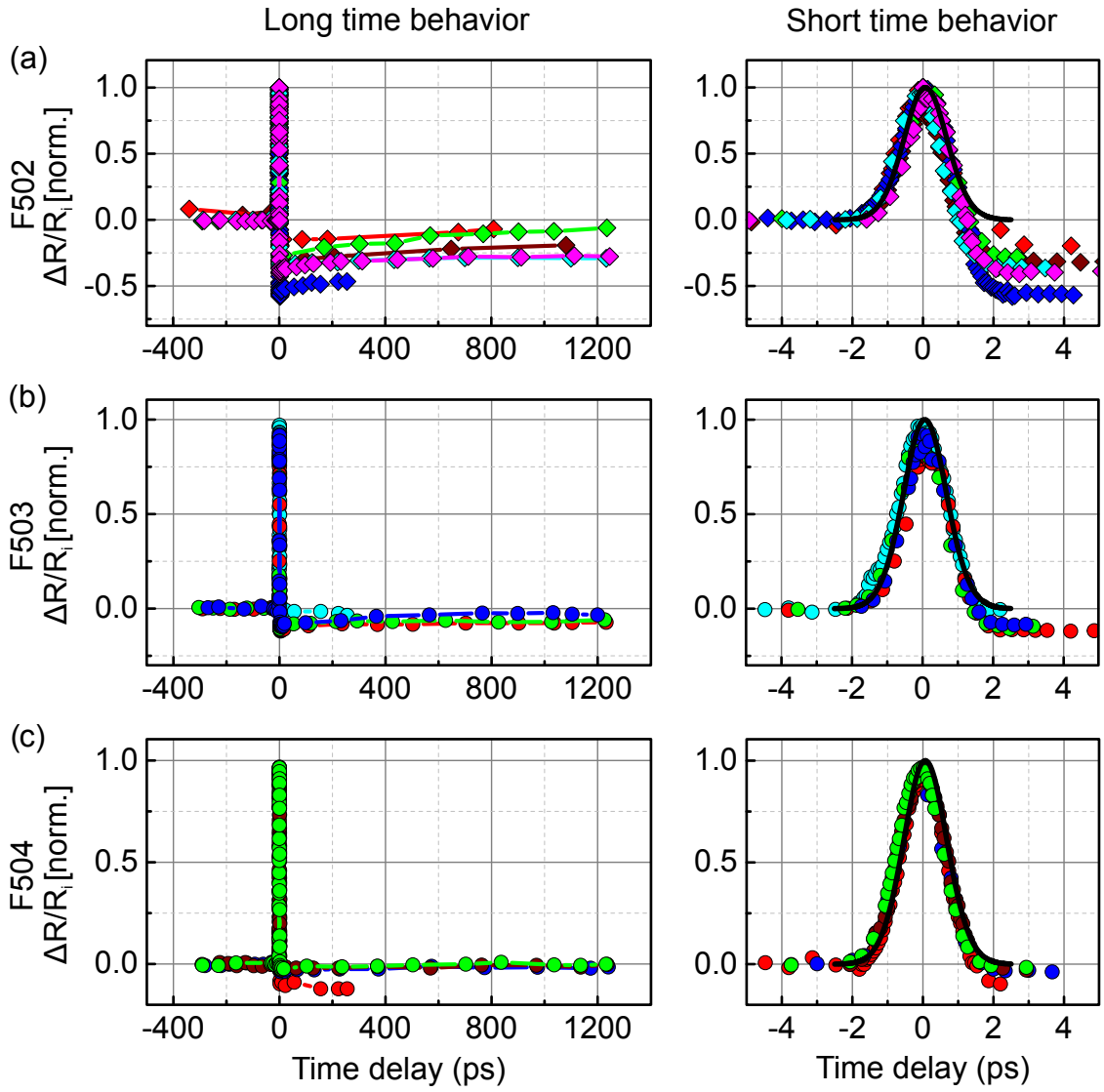

Figure 5.27: Reproducibility of pump-probe measurements for NMCs F502 (a), F503 (b) and F504 (c) where $R_i/T_i = 90/10$. The long time behavior (left panels) is contrasted with short time behavior (right panels). Short time behavior (right panels) of the NMCs is compared to a Gaussian fitted ACF (black solid curve). The presented measurements were performed on different days and at different sites on the NMCs.

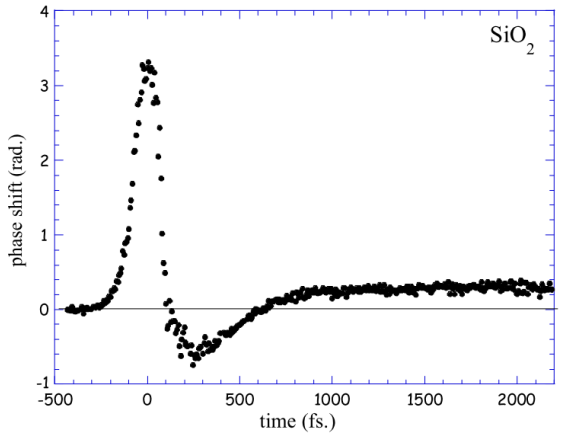

Figure 5.28: Phase shift as a function of time measured in SiO_2. The initial positive phase shift is due to the Kerr effect, then free carriers induce a negative phase shift (plasma effect) and finally electron–hole pairs are trapping deeply in the band gap, leading to a positive phase shift. The intensities are kept well below the threshold. Figure and the caption are adapted from [193].

then the time response of all the studied NMCs could certainly be claimed to be below 1 ps. If the features detected at long delay times have, on the contrary, a physical origin, only NMC F504 demonstrates more or less reproducible rapid recovery. As a remark, the pre-damage nonlinear behavior of oxide dielectric single-layer thin films (including Ta_2O_5 and SiO_2) has been attributed to several effects [193, 214, 222]. Among the latter, MPA processes, the optical Kerr effect and the ultrafast formation of STEs (discussed in section 5.5) on a 1-ps time scale have been stated to be the dominant ones.

More specifically, using either conventional pump-probe or femtosecond pump-probe interferometry technique, a group of researches [192, 193, 223] has investigated the kinetics in both quartz (α-SiO_2) and amorphous silica (a-SiO_2). Mouskeftaras et al. [193] have measured the change of the phase shift in time (figure 5.28), which is basically proportional to n_2, and is somewhat similar to the pump-probe traces presented here (figure 5.27(a,b)). The first positive part has been attributed to the Kerr effect, followed by a negative part (when the pump is gone), proportional to the density of photo-excited electrons. The final positive phase shift has been justified by STE formation. Likewise, it could be that the STEs form in the multilayer structures presented in this work as well, resulting in both the temperature rise (due to MPA via the induced mid-gap states) and the long-time tails in the pump-probe measurements. However, this remains only speculation at this

point, and these undetermined features need to be further investigated.

Overall, in multilayer thin films, nonlinear absorption has been shown to only lead to decreasing reflectance (e.g. ref. [145]), which is not the case in the present study (see section 5.3). The temperature-induced effects were isolated, enabling the observation of the "pure" nonlinear effect (see section 5.4). Recovery of the NMCs limited to 1 ps was shown (figure 5.27). Hence, from a physical point of view, the nonlinear pre-damage performance of the NMCs is dominated by the optical Kerr effect.

Previously reported calculations [147, 150, 152] and experiments with various nonlinear optical materials and devices [145, 146, 170–176] have predominantly been performed for wavelengths equal to or shorter than 800 nm, where MPA processes arise in dielectrics with a high probability. For the present investigation, any MPA processes are considered detrimental. The longer the wavelength, the less the probability of MPA and other intensity-dependent absorption effects, hindering the beneficial optical Kerr effect (for the same E_g). A step towards longer wavelengths and, consequently, to a nonlinear optical response dominated solely by the optical Kerr effect, was undertaken herein. Operating at longer wavelengths such as 1.5 μm or 2 μm is expected to bypass the limitations originating from intensity-dependent absorption.

Chapter 6

Applications of nonlinearities in dielectric multilayer coatings

This chapter introduces the first potential applications of the NMCs, among which are limiters (section 6.1), spatial (section 6.2) or temporal filters (section 6.3), and light modulators (section 6.4). As mode-lockers, the NMC devices, could be used in combination with other mode-locking techniques, for instance with Kerr-lens mode-locking.

6.1 Limiter

Here, one of the possible applications is demonstrated, namely performance of an NMC as a passive, intensity-stabilizing element for laser pulse trains. A plot of average transmitted power versus incident laser peak intensity (figure 6.1) illustrates that the transmitted power P_{tr} practically remains constant in the nonlinear regime (starting from about 100 GW/cm^2) despite the increasing incident intensity. This result shows that NMC F504 exhibits "limiting performance", i.e. limits the transmitted power to a certain value which depends on the value of R_i/T_i. The nearly instantaneous Kerr effect thereby ensures fast stabilization of the transmitted radiation, whereas the temperature effect additionally provides slow stabilization at a time scale of 1 s.

6.2 Spatial filter

One of the potential applications of NMCs is the spatial filtering of optical pulses. Generally, the spatial intensity distribution of pulses produced by laser oscillators and amplifiers can be represented by a Gaussian function. Such beam profiles

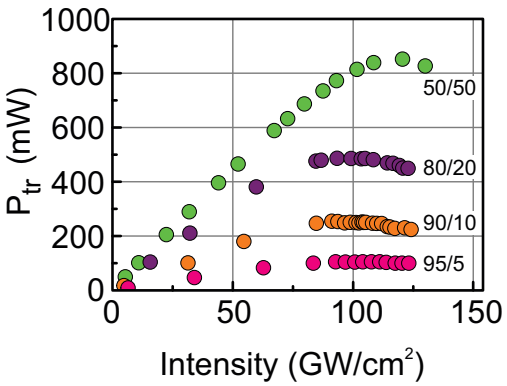

Figure 6.1: Limiting performance of NMC F504: Dependence of transmitted power P_{tr} on the peak intensity for different R_i/T_i values enumerated by the legend.

usually contain additional higher order modes of non-Gaussian shape. The nonlinear spatial filter, based on the propoerty of the NMCs demonstrating higher reflectance for higher intensities, can effectively filter these modes out. Hence, mostly the lower order Gaussian part of the beam will be reflected by the spatial filter. Furthermore, it is sometimes necessary to obtain a nearly flat spatial distribution in order to prevent undesirable self-focusing effects in air and gain media. This can be achieved with the help of a nonlinear π-shaper which is more absorbant at higher intensities (due to 2PA in the dielectric layers), thus flattening the laser beam profile as shown in figure 6.2.

6.3 Temporal filter

The NMCs may possibly lead to the creation of temporal filters, allowing the reduction of noise of the incident laser radiation. Such "noise eaters" would stabilize the laser output and would be incredibly useful for laser applications, where stability plays an important role. Similar to the demonstrated limiting behavior of the NMCs (section 6.1), a certain constant pulse intensity will be transmitted through the nonlinear stabilizer regardless of the incident pulse intensity in the time domain (figure 6.3). Naturally, the fast time response of the NMCs is the necessary condition for the stabilizing performance.

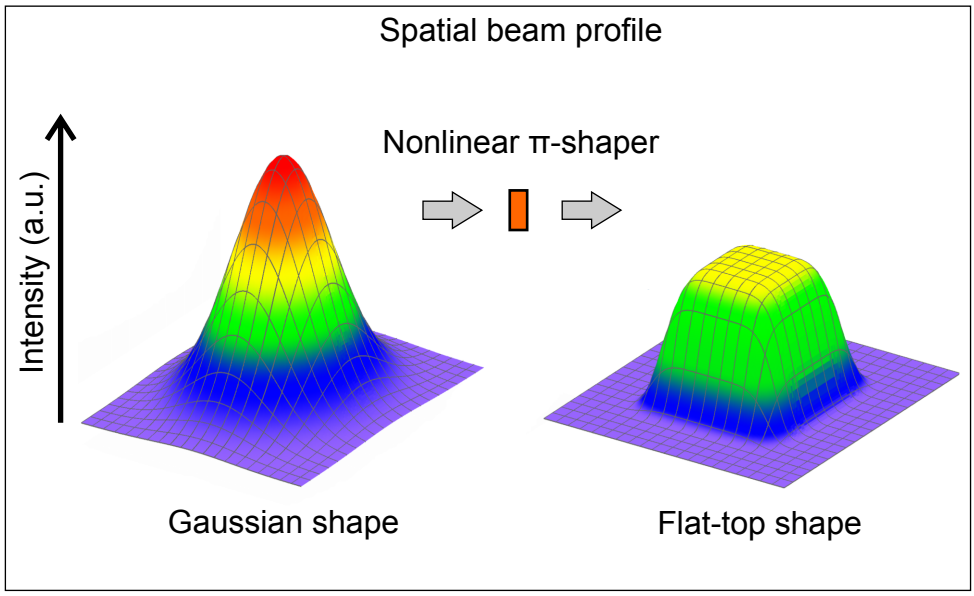

Figure 6.2: Principle of a nonlinear π-shaper: It absorbs stronger at higher intensities (due to the 2PA in dielectric layers), thus flattening the laser beam profile. The original figure was kindly provided by T. Amotchkina.

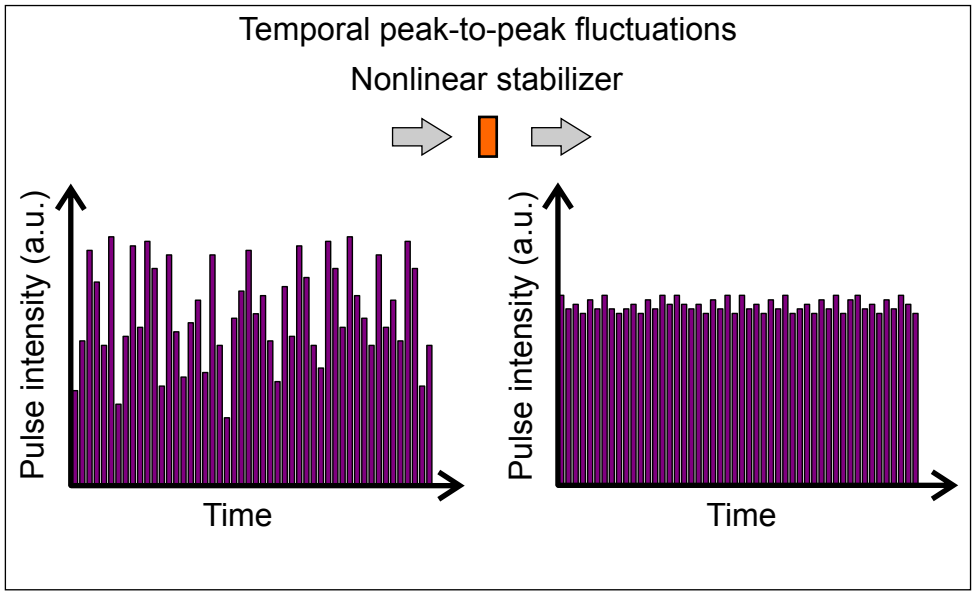

Figure 6.3: Principle of a nonlinear stabilizer: A certain constant pulse intensity is transmitted through the nonlinear stabilizer regardless of the incident pulse intensity in the time domain.

6.4 Mode-locking device: Multilayer Amplitude Modulator

Originally, the idea for creating a light modulator exploiting intensity-dependent refractive indices of a multilayer coating beneficial for mode-locking in particular has emerged. In this case, the NMC would serve as a multilayer amplitude modulator (MAM).

The current design has a rather narrow bandwidth of about 10 nm (see e.g. figure 5.1(b)), which would limit the pulse durations down to 100–200 fs (the upper limit) if the presented NMCs are implemented as mode-locking devices. However, in combination with Yb-doped gain media (Yb:YAG, Yb:KYW, Yb:KGW), whose emission bandwidths are intrinsically narrow (about 9–15 nm), the edge-type structure does not restrict the attainable bandwidth. For the possible mode-locking applications, the change in reflectance on the order of 0.5% (modulation depth currently demonstrated by SESAMs) is sufficient to achieve mode-locking of a laser system. Potentially, the NMC devices could outperform such mode-lockers as SESAMs due to much faster time response and absence of linear absorption.

A typical mode-locked oscillator configuration (figure 6.4) consisting of a laser gain medium, linear or ring resonator, HR mirrors and DMs. The MAM operated in reflection is schematically depicted in figure 6.4(a), whereas figure 6.4(b) illustrates the MAM functioning in transmission. MAM should be positioned inside the cavity in such a fashion that the beam size is small enough to reach the required intensity and thus induce the appropriate reflectance change. For instance, the MAM can be located in the beam focus created by two concave mirrors as shown in figure 6.4(a), where it at the same time serves as an output coupler. A person skilled in the art of cavity design can suggest many other cavity configurations providing the small beam size inside of the cavity. For instance, a small beam size can be achieved closer to one of the end mirrors. In this case, the MAM would be used as an end mirror or positioned closer to the end mirror as exemplified in figure 6.4(b). The MAM could also be used in combination with other mode-locking techniques, e.g. KLM. Multiple MAMs, integrated in the laser cavity, could enhance the SAM effect. Moreover, complimentary MAMs can be inserted in the cavity such that the overall bandwidth (or dispersion curve) provided by two or more MAMs is better than that provided by a single MAM. The laser gain medium can be chosen as a bulk crystal medium, as a slab crystal and as a TD crystal. Dispersion compensation can be provided by a set of DMs (see section 4.1). A mode-locked oscillator can be operated in the regime of either anomalous

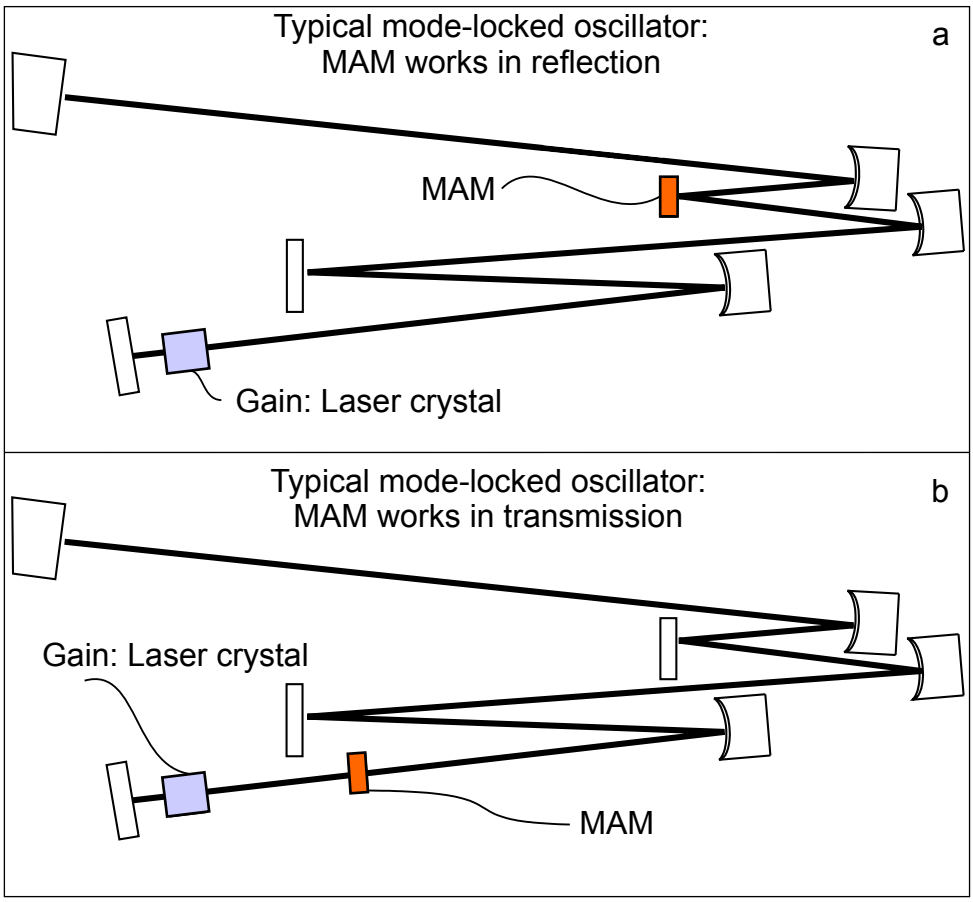

Figure 6.4: Oscillator configuration with the integrated MAM as a mode-locking device: (a) MAM works in reflection; (b) MAM works in transmission. MAM should be positioned inside the cavity in such a fashion that the beam size is small enough to reach the required intensity and thus cause an appropriate reflectance change. MAM is located in the beam focus created by two concave mirrors, where it at the same time serves as an output coupler (a). Alternatively, the small beam size can be achieved closer to one of the end mirrors, where MAM is positioned (b).

(negative) or normal (positive) dispersion.

However, the MAM application has not, up to now, been realized. The temperature effects caused by nonlinear absorption (discussed in section 5.4) are probably one of the most considerable obstacles for achieving mode-locking. One of the possible consequences is that the temperature could change the ROC of mirrors, thus preventing the locking of the phases. More details about the undertaken attempts to achieve mode-locking can be found elsewhere [144]. Nevertheless, the application of an NMC as a mode-locking device, as a multilayer amplitude modulator (MAM) remains one of the most exciting and promising potential applications.

Chapter 7

Summary and outlook

This work has demonstrated the high capacity of coating technology to provide solutions to pushing the boundaries of ultrafast oscillator performance. The feasibility of the coating technology to implement not-hitherto-accessible levels of negative dispersion holds promise for developing laser oscillators with ever shorter pulses possessing ever higher energy, peak and average power values. A single highly-dispersive mirror (HDM) with a group delay dispersion reaching the value of –10 000 fs^2 in the wavelength range 1025–1035 nm has been presented here. This HDM was successfully employed in a mode-locked Yb:YAG thin-disk oscillator, resulting in 320-fs pulses with an average power of about 4 W; and lead to no degradation in the oscillator behavior in comparison to an HDM with $-3000\,fs^2$. In the course of time, HDMs providing unprecedented levels of dispersion may be integrated in high average power regenerative amplifiers. Advancing HDMs to ever higher negative dispersion benefits the development of compact, user-friendly, high-power and high-repetition rate femtosecond oscillators and may, in prospect, simplify pulse stretching-compression schemes in chirped-pulse amplifier systems. Further research directed at HDMs deposited on suitable substrates concurrently demonstrating high dispersion values for a broad wavelength range, low losses, high damage threshold and negligible thermal effects will promote the development of ultrafast oscillators.

At the same time, the coating technology can become a source of nonlinearity and spawn a novel class of laser elements. Dielectric optical coatings whose operating principle is based on the nonlinear optical Kerr effect are near at hand and may become a key element in enhancing the capabilities of ultrafast oscillators. Nonlinear multilayer coatings (NMCs) for the near-infrared spectral range have been designed, manufactured and intensely characterized in the frame of this work. The observed nonlinear behavior of the NMCs has been found to be the result of two separate manifestations: a quasi-instantaneous nonlinear response

driven by the optical Kerr effect, and temperature-induced effects arising through thermal expansion and the thermo-optic effect. The detrimental temperature influence has been studied independently. The modulation depth in reflectance of the NMCs due to the optical Kerr effect has been shown to be as high as 6 %, which is fairly significant considering the small Kerr coefficients of the composing dielectric materials. Pump-probe measurements have shown that the nonlinearity of the NMCs has a rapid recovery time shorter than the laser envelope width of 1 ps.

Investigating the origin of absorption in the presented NMCs as well as the unexplained long time dynamics should enable the creation of elements exhibiting a solely Kerr-based nonlinear response. It may also be interesting to create NMCs for longer wavelengths, around 2 μm, where the probability of multiphoton absorption and other intensity-dependent absorption effects is lower (given the bandgap energy remains the same). There, a nonlinear response based entirely on the quasi-instantaneous change of the refractive index is expected. Dielectric NMC elements, which can be fabricated using standard coating techniques available in many facilities around the world, could be a viable alternative for conventional nonlinear materials in laser applications. NMCs can potentially be integrated in laser oscillators as intensity-limiting, spatial or temporal filters. With further optimization, NMCs may serve as multilayer amplitude modulators for initiating or assisting laser mode-locking. In a greater outlook, the NMCs may betoken the advent of a novel all-dielectric mode-locking technique.

Bibliography

[1] J.-C. Diels and W. Rudolph, *Ultrashort laser pulse phenomena.* Academic press, 2006.

[2] J. R. Lawrence, *Advances in laser materials processing: Technology, research and application.* Elsevier, 2010.

[3] R. A. Delgado-Ruiz, J. L. Calvo-Guirado, P. Moreno, J. Guardia, G. Gomez-Moreno, J. E. Mate-Sanchez, P. Ramirez-Fernandez, and F. Chiva, "Femtosecond laser microstructuring of zirconia dental implants," *Journal of Biomedical Materials Research Part B-applied Biomaterials*, vol. 96B, pp. 91–100, 2011.

[4] M. Bass, *Laser materials processing.* Elsevier, 2012, vol. 3.

[5] M. Drescher, M. Hentschel, R. Kienberger, M. Uiberacker, V. Yakovlev, A. Scrinzi, T. Westerwalbesloh, U. Kleineberg, U. Heinzmann, and F. Krausz, "Time-resolved atomic inner-shell spectroscopy," *Nature*, vol. 419, pp. 803–807, 2002.

[6] D. V. Palanker, M. S. Blumenkranz, and M. F. Marmor, "Fifty years of ophthalmic laser therapy," *Archives of Ophthalmology*, vol. 129, pp. 1613–1619, 2011.

[7] K. K. Jain, "Current status of laser applications in neurosurgery," *IEEE Journal of Quantum Electronics*, vol. 20, pp. 1401–1406, 1984.

[8] R. W. Ryan, R. F. Spetzler, and M. C. Preul, "Aura of technology and the cutting edge: a history of lasers in neurosurgery," *Neurosurgical Focus*, vol. 27, p. E6, 2009.

[9] A. H. Zewail, "Laser femtochemistry," *Science*, vol. 242, pp. 1645–1653, 1988.

[10] A. H. Zewail, "Femtochemistry: Atomic-scale dynamics of the chemical bond," *Journal of Physical Chemistry A*, vol. 104, pp. 5660–5694, 2000.

[11] R. Holzwarth, T. Udem, T. W. Hänsch, J. C. Knight, W. J. Wadsworth, and P. S. J. Russell, "Optical frequency synthesizer for precision spectroscopy," *Physical Review Letters*, vol. 85, pp. 2264–2267, 2000.

[12] T. Udem, R. Holzwarth, and T. W. Hänsch, "Optical frequency metrology," *Nature*, vol. 416, pp. 233–237, 2002.

[13] C. Gohle, T. Udem, M. Herrmann, J. Rauschenberger, R. Holzwarth, H. A. Schuessler, F. Krausz, and T. W. Hänsch, "A frequency comb in the extreme ultraviolet," *Nature*, vol. 436, pp. 234–237, 2005.

[14] A. Cingoez, D. C. Yost, T. K. Allison, A. Ruehl, M. E. Fermann, I. Hartl, and J. Ye, "Direct frequency comb spectroscopy in the extreme ultraviolet," *Nature*, vol. 482, pp. 68–71, 2012.

[15] M. Hentschel, R. Kienberger, C. Spielmann, G. A. Reider, N. Milosevic, T. Brabec, P. Corkum, U. Heinzmann, M. Drescher, and F. Krausz, "Attosecond metrology," *Nature*, vol. 414, pp. 509–513, 2001.

[16] F. Krausz, "From femtochemistry to attophysics," *Physics World*, vol. 14, pp. 41–46, 2001.

[17] E. Goulielmakis, M. Schultze, M. Hofstetter, V. S. Yakovlev, J. Gagnon, M. Uiberacker, A. L. Aquila, E. M. Gullikson, D. T. Attwood, R. Kienberger, F. Krausz, and U. Kleineberg, "Single-cycle nonlinear optics," *Science*, vol. 320, pp. 1614–1617, 2008.

[18] F. Krausz and M. I. Stockman, "Attosecond metrology: from electron capture to future signal processing," *Nature Photonics*, vol. 8, pp. 205–213, 2014.

[19] T. Brabec and F. Krausz, "Intense few-cycle laser fields: Frontiers of nonlinear optics," *Reviews of Modern Physics*, vol. 72, pp. 545–591, 2000.

[20] U. Keller, "Recent developments in compact ultrafast lasers," *Nature*, vol. 424, pp. 831–838, 2003.

[21] F. Krausz and M. Ivanov, "Attosecond physics," *Reviews of Modern Physics*, vol. 81, pp. 163–234, 2009.

[22] E. Goulielmakis and F. Krausz, "Making optical waves, tracing electrons in real-time: The onset of the attosecond realm," *Progress In Electromagnetics Research-pier*, vol. 147, pp. 127–140, 2014.

[23] P. B. Corkum, N. H. Burnett, and F. Brunel, "Above-threshold ionization in the long-wavelength limit," *Physical Review Letters*, vol. 62, pp. 1259–1262, 1989.

[24] P. B. Corkum, "Plasma perspective on strong-field multiphoton ionization," *Physical Review Letters*, vol. 71, pp. 1994–1997, 1993.

[25] C. Spielmann, C. Kan, N. H. Burnett, T. Brabec, M. Geissler, A. Scrinzi, M. Schnurer, and F. Krausz, "Near-keV coherent X-ray generation with sub-10-fs lasers," *IEEE Journal of Selected Topics In Quantum Electronics*, vol. 4, pp. 249–265, 1998.

[26] M. DiDomenico, "Small-signal analysis of internal (coupling-type) modulation of lasers," *Journal of Applied Physics*, vol. 35, pp. 2870–2876, 1964.

[27] A. Yariv, "Internal modulation in multimode laser oscillators," *Journal of Applied Physics*, vol. 36, pp. 388–391, 1965.

[28] D. E. Spence, P. N. Kean, and W. Sibbett, "60-fsec pulse generation from a self-mode-locked Ti-sapphire laser," *Optics Letters*, vol. 16, pp. 42–44, 1991.

[29] A. Poppe, M. Lenzner, F. Krausz, and C. Spielmann, "A sub-10 fs, 2.5 MW Ti:sapphire oscillator," in *paper presented at the 1999 conference on Ultrafast Optics, Zurich, Switzerland*, 1999.

[30] R. Szipocs, K. Ferencz, C. Spielmann, and F. Krausz, "Chirped multilayer coatings for broad-band dispersion control in femtosecond lasers," *Optics Letters*, vol. 19, pp. 201–203, 1994.

[31] A. Stingl, M. Lenzner, C. Spielmann, F. Krausz, and R. Szipocs, "Sub-10-fs mirror-dispersion-controlled Ti-sapphire laser," *Optics Letters*, vol. 20, pp. 602–604, 1995.

[32] A. Kasper and K. J. Witte, "10-fs pulse generation from a unidirectional kerr-lens mode-locked ti:sapphire ring laser," *Optics Letters*, vol. 21, pp. 360–362, 1996.

[33] O. Pronin, M. Seidel, F. Luecking, J. Brons, E. Fedulova, M. Trubetskov, V. Pervak, A. Apolonski, T. Udem, and F. Krausz, "High-power multi-megahertz source of waveform-stabilized few-cycle light," *Nature Communications*, vol. 6, p. 6998, 2015.

[34] A. Wirth, M. T. Hassan, I. Grguras, J. Gagnon, A. Moulet, T. T. Luu, S. Pabst, R. Santra, Z. A. Alahmed, A. M. Azzeer, V. S. Yakovlev, V. Pervak, F. Krausz, and E. Goulielmakis, "Synthesized light transients," *Science*, vol. 334, pp. 195–200, 2011.

[35] C. Manzoni, O. D. Muecke, G. Cirmi, S. Fang, J. Moses, S.-W. Huang, K.-H. Hong, G. Cerullo, and F. X. Kaertner, "Coherent pulse synthesis: towards sub-cycle optical waveforms," *Laser & Photonics Reviews*, vol. 9, pp. 129–171, 2015.

[36] M. T. Hassan, A. Wirth, I. Grguras, A. Moulet, T. T. Luu, J. Gagnon, V. Pervak, and E. Goulielmakis, "Attosecond photonics: Synthesis and control of light transients," *Review of Scientific Instruments*, vol. 83, p. 111301, 2012.

[37] Z. Cheng, G. Tempea, T. Brabec, K. Ferencz, C. Spielmann, and F. Krausz, *Ultrafast Phenomena XI: Proceedings of the 11th International Conference, Garmisch-Partenkirchen, Germany, July 12–17, 1998*. Berlin, Heidelberg: Springer Berlin Heidelberg, 1998, ch. Generation of Intense Diffraction-Limited White Light and 4-fs Pulses, pp. 8–10.

[38] A. S. Morlens, P. Balcou, P. Zeitoun, C. Valentin, V. Laude, and S. Kazamias, "Compression of attosecond harmonic pulses by extreme-ultraviolet chirped mirrors," *Optics Letters*, vol. 30, pp. 1554–1556, 2005.

[39] A. Wonisch, U. Neuhaeusler, N. M. Kabachnik, T. Uphues, M. Uiberacker, V. Yakovlev, F. Krausz, M. Drescher, U. Kleineberg, and U. Heinzmann, "Design, fabrication, and analysis of chirped multilayer mirrors for reflection of extreme-ultraviolet attosecond pulses," *Applied Optics*, vol. 45, pp. 4147–4156, 2006.

[40] M. Suman, G. Monaco, M. G. Pelizzo, D. L. Windt, and P. Nicolosi, "Realization and characterization of an xuv multilayer coating for attosecond pulses," *Optics Express*, vol. 17, pp. 7922–7932, 2009.

[41] M. Hofstetter, "Multilayer mirrors for attosecond pulse shaping between 30 and 200 eV," Ph.D. dissertation, Ludwig-Maximilian University München, 2011.

[42] I. P. Christov, M. M. Murnane, and H. C. Kapteyn, "High-harmonic generation of attosecond pulses in the "single-cycle" regime," *Physical Review Letters*, vol. 78, pp. 1251–1254, 1997.

[43] R. Kienberger, E. Goulielmakis, M. Uiberacker, A. Baltuska, V. Yakovlev, F. Bammer, A. Scrinzi, T. Westerwalbesloh, U. Kleineberg, U. Heinzmann, M. Drescher, and F. Krausz, "Atomic transient recorder," *Nature*, vol. 427, pp. 817–821, 2004.

[44] E. Goulielmakis, M. Uiberacker, R. Kienberger, A. Baltuska, V. Yakovlev, A. Scrinzi, T. Westerwalbesloh, U. Kleineberg, U. Heinzmann, M. Drescher, and F. Krausz, "Direct measurement of light waves," *Science*, vol. 305, pp. 1267–1269, 2004.

[45] F. Habel, W. Schneider, and V. Pervak, "Broadband thin-film polarizer for 12 fs applications," *Optics Express*, vol. 23, pp. 21 624–21 628, 2015.

[46] F. Habel, V. Shirvanyan, M. Trubetskov, C. Burger, A. Sommer, M. F. Kling, M. Schultze, and V. Pervak, "Octave spanning wedge dispersive mirrors with low dispersion oscillations," *Opt. Express*, vol. 24, pp. 9218–9223, 2016.

[47] H. Fattahi, H. G. Barros, M. Gorjan, T. Nubbemeyer, B. Alsaif, C. Y. Teisset, M. Schultze, S. Prinz, M. Haefner, M. Ueffing, A. Alismail, L. Vamos, A. Schwarz, O. Pronin, J. Brons, X. T. Geng, G. Arisholm, M. Ciappina, V. S. Yakovlev, D.-E. Kim, A. M. Azzeer, N. Karpowicz, D. Sutter, Z. Major, T. Metzger, and F. Krausz, "Third-generation femtosecond technology," *Optica*, vol. 1, pp. 45–63, 2014.

[48] A. Dubietis, G. Jonusauskas, and A. Piskarskas, "Powerful femtosecond pulse generation by chirped and stretched pulse parametric amplification in BBO crystal," *Optics Communications*, vol. 88, pp. 437–440, 1992.

[49] F. Krausz, M. E. Fermann, T. Brabec, P. F. Curley, M. Hofer, M. H. Ober, C. Spielmann, E. Wintner, and A. J. Schmidt, "Femtosecond solid-state lasers," *IEEE Journal of Quantum Electronics*, vol. 28, pp. 2097–2122, 1992.

[50] R. Ell, U. Morgner, F. X. Kärtner, J. G. Fujimoto, E. P. Ippen, V. Scheuer, G. Angelow, T. Tschudi, M. J. Lederer, A. Boiko, and B. Luther-Davies, "Generation of 5-fs pulses and octave-spanning spectra directly from a Ti:sapphire laser," *Optics Letters*, vol. 26, pp. 373–375, 2001.

[51] A. Giesen, H. Huegel, A. Voss, K. Wittig, U. Brauch, and H. Opower, "Scalable concept for diode-pumped high-power solid-state lasers," *Applied Physics B-lasers and Optics*, vol. 58, pp. 365–372, 1994.

[52] O. Pronin, "Towards a compact thin-disk-based femtosecond XUV source," Ph.D. dissertation, Ludwig-Maximilians-University of Munich, 2012.

[53] T. Südmeyer, C. Kränkel, C. R. E. Baer, O. H. Heckl, C. J. Saraceno, M. Golling, R. Peters, K. Petermann, G. Huber, and U. Keller, "High-power ultrafast thin disk laser oscillators and their potential for sub-100-femtosecond pulse generation," *Applied Physics B-lasers and Optics*, vol. 97, pp. 281–295, 2009.

[54] J. Brons, V. Pervak, E. Fedulova, D. Bauer, D. Sutter, V. Kalashnikov, A. Apolonskiy, O. Pronin, and F. Krausz, "Energy scaling of Kerr-lens mode-locked thin-disk oscillators," *Optics Letters*, vol. 39, pp. 6442–6445, 2014.

[55] M. A. Duguay and J. W. Hansen, "An ultrafast light gate," *Applied Physics Letters*, vol. 15, pp. 192–194, 1969.

[56] H. A. Macleod, *Thin-Film Optical Filters, Fourth Edition.* CRC Press Taylor & Francis Group, 2010, ch. 11, Production Methods and Thin-Film Materials.

[57] P. J. Kelly and R. D. Arnell, "Magnetron sputtering: a review of recent developments and applications," *Vacuum*, vol. 56, pp. 159–172, 2000.

[58] V. Pervak, A. V. Tikhonravov, M. K. Trubetskov, S. Naumov, F. Krausz, and A. Apolonski, "1.5-octave chirped mirror for pulse compression down to sub-3 fs," *Applied Physics B-lasers and Optics*, vol. 87, pp. 5–12, 2007.

[59] V. Pervak, A. V. Tikhonravov, M. K. Trubetskov, J. Pistner, F. Krausz, and A. Apolonski, "Band filters: two-material technology versus rugate," *Applied Optics*, vol. 46, pp. 1190–1193, 2007.

[60] D. N. Nguyen, L. A. Emmert, D. Patel, C. S. Menoni, and W. Rudolph, "Transient phenomena in the dielectric breakdown of HfO_2 optical films probed by ultrafast laser pulse pairs," *Applied Physics Letters*, vol. 97, p. 191909, 2010.

[61] S. A. Akhmanov and S. Y. Nikitin, *Physical Optics*. Clarendon Press, Oxford, 1997.

[62] R. W. Boyd, *Nonlinear optics, third edition*. Academic Press, 2007.

[63] F. Krausz. Lectures, photonics I. http://www.atto.physik.uni-muenchen.de/teaching/index.html.

[64] H. A. Haus, *Compact Sources of Ultrashort Pulses*. Cambridge University Press, 2006, ch. Short pulse generation, pp. 1–56.

[65] R. Paschotta. Wiley-VCH, 2008, ch. article on 'solitons' in the Encyclopedia of Laser Physics and Technology, 1. edition.

[66] P. L. Kelley, "Self-focusing of optical beams," *Physical Review Letters*, vol. 15, pp. 1005–1008, 1965.

[67] R. H. Stolen and C. Lin, "Self-phase-modulation in silica optical fibers," *Physical Review A*, vol. 17, pp. 1448–1453, 1978.

[68] A. Weiner, *Ultrafast optics*. John Wiley & Sons, Inc., 2011.

[69] J. H. Marburger, "Self-focusing: Theory," *Prog. Qant. Electr.*, vol. 4, pp. 35–110, 1975.

[70] T. Deutsch, "Mode-locking effects in an internally modulated ruby laser," *Applied Physics Letters*, vol. 7, pp. 80–82, 1965.

[71] M. DiDomenico, J. E. Geusic, H. M. Marcos, and R. G. Smith, "Generation of ultrashort optical pulses by mode locking YAIG:Nd laser," *Applied Physics Letters*, vol. 8, pp. 180–183, 1966.

[72] A. F. Gibson, M. F. Kimmitt, and B. Norris, "Generation of bandwidth-limited pulses from a tea CO_2-laser using para type germanium," *Applied Physics Letters*, vol. 24, pp. 306–307, 1974.

[73] M. N. Islam, E. R. Sunderman, C. E. Soccolich, I. Barjoseph, N. Sauer, and T. Y. Chang, "Color center lasers passively mode-locked by quantum wells," *IEEE Journal of Quantum Electronics*, vol. 25, pp. 2454–2463, 1989.

[74] H. W. Mocker and R. J. Collins, "Mode competition and self-locking effects in Q-switched ruby laser," *Applied Physics Letters*, vol. 7, pp. 270–273, 1965.

[75] A. J. DeMaria, D. A. Stetser, and H. Heynau, "Self mode-locking of lasers with saturable absorbers," *Applied Physics Letters*, vol. 8, pp. 174–176, 1966.

[76] M. Piche, "Beam reshaping and self-mode-locking in nonlinear laser resonators," *Optics Communications*, vol. 86, pp. 156–160, 1991.

[77] P. W. Baumeister, "Design of multilayer filters by successive approximations," *Journal of the Optical Society of America*, vol. 48, pp. 955–958, 1958.

[78] E. Delano and R. J. Pegis, "II methods of synthesis for dielectric multilayer filters," *Progress in Optics, North-Holland, Amsterdam*, vol. 7, pp. 67–137, 1969.

[79] P. W. Baumeister, *Optical Coating Technology.* SPIE Press Monograph Vol. PM137, 2004.

[80] A. Thelen, *Design of optical interference coatings.* New York [etc.] : McGraw-Hill, 1989.

[81] S. F. Furman and A. V. Tikhonravov, *Basics of Optics of Multilayer Systems.* Editions Frontieres, 1992.

[82] L. Sossi, *On the theory of the synthesis of multilayer dielectric light filters*, 1977.

[83] P. G. Verly, J. A. Dobrowolski, W. J. Wild, and R. L. Burton, "Synthesis of high rejection filters with the fourier-transform method," *Applied Optics*, vol. 28, pp. 2864–2875, 1989.

[84] P. G. Verly, J. A. Dobrowolski, and R. R. Willey, "Fourier-transform method for the design of wide-band antireflection coatings," *Applied Optics*, vol. 31, pp. 3836–3846, 1992.

[85] A. V. Tikhonravov, "Synthesis of optical coatings using optimality conditions (in Russian)," *Vestn. Mosk. Univ. Fiz. Astronomiya*, vol. 23, pp. 91–93, 1982.

[86] A. V. Tikhonravov, M. K. Trubetskov, and G. W. DeBell, "Application of the needle optimization technique to the design of optical coatings," *Applied Optics*, vol. 35, pp. 5493–5508, 1996.

[87] A. V. Tikhonravov, M. K. Trubetskov, and G. W. DeBell, "Optical coating design approaches based on the needle optimization technique," *Applied Optics*, vol. 46, pp. 704–710, 2007.

[88] A. V. Tikhonravov and M. K. Trubetskov, "Modern design tools and a new paradigm in optical coating design," *Applied Optics*, vol. 51, pp. 7319–7332, 2012.

[89] H. A. Macleod, *Thin-Film Optical Filters, Fourth Edition.* CRC Press Taylor & Francis Group, 2010, ch. 2, Basic Theory.

[90] F. Abeles, "Recherches sur la propagation des ondes electromagnetiques sinusoidales dans les milieux stratifies. application aux couches minces. (in French)," Ph.D. dissertation, Paris: Masson, 1950.

[91] A. V. Tikhonravov, "Some theoretical aspects of thin-film optics and their applications," *Applied Optics*, vol. 32, pp. 5417–5426, 1993.

[92] A. V. Tikhonravov, *Optical interference coatings.* Springer, 2013, ch. Design of Optical Coatings, pp. 81–104.

[93] A. V. Tikhonravov and M. K. Trubetskov, "Optilayer software," http://www.optilayer.com.

[94] O. Stenzel, S. Wilbrandt, S. Yulin, N. Kaiser, M. Held, A. Tünnermann, J. Biskupek, and U. Kaiser, "Plasma ion assisted deposition of hafnium dioxide using argon and xenon as process gases," *Optical Materials Express*, vol. 1, pp. 278–292, 2011.

[95] T. Amotchkina, M. Trubetskov, A. Tikhonravov, I. B. Angelov, and V. Pervak, "Reliable optical characterization of e-beam evaporated TiO_2 films deposited at different substrate temperatures," *Applied Optics*, vol. 53, pp. A8–A15, 2014.

[96] D. T. Wei, H. R. Kaufman, and C.-C. Lee, *Ion beam sputtering Thin Films for Optical Systems.* New York: Marcel Dekker, 1995, pp. 133–201.

[97] R. Lalezari, G. Rempe, R. J. Thompson, and H. J. Kimble, *Measurement of ultralow losses in dielectric mirrors.* Topical Meeting on Optical Interference Coatings (Tucson, AZ) (Washington: Optical Society of America), 1992, pp. 331–333.

[98] J. M. Mackowski, L. Pinard, L. Dognin, P. Ganau, B. Lagrange, C. Michel, and M. Morgue, *Different approaches to improve the wavefront of low-loss mirrors used in the VIRGO gravitational wave antenna.* Optical Interference Coatings (Washington: Optical Society of America), 1998, pp. 18–20.

[99] H. A. Macleod, *Thin-Film Optical Filters, Fourth Edition.* CRC Press Taylor & Francis Group, 2010, ch. 13, Layer Uniformity and Thickness Monitoring.

[100] R. P. Riegert, *Optimum usage of quartz crystal monitor based devices.* IVth International Vacuum Congress (Manchester) (Bristol: Institute of Physics and the Physical Society), 1968, pp. 527–530.

[101] D. R. Gibson, I. Brinkley, E. M. Waddell, and J. M. Walls, "Closed field magnetron sputtering: new generation sputtering process for optical coatings," in *Proceedings of the SPIE*, vol. 7101, 2008, p. 12.

[102] D. Ristau, H. Ehlers, T. Gross, and M. Lappschies, "Optical broadband monitoring of conventional and ion processes," *Applied Optics*, vol. 45, pp. 1495–1501, 2006.

[103] D. Z. Anderson, J. C. Frisch, and C. S. Masser, "Mirror reflectometer based on optical cavity decay time," *Applied Optics*, vol. 23, pp. 1238–1245, 1984.

[104] W. H. Knox, N. M. Pearson, K. D. Li, and C. A. Hirlimann, "Interferometric measurements of femtosecond group delay in optical-components," *Optics Letters*, vol. 13, pp. 574–576, 1988.

[105] K. Naganuma, K. Mogi, and H. Yamada, "Group-delay measurement using the Fourier-transform of an interferometric cross-correlation generated by white-light," *Optics Letters*, vol. 15, pp. 393–395, 1990.

[106] W. H. Knox, "Dispersion measurements for femtosecond-pulse generation and applications," *Applied Physics B-lasers and Optics*, vol. 58, pp. 225–235, 1994.

[107] A. Gosteva, M. Haiml, R. Paschotta, and U. Keller, "Noise-related resolution limit of dispersion measurements with white-light interferometers," *Journal of the Optical Society of America B-optical Physics*, vol. 22, pp. 1868–1874, 2005.

[108] D. Grupe, "Measuring group delay dispersion in the UV-VIS-IR range by white-light interferometry," Master's thesis, Ludwig Maximilian University, Munich, 2008.

[109] T. V. Amotchkina, A. V. Tikhonravov, M. K. Trubetskov, D. Grupe, A. Apolonski, and V. Pervak, "Measurement of group delay of dispersive mirrors with white-light interferometer," *Applied Optics*, vol. 48, pp. 949–956, 2009.

[110] V. Pervak, C. Teisset, A. Sugita, S. Naumov, F. Krausz, and A. Apolonski, "High-dispersive mirrors for femtosecond lasers," *Optics Express*, vol. 16, pp. 10 220–10 230, 2008.

[111] P. Dombi, P. Racz, M. Lenner, V. Pervak, and F. Krausz, "Dispersion management in femtosecond laser oscillators with highly dispersive mirrors," *Optics Express*, vol. 17, pp. 20 598–20 604, 2009.

[112] V. Pervak, O. Pronin, O. Razskazovskaya, J. Brons, I. B. Angelov, M. K. Trubetskov, A. V. Tikhonravov, and F. Krausz, "High-dispersive mirrors for high power applications," *Optics Express*, vol. 20, pp. 4503–4508, 2012.

[113] C. R. E. Baer, C. Kraenkel, C. J. Saraceno, O. H. Heckl, M. Golling, R. Peters, K. Petermann, T. Südmeyer, G. Huber, and U. Keller, "Femtosecond thin-disk laser with 141 W of average power," *Optics Letters*, vol. 35, pp. 2302–2304, 2010.

[114] D. Bauer, I. Zawischa, D. H. Sutter, A. Killi, and T. Dekorsy, "Mode-locked Yb:YAG thin-disk oscillator with 41 μJ pulse energy at 145 W average infrared power and high power frequency conversion," *Optics Express*, vol. 20, 2012.

[115] A. A. Eilanlou, Y. Nabekawa, M. Kuwata-Gonokami, and K. Midorikawa, "Femtosecond laser pulses in a Kerr-lens mode-locked thin-disk ring oscillator with an intra-cavity peak power beyond 100 MW," *Japanese Journal of Applied Physics*, vol. 53, p. 082701, 2014.

[116] C. J. Saraceno, F. Emaury, C. Schriber, M. Hoffmann, M. Golling, T. Suedmeyer, and U. Keller, "Ultrafast thin-disk laser with 80 μJ pulse energy and 242 W of average power," *Optics Letters*, vol. 39, pp. 9–12, 2014.

[117] O. Pronin, J. Brons, C. Grasse, V. Pervak, G. Boehm, M. . C. Amann, V. L. Kalashnikov, A. Apolonski, and F. Krausz, "High-power 200 fs Kerr-lens mode-locked Yb:YAG thin-disk oscillator," *Optics Letters*, vol. 36, pp. 4746–4748, 2011.

[118] J. Zhang, J. Brons, N. Lilienfein, E. Fedulova, V. Pervak, D. Bauer, D. Sutter, Z. Wei, A. Apolonski, O. Pronin, and F. Krausz, "260-megahertz, megawatt-level thin-disk oscillator," *Optics Letters*, vol. 40, pp. 1627–1630, 2015.

[119] E. B. Treacy, "Optical pulse compression with diffraction gratings," *IEEE Journal of Quantum Electronics*, vol. QE 5, pp. 454–458, 1969.

[120] R. L. Fork, O. E. Martinez, and J. P. Gordon, "Negative dispersion using pairs of prisms," *Optics Letters*, vol. 9, pp. 150–152, 1984.

[121] J. Heppner and J. Kuhl, "Intracavity chirp compensation in a colliding pulse mode-locked laser using thin-film interferometers," *Applied Physics Letters*, vol. 47, pp. 453–455, 1985.

[122] B. Golubovic, R. R. Austin, M. K. Steiner-Shepard, M. K. Reed, S. A. Diddams, D. J. Jones, and A. G. Van Engen, "Double gires-tournois interferometer negative-dispersion mirrors for use in tunable mode-locked lasers," *Optics Letters*, vol. 25, pp. 275–277, 2000.

[123] R. Szipocs, A. Kohazi-Kis, S. Lako, P. Apai, A. P. Kovacs, G. DeBell, L. Mott, A. W. Louderback, A. V. Tikhonravov, and M. K. Trubetskov, "Negative dispersion mirrors for dispersion control in femtosecond lasers: chirped dielectric mirrors and multi-cavity Gires-Tournois interferometers," *Applied Physics B-lasers and Optics*, vol. 70, pp. S51–S57, 2000.

[124] R. L. Fork, C. H. B. Cruz, P. C. Becker, and C. V. Shank, "Compression of optical pulses to 6 femtoseconds by using cubic phase compensation," *Optics Letters*, vol. 12, pp. 483–485, 1987.

[125] S. Kane and J. Squier, "Grism-pair stretcher-compressor system for simultaneous second- and third-order dispersion compensation in chirped-pulse

amplification," *Journal of the Optical Society of America B-optical Physics*, vol. 14, pp. 661–665, 1997.

[126] N. Matuschek, F. X. Kärtner, and U. Keller, "Theory of double-chirped mirrors," *IEEE Journal of Selected Topics In Quantum Electronics*, vol. 4, pp. 197–208, 1998.

[127] G. Tempea, F. Krausz, C. Spielmann, and K. Ferencz, "Dispersion control over 150 THz with chirped dielectric mirrors," *IEEE Journal of Selected Topics In Quantum Electronics*, vol. 4, pp. 193–196, 1998.

[128] V. Pervak, I. Ahmad, S. A. Trushin, Z. Major, A. Apolonski, S. Karsch, and F. Krausz, "Chirped-pulse amplification of laser pulses with dispersive mirrors," *Optics Express*, vol. 17, pp. 19 204–19 212, 2009.

[129] V. Pervak, I. Ahmad, M. K. Trubetskov, A. V. Tikhonravov, and F. Krausz, "Double-angle multilayer mirrors with smooth dispersion characteristics," *Optics Express*, vol. 17, pp. 7943–7951, 2009.

[130] D. Strickland and G. Mourou, "Compression of amplified chirped optical pulses," *Optics Communications*, vol. 56, pp. 219–221, 1985.

[131] C. E. Barrera, J. Martinez-Flores, G. Gonzalez, M. Ortega-Lopez, and R. Rosas, "Spectroscopic ellipsometry study of Co_3O_4 thin films deposited on several metal substrates," *The Open Surface Science Journal*, pp. 9–16, 2013.

[132] "ULE® corning code 7972 ultra low expansion glass," https://www.corning.com/media/worldwide/csm/documents/D20FD2EA-7264-43DD-B544-E1CA042B486A.pdf.

[133] "Zerodur® extremely low expansion glass ceramic," http://www.schott.com/advanced_optics/english/products/optical-materials/zerodur-extremely-low-expansion-glass-ceramic/zerodur/index.html.

[134] D. R. Lide, *Handbook of chemistry and physics*. CRC press, 2004.

[135] "Good fellow," http://www.goodfellow.com/.

[136] "Hukseflux thermal sensors," http://www.hukseflux.com/page/products-services.

[137] "Almaz optics, inc." http://www.almazoptics.com/sapphire.htm.

[138] J. Dean, *Lange's handbook of chemistry*. McGraw Hill Book Co.,New York, NY, 1985.

[139] P. Becker, P. Seyfried, and H. Siegert, "The lattice-parameter of highly pure silicon single-crystals," *Zeitschrift für Physik B Condensed Matter*, vol. 48, pp. 17–21, 1982.

[140] H. E. Bennett and J. O. Porteus, "Relation between surface roughness and specular reflectance at normal incidence," *Journal of the Optical Society of America*, vol. 51, pp. 123–129, 1961.

[141] J. E. Harvey, S. Schroeder, N. Choi, and A. Duparre, "Total integrated scatter from surfaces with arbitrary roughness, correlation widths, and incident angles," *Optical Engineering*, vol. 51, p. 013402, 2012.

[142] V. Pervak, V. Fedorov, Y. A. Pervak, and M. Trubetskov, "Empirical study of the group delay dispersion achievable with multilayer mirrors," *Optics Express*, vol. 21, pp. 18 311–18 316, 2013.

[143] V. Pervak, M. K. Trubetskov, and A. V. Tikhonravov, "Robust synthesis of dispersive mirrors," *Optics Express*, vol. 19, pp. 2371–2380, 2011.

[144] K. Fritsch, "Mode-locking with ultra-high dispersive mirrors and novel multilayer structures," Master's thesis, Ludwig-Maximilian Universität München, 2015, (in German).

[145] O. Razskazovskaya, T. T. Luu, M. Trubetskov, E. Goulielmakis, and V. Pervak, "Nonlinear absorbance in dielectric multilayers," *Optica*, vol. 2, pp. 803–811, 2015.

[146] C. Rodriguez, S. Guenster, D. Ristau, and W. Rudolph, "Frequency tripling mirror," *Optics Express*, vol. 23, pp. 31 594–31 601, 2015.

[147] K. Starke, D. Ristau, H. Welling, T. V. Amotchkina, M. K. Trubetskov, A. A. Tikhonravov, and A. S. Chirkin, "Investigations in the nonlinear behavior of dielectrics by using ultrashort pulses," *Proceedings of SPIE*, vol. 5273, pp. 501–514, 2003.

[148] W. Chen and D. L. Mills, "Optical-response of nonlinear multilayer structures - bilayers and superlattices," *Physical Review B*, vol. 36, pp. 6269–6278, 1987.

[149] E. Lidorikis, Q. M. Li, and C. M. Soukoulis, "Wave propagation in nonlinear multilayer structures," *Physical Review B*, vol. 54, pp. 10 249–10 252, 1996.

[150] L. Brzozowski and E. H. Sargent, "Optical signal processing using nonlinear distributed feedback structures," *IEEE Journal of Quantum Electronics*, vol. 36, pp. 550–555, 2000.

[151] P. K. Kwan and Y. Y. Lu, "Computing optical bistability in one-dimensional nonlinear structures," *Optics Communications*, vol. 238, pp. 169–175, 2004.

[152] N. Moshonas, G. K. Pagiatakis, P. Papagiannis, S. P. Savaidis, and N. A. Stathopoulos, "Simulation and properties of highly nonlinear multilayer optical structures using the transmission line method," *Proc. SPIE Optical Modelling and Design III*, vol. 9131, pp. 913 129–1–913 129–11, 2014.

[153] R. Adair, L. L. Chase, and S. A. Payne, "Nonlinear refractive-index of optical-crystals," *Physical Review B*, vol. 39, pp. 3337–3350, 1989.

[154] V. Dimitrov and S. Sakka, "Linear and nonlinear optical properties of simple oxides. 2." *Journal of Applied Physics*, vol. 79, pp. 1741–1745, 1996.

[155] E. Fedulova, M. Trubetskov, T. Amotchkina, K. Fritsch, P. Baum, O. Pronin, and V. Pervak, "Kerr effect in multilayer dielectric coatings," *Optica*, 2016, submitted.

[156] M. Sheik-Bahae, D. J. Hagan, and E. W. Vanstryland, "Dispersion and bandgap scaling of the electronic Kerr effect in solids associated with 2-photon absorption," *Physical Review Letters*, vol. 65, pp. 96–99, 1990.

[157] R. Paschotta, *article on 'nonlinear index' in the Encyclopedia of Laser Physics and Technology, 1. edition.* Wiley-VCH, ISBN 978-3-527-40828-3, October 2008.

[158] "Refractive index database," http://refractiveindex.info/.

[159] M. Evans, "Recent development in thermo-optic noise," Tech. Rep. La Biodola, Isola d'Elba, Italy, 2008, technical report.

[160] M. Mero, J. H. Liu, A. Sabbah, J. Jasapara, K. Starke, D. Ristau, J. K. McIver, and W. Rudolph, "Femtosecond pulse damage and pre-damage behavior of dielectric thin films," *Proc. SPIE 4932, Laser-Induced Damage in Optical Materials: 2002 and 7th International Workshop on Laser Beam and Optics Characterization*, vol. 4932, pp. 202–215, 2002.

[161] J. Liu, D. Xue, and K. Li, "Single-crystalline nanoporous Nb_2O_5 nanotubes," *Nanoscale Research Letters*, vol. 6, p. 138, 2011.

[162] J. Sancho-Parramon, V. Janicki, and H. Zorc, "Compositional dependence of absorption coefficient and band-gap for Nb_2O_5-SiO_2 mixture thin films," *Thin Solid Films*, vol. 516, pp. 5478–5482, 2008.

[163] C. Y. Tai, J. S. Wilkinson, N. M. B. Perney, M. C. Netti, F. Cattaneo, C. E. Finlayson, and J. J. Baumberg, "Determination of nonlinear refractive index in a Ta_2O_5 rib waveguide using self-phase modulation," *Optics Express*, vol. 12, pp. 5110–5116, 2004.

[164] E. Bersch, S. Rangan, R. A. Bartynski, E. Garfunkel, and E. Vescovo, "Band offsets of ultrathin high-kappa oxide films with Si," *Physical Review B*, vol. 78, p. 085114, 2008.

[165] J. P. Chang, Y. S. Lin, and K. Chu, "Rapid thermal chemical vapor deposition of zirconium oxide for metal-oxide-semiconductor field effect transistor application," *Journal of Vacuum Science & Technology B*, vol. 19, p. AVS, 2001.

[166] B. P. Nelson, K. J. Blow, P. D. Constantine, N. J. Doran, J. K. Lucek, I. W. Marshall, and K. Smith, "All-optical gbit/s switching using nonlinear optical loop mirror," *Electronics Letters*, vol. 27, pp. 704–705, 1991.

[167] D. Rafieian, W. Ogieglo, T. Savenije, and R. G. H. Lammertink, "Controlled formation of anatase and rutile tio2 thin films by reactive magnetron sputtering," *Aip Advances*, vol. 5, p. 097168, 2015.

[168] E. Franke, C. L. Trimble, M. J. DeVries, J. A. Woollam, M. Schubert, and F. Frost, "Dielectric function of amorphous tantalum oxide from the far infrared to the deep ultraviolet spectral region measured by spectroscopic ellipsometry," *Journal of Applied Physics*, vol. 88, pp. 5166–5174, 2000.

[169] I. B. Angelov, A. von Conta, S. A. Trushin, Z. Major, S. Karsch, F. Krausz, and V. Pervak, "Investigation of the laser-induced damage in dispersive coatings," *Proceeding of SPIE: Laser-induced Damage In Optical Materials*, vol. 8190, pp. 81 900B–1 – 81 900B–6, 2011.

[170] L. W. Tutt and T. F. Boggess, "A review of optical limiting mechanisms and devices using organics, fullerenes, semiconductors and other materials," *Progress In Quantum Electronics*, vol. 17, pp. 299–338, 1993.

[171] Q. Lin, O. J. Painter, and G. P. Agrawal, "Nonlinear optical phenomena in silicon waveguides: Modeling and applications," *Optics Express*, vol. 15, pp. 16 604–16 644, 2007.

[172] J. Leuthold, C. Koos, and W. Freude, "Nonlinear silicon photonics," *Nature Photonics*, vol. 4, pp. 535–544, 2010.

[173] C. Koos, L. Jacome, C. Poulton, J. Leuthold, and W. Freude, "Nonlinear silicon-on-insulator waveguides for all-optical signal processing," *Optics Express*, vol. 15, pp. 5976–5990, 2007.

[174] E. C. Maegi, L. B. Fu, H. C. Nguyen, M. R. E. Lamont, D. I. Yeom, and B. J. Eggleton, "Enhanced Kerr nonlinearity in sub-wavelength diameter As_2Se_3 chalcogenide fiber tapers," *Optics Express*, vol. 15, pp. 10 324–10 329, 2007.

[175] L. Waldecker, T. A. Miller, M. Rude, R. Bertoni, J. Osmond, V. Pruneri, R. E. Simpson, R. Ernstorfer, and S. Wall, "Time-domain separation of optical properties from structural transitions in resonantly bonded materials," *Nature Materials*, vol. 14, pp. 991–995, 2015.

[176] J. Hsu, C. Fuentes-Hernandez, A. R. Ernst, and B. Kippelen, "Ultrafast nonlinear mirrors with broad spectral and angular bandwidths in the visible spectral range," *Optics Express*, vol. 21, pp. 3573–3581, 2013.

[177] W. Schneider, A. Ryabov, C. Lombosi, T. Metzger, Z. Major, J. A. Fulop, and P. Baum, "800-fs, 330-μJ pulses from a 100-W regenerative Yb:YAG thin-disk amplifier at 300 kHz and THz generation in $LiNbO_3$," *Optics Letters*, vol. 39, pp. 6604–6607, 2014.

[178] D. Du, X. Liu, G. Korn, J. Squier, and G. Mourou, "Laser-induced breakdown by impact ionization in SiO_2 with pulse widths from 7 ns to 150 fs," *Applied Physics Letters*, vol. 64, pp. 3071–3073, 1994.

[179] B. C. Stuart, M. D. Feit, A. M. Rubenchik, B. W. Shore, and M. D. Perry, "Laser-induced damage in dielectrics with nanosecond to subpicosecond pulses," *Physical Review Letters*, vol. 74, pp. 2248–2251, 1995.

[180] M. Lenzner, F. Krausz, J. Kruger, and W. Kautek, "Photoablation with sub-10 fs laser pulses," *Applied Surface Science*, vol. 154, pp. 11–16, 2000.

[181] C. B. Schaffer, A. Brodeur, and E. Mazur, "Laser-induced breakdown and damage in bulk transparent materials induced by tightly focused femtosecond laser pulses," *Measurement Science & Technology*, vol. 12, pp. 1784–1794, 2001.

[182] M. Mero, B. Clapp, J. C. Jasapara, W. Rudolph, D. Ristau, K. Starke, J. Kruger, S. Martin, and W. Kautek, "On the damage behavior of dielectric films when illuminated with multiple femtosecond laser pulses," *Optical Engineering*, vol. 44, pp. 051 107–1–051 107–7, 2005.

[183] D. Nguyen, L. A. Emmert, I. V. Cravetchi, M. Mero, W. Rudolph, M. Jupe, M. Lappschies, K. Starke, and D. Ristau, "$Ti_xSi_{1-x}O_2$ optical coatings with tunable index and their response to intense subpicosecond laser pulse irradiation," *Applied Physics Letters*, vol. 93, p. 261903, 2008.

[184] A. Melninkaitis, J. Mirauskas, and V. Sirutkaitis, "Adaptive laser-induced damage detection," in *Proceedings of SPIE, Laser-Induced Damage in Optical Materials*, vol. 7504, 2009.

[185] I. B. Angelov, M. von Pechmann, M. K. Trubetskov, F. Krausz, and V. Pervak, "Optical breakdown of multilayer thin-films induced by ultrashort pulses at MHz repetition rates," *Optics Express*, vol. 21, pp. 31 453–31 461, 2013.

[186] J. Bonse, S. Baudach, J. Kruger, W. Kautek, K. Starke, T. Gross, D. Ristau, W. Rudolph, J. Jasapara, and E. Welsch, "Femtosecond laser damage in dielectric coatings," *Laser-induced Damage In Optical Materials: 2000, Proceedings of SPIE*, vol. 4347, pp. 24–34, 2001.

[187] M. Mero, A. J. Sabbah, J. Zeller, and W. Rudolph, "Femtosecond dynamics of dielectric films in the pre-ablation regime," *Applied Physics A-materials Science & Processing*, vol. 81, pp. 317–324, 2005.

[188] I. B. Angelov, "Development of high-damage threshold dispersive coatings," Ph.D. dissertation, Ludwig-Maximilian University, Munich, 2014.

[189] A. Zukauskas, A. Melninkaitis, and V. Sirutkaitis, "Nonlinear absorption of ultrashort pulses in HR dielectric mirrors," *Proceedings of SPIE*, vol. 5991, pp. 599 111–1 – 599 111–10, 2005.

[190] M. Konuma, "Plasma techniques for film deposition," Ph.D. dissertation, Alpha Science, Harrow, UK, 2005.

[191] S. C. Jones, P. Braunlich, R. T. Casper, X. A. Shen, and P. Kelly, "Recent progress on laser-induced modifications and intrinsic bulk damage of wide-gap optical-materials," *Optical Engineering*, vol. 28, pp. 1039–1068, 1989.

[192] S. Guizard, P. Martin, G. Petite, P. DOliveira, and P. Meynadier, "Time-resolved study of laser-induced colour centres in SiO_2," *Journal of Physics-condensed Matter*, vol. 8, pp. 1281–1290, 1996.

[193] A. Mouskeftaras, S. Guizard, N. Fedorov, and S. Klimentov, "Mechanisms of femtosecond laser ablation of dielectrics revealed by double pump-probe experiment," *Applied Physics A-materials Science & Processing*, vol. 110, pp. 709–715, 2013.

[194] D. N. Nguyen, L. A. Emmert, M. Mero, and W. Rudolph, "The effect of annealing on the subpicosecond breakdown behavior of hafnia films," *Proceedings of SPIE*, vol. 7132, pp. 71 320N–1, 2008.

[195] L. A. Emmert, M. Mero, and W. Rudolph, "Modeling the effect of native and laser-induced states on the dielectric breakdown of wide band gap optical materials by multiple subpicosecond laser pulses," *Journal of Applied Physics*, vol. 108, p. 043523, 2010.

[196] P. A. Tipler and G. Mosca, Eds., *Physics for Scientists and Engineers, Volume 1*, 6th ed. New York, NY: Worth Publishers, 2008, pp. 666–670.

[197] J. Franc, N. Morgado, R. Flaminio, R. Nawrodt, I. Martin, L. Cunningham, A. Cumming, S. Rowan, and J. Hough, "Mirror thermal noise in laser interferometer gravitational wave detectors operating at room and cryogenic temperature," Tech. Rep. General Relativity and Quantum Cosmology, 2009.

[198] M. L. Gorodetsky, "Thermal noises and noise compensation in high-reflection multilayer coating," *Physics Letters A*, vol. 372, pp. 6813–6822, 2008.

[199] S. Rao, "Mirror thermal noise in interferometric gravitational waves detectors," Ph.D. dissertation, Caltech., University of California, 2003.

[200] T.-C. Chen, C.-J. Chu, C.-H. Ho, C.-C. Wu, and C.-C. Lee, "Determination of stress-optical and thermal-optical coefficients of Nb_2O_5 thin film material," *Journal of Applied Physics*, vol. 101, p. 043513, 2007.

[201] C. L. Tien, C. C. Jaing, C. C. Lee, and K. P. Chuang, "Simultaneous determination of the thermal expansion coefficient and the elastic modulus of Ta_2O_5 thin film using phase shifting interferometry," *Journal of Modern Optics*, vol. 47, pp. 1681–1691, 2000.

[202] A. von Conta, "Characterization of the laser induced damage threshold of mirrors in the ultra short pulse regime," Bachelor Thesis, Hochschule München, 2010.

[203] B. C. Stuart, M. D. Feit, S. Herman, A. M. Rubenchik, B. W. Shore, and M. D. Perry, "Nanosecond-to-femtosecond laser-induced breakdown in dielectrics," *Physical Review B*, vol. 53, pp. 1749–1761, 1996.

[204] M. Lenzner, J. Kruger, S. Sartania, Z. Cheng, C. Spielmann, G. Mourou, W. Kautek, and F. Krausz, "Femtosecond optical breakdown in dielectrics," *Physical Review Letters*, vol. 80, pp. 4076–4079, 1998.

[205] A. Rosenfeld, M. Lorenz, R. Stoian, and D. Ashkenasi, "Ultrashort-laser-pulse damage threshold of transparent materials and the role of incubation," *Applied Physics A-materials Science & Processing*, vol. 69, pp. S373–S376, 1999.

[206] C. Itoh, K. Tanimura, and N. Itoh, "Optical studies of self-trapped excitons in SiO_2," *Journal of Physics C-solid State Physics*, vol. 21, pp. 4693–4702, 1988.

[207] A. M. Stoneham, J. Gavartin, A. L. Shluger, A. V. Kimmel, D. M. Ramo, H. M. Ronnow, G. Aeppli, and C. Renner, "Trapping, self-trapping and the polaron family," *Journal of Physics-condensed Matter*, vol. 19, 2007.

[208] K. Tanimura, T. Tanaka, and N. Itoh, "Creation of quasistable lattice-defects by electronic excitation in SiO_2," *Physical Review Letters*, vol. 51, pp. 423–426, 1983.

[209] R. T. Williams, "Optically generated lattice-defects in halide crystals," *Optical Engineering*, vol. 28, pp. 1024–1033, 1989.

[210] A. Hertwig, S. Martin, J. Kruger, and W. Kautek, "Surface damage and color centers generated by femtosecond pulses in borosilicate glass and silica," *Applied Physics A-materials Science & Processing*, vol. 79, pp. 1075–1077, 2004.

[211] L. A. Emmert, C. Rodriguez, Z. Sun, F. B. A. Aghbolagh, S. Guenster, D. Ristau, D. Patel, C. M. Menonic, and W. Rudolph, "Optical coatings excited by femtosecond lasers near the damage threshold: Challenges and opportunities," *Laser-induced Damage In Optical Materials*, vol. 9632, pp. 96 320K–1 – 96 320K–9, 2015.

[212] A. C. Tien, S. Backus, H. Kapteyn, M. Murnane, and G. Mourou, "Short-pulse laser damage in transparent materials as a function of pulse duration," *Physical Review Letters*, vol. 82, pp. 3883–3886, 1999.

[213] C. W. Luo, Y. T. Wang, F. W. Chen, H. C. Shih, and T. Kobayashi, "Eliminate coherence spike in reflection-type pump-probe measurements," *Optics Express*, vol. 17, pp. 11 321–11 327, 2009.

[214] M. Mero, "Femtosecond laser induced breakdown in dielectric films," Ph.D. dissertation, The University of New Mexico, 2005.

[215] Z. Vardeny and J. Tauc, "Picosecond coherence coupling in the pump and probe technique," *Optics Communications*, vol. 39, pp. 396–400, 1981.

[216] B. S. Wherrett, A. L. Smirl, and T. F. Boggess, "Theory of degenerate four-wave mixing in picosecond excitation-probe experiments," *IEEE Journal of Quantum Electronics*, vol. 19, pp. 680–690, 1983.

[217] S. L. Palfrey and T. F. Heinz, "Coherent interactions in pump-probe absorption-measurements – the effect of phase gratings," *Journal of the Optical Society of America B-optical Physics*, vol. 2, pp. 674–679, 1985.

[218] G. Cerullo, C. Manzoni, L. Luer, and D. Polli, "Time-resolved methods in biophysics. 4. broadband pump-probe spectroscopy system with sub-20 fs temporal resolution for the study of energy transfer processes in photosynthesis," *Photochemical & Photobiological Sciences*, vol. 6, pp. 135–144, 2007.

[219] U. Keller, W. H. Knox, and G. W. 't Hooft, "Ultrafast solid-state mode-locked lasers using resonant nonlinearities," *IEEE Journal of Quantum Electronics*, vol. 28, pp. 2123–2133, 1992.

[220] U. Keller, K. J. Weingarten, F. X. Kärtner, D. Kopf, B. Braun, I. D. Jung, R. Fluck, C. Honninger, N. Matuschek, and J. A. derAu, "Semiconductor saturable absorber mirrors (SESAM's) for femtosecond to nanosecond pulse generation in solid-state lasers," *IEEE Journal of Selected Topics In Quantum Electronics*, vol. 2, pp. 435–453, 1996.

[221] K. G. Wilcox, Z. Mihoubi, S. Elsmere, A. Quarterman, H. D. Foreman, S. Hashimoto, T. Südmeyer, U. Keller, and A. Tropper, "Passively mode-locked 832 nm vertical-external-cavity surface-emitting semiconductor laser producing 15.3 ps pulses at 1.9 GHz repetition rate," *Electronics Letters*, vol. 44, pp. 1469 –1470, 2008.

[222] M. Mero, J. Liu, W. Rudolph, D. Ristau, and K. Starke, "Scaling laws of femtosecond laser pulse induced breakdown in oxide films," *Physical Review B*, vol. 71, p. 115109, 2005.

[223] P. Martin, S. Guizard, P. Daguzan, G. Petite, P. D'Oliveira, P. Meynadier, and M. Perdrix, "Subpicosecond study of carrier trapping dynamics in wide-band-gap crystals," *Physical Review B*, vol. 55, pp. 5799–5810, 1997.

Data archiving

The experimental raw data, evaluation files, and original figures can be found on the Data Archive Server of the Laboratory for Attosecond Physics at the Max Planck Institute of Quantum Optics: /afs/rzg/mpq/lap/publication_archive.

The data is organized with respect to the chapters and sections of the thesis. All original figures are named fig_xx-xx_text, where xx-xx corresponds to the figure number in the thesis and _text gives a short figure caption. A text file within each folder named ChapterX.docx or ChapterX_SectionY.docx (X/Y being the chapter/section number) gives detailed information for the figures contained in the according chapter (section of that chapter) in the order of appearance. These text files describe the organization and format of the raw data, as well as the processing, evaluation or simulation performed in order to obtain the final figure.

List of publications

Publications in refereed journals

E. Fedulova, M. Trubetskov, T. Amotchkina, K. Fritsch, P. Baum, O. Pronin, and V. Pervak. *Kerr effect in multilayer dielectric coatings.* Optics Express **24**, 21802-21817 (2016).

E. Fedulova, K. Fritsch, J. Brons, O. Pronin, T. Amotchkina, M. Trubetskov, F. Krausz and V. Pervak. *Highly-dispersive mirrors reach new levels of dispersion.* Optics Express **23**, 13788−13793 (2015).

O. Pronin, M. Seidel, F. Lücking, J. Brons, **E. Fedulova**, M. Trubetskov, V. Pervak, A. Apolonski, T. Udem and F. Krausz. *High-power multi-megahertz source of waveform-stabilized few-cycle light.* Nature Communications **6**, 6988 (2015).

J. Zhang, J. Brons, N. Lilienfein, **E. Fedulova**, V. Pervak, D. Bauer, D. Sutter, Z. Wei, A. Apolonski, O. Pronin, and F. Krausz. *260-megahertz, megawatt-level thin-disk oscillator.* Optics Letters **40**, 1627−1630 (2015).

J. Brons, V. Pervak, **E. Fedulova**, D. Bauer, D. Sutter, V. Kalashnikov, A. Apolonskiy, O. Pronin, and F. Krausz. *Energy scaling of Kerr-lens mode-locked thin-disk oscillators.* Optics Letters **39**, 6442-6445 (2014).

Proceedings of refereed conferences

E. Fedulova, K. Fritsch, J. Brons, O. Pronin, T. Amotchkina, M. Trubetskov, F. Krausz, and V. Pervak. **Oral talk***: New levels of dispersion of highly dispersive mirrors.* In Advanced Solid State Lasers, OSA Technical Digest (online), paper ATu3A.8, (Optical Society of America, 2015).

M. Seidel, J. Brons, **E. Fedulova**, V. Pervak, A. Apolonski, O. Pronin, and F. Krausz. *High-power few-cycle pulse generation by spectral broadening in bulk material.* In CLEO: 2014 Postdeadline Paper Digest, OSA Technical Digest (online), paper STh5C.9, (Optical Society of America, 2014).

J. Brons, V. Pervak, **E. Fedulova**, M. Seidel, D. Bauer, D. Sutter, V. Kalashnikov, A. Apolonski, O. Pronin, and F. Krausz. *Power-scaling a Kerr-lens mode-locked Yb:YAG thin-disk oscillator via enlarging the cavity mode in the Kerr-medium.* In CLEO: 2014, OSA Technical Digest (online), paper SM4F.7, (Optical Society of America, 2014).

O. Pronin, J. Brons, M. Seidel, **E. Fedulova**, A. A. Apolonskiy, D. Bauer, D. Sutter, V. Kalashnikov, V. Pervak, F. Krausz. *Power and energy scaling of Kerr-lens mode-locked thin-disk oscillators.* In Conference SPIE Photonics Europe, published in SPIE Proceedings Vol. 9135: Laser Sources and Applications II, 91351H (2014).

S. Keiber, T. Paasch-Colberg, A. Schwarz, O. Razskazovskaya, **E. Fedulova**, Ö. Sağlam, C. Jakubeit, S. Sederberg, P. Dombi, N. Karpowicz, and F. Krausz. *Investigation of Laser-Induced Currents in Large-Band-Gap Dielectrics.* In 19th International Conference on Ultrafast Phenomena, OSA Technical Digest (online), paper 10.Thu.C.6, (Optical Society of America, 2014).

M. Seidel, O. Pronin, J. Brons, **E. Fedulova**, F. Lücking, I. Angelov, V. Pervak, A. Apolonski, and F. Krausz, *Approaching the Few-Cycle Pulse Regime with Thin-Disk Oscillators.* In Advanced Solid-State Lasers Congress, G. Huber and P. Moulton, eds., OSA Technical Digest (online), paper ATu4A.7, (Optical Society of America, 2013).

M. K. Trubetskov, M. von Pechmann, I. Angelov, **E. Fedulova**, F. Krausz, V. Pervak. *Group Delay Dispersion Measurements with Resonance Scanning Interferometry.* In Optical Interference Coatings, M. Tilsch and D. Ristau, eds., OSA Technical Digest (online), paper WD.3, (Optical Society of America, 2013).

D. Franz, H. Fattahi, V. Pervak, M. Trubetskov, **E. Fedulova**, N. Karpowicz, Z. Major, F. Krausz. *Investigation of temporal compression of few-cycle pulses from an ultrabroadband, multi-mJ optical parametric amplifier.* In Conference on Lasers & Electro-Optics Europe & International Quantum Electronics Conference CLEO EUROPE/IQEC (2013).

Patents

The pending patent application regarding NMCs will be published in September 2017.

Acknowledgments

First of all, my thanks go to my Doktorvater Professor Ferenc Krausz for giving me this wonderful opportunity to execute a PhD study in his outstanding group and to see how powerful and resourceful the scientific research can be. It was a great experience working in the LAP team among highly motivated and knowledgeable people, who were always ready to help. Ein großes Dankeschön geht auch an liebe Angela Krausz, eine sehr handwerklich begabte Vermieterin. Du hast mein Leben hier viel leichter gemacht!

I would like to thank Professor Jörg Schreiber for agreeing to review my thesis, even though it was quite a short notice to start with. I am deeply grateful to my mentor Dr. Vladimir Pervak, who offered me the PhD position and kindly kept me after the first three trial months for four more years. Vladimir has let me to find a balance between freedom and responsibility in planning and conducting the research, which I truly appreciate. Also, a difficult task of preparing a presentation was much lightened by Vladimir's feedback and advises. He also gave me valuable constructive feedback for improving my dissertation. Thank you for your motivation, support and all the ideas that constantly pushed the experiments forward. Together with Olga Razskazovskaya, Andrey Ryabov and Frau Wild, you helped me to adjust to a completely unknown and scary at the time of my arrival country.

I am also indebted to the members, former and present, of our coating team, without whom this thesis would not have existed. Thank you Olga, for sharing your both life and scientific experience with me. Thank you Maximilian von Pechmann, for our experimental work together in the lab, and for being such a cutie pie. Thank you Ivan Angelov, for explaining a lot of different things to me, over and over, and for being such a good suasible flat mate. Thank you Florian Habel, for all your helpful work-related advises and our non-work-related discussions, and for being such an inspiring perennial spring of curiosity. Also, many thanks for translating the abstract! Thank you Dr. Mikhail Trubetskov, for many fruitful discussions and innovative ideas, that always arrived just on time in moments of stagnation. Thank you Dr. Tatiana Amotchkina, for appearing at the end of my PhD journey and rising so many valuable questions, that shed light on many issues.

You have tremendously helped me with writing the MAM paper, and consequently my thesis. Endlich, bedanke ich mich auch bei Bernd und Sigi, die viele technishe Unterstützung gemacht haben. It was a pleasure working with all of you!

I am infinitely grateful to Dr. Oleg Pronin, who introduced me to the lab and incommensurably helped me during my PhD studies: your dedication and push made this work successful. Through your example, I was able to see how charming working late into the night is. I am very thankful to Oleg's team (especially to Kilian Fritsch, Marcus Seidel, Jonathan Brons, Jinwei Zhang and Kafai Mak) for always being happy to help.

Special thanks go to the group of Dr. Peter Baum and Peter Baum himself, for providing and untiringly maintaining the laser source at different times: Waldemar Schneider, Andrey Ryabov, Dominik Ehberger and Catherine Kealhofer. Thank you and the rest of the UED group for a nice environment in the lab, which I barbarously occupied. I am also grateful to Peter for improving (read: re-writing) the abstract and the introduction of my second paper. Also, thanks to a very kind and helpful person, hiding inside of Alex Gliserin, for his help with CorelDraw. I know what you would call the pictures presented here, but you will have to live with the thought that they exist due to you anyway. I am very grateful to Christian Kreuzer, who helped me a lot with AFM measurements and explained to me what exactly my second referee is doing.

Thanks to various people for being great office mates: Mikhail Trubetskov, Olga Razskazovskaya, Daniel Kreier, Simon Holzberger, Yuya Morimoto, Waldemar Schneider, Matthias Kübel and Ernst Fill (the latter three being even too great as it appeared). Also, thank you Simon, whose heart is as big as his ears, for all the arguing and gossiping we had!

I also recognize the work of Klaus Franke, Katharina Adler and Martin Gross, who daily process unmeasurable amount of documents for us. Thanks to our Werkstatt and Herr Öhm, who heroically deals with all kinds of awful German speakers. Speaking of which, I would like to thank all the Germans who I occasionally forced to be my Ansprechpartners!

I am also grateful to all the LMU building inhabitants for always willing to lend any equipment and bring all those delicious "cake-like objects". Further, it was super cool to get to know all you Beer O'Clock participants: Smatt Waldbrand, Chancellor Kerrie Peache, Henning the Fishkopf, Simon the Seaman, Niko the Huge, Heinrich the Acetone Fiend, Dominik Dreheberger the Nominator, Nora the Black Hole, Tobi the Purple and Rich, Marinus the Night-Boat-Knight, Catherine the Cold, Christian the Jendrzejewski-Burger and many others. That is how I will

remember you! Thank you guys for helping me out when needed, for having loads of fun and showing me that foreigners are not as foreign as I stereotypically used to imagine.

I am very happy to have gotten to know Maria Meng, Kellie Pearce, Lamia (Kanga) Kasmi and Matt Walbran, who became my small family here. Also, I owe a special debt of gratitude to Matt, a weirdo who not only was asked to but also chose to proof read all my writing during my PhD time. Chur, bro! All H, eh!

I cannot imagine being surrounded by a better group of people, than the Krausz group!

I am also thankful to my mentors Dr. Maxim Nazarov and Prof. Alexander Shkurinov from Moscow State University, under whose supervision my CV became so good, that I could make it here, to Max Planck Institute for Quantum Optics.

Спасибо моим родным за любовь, поддержку и понимание. Спасибо вам, мои дорогие родители, за то, что не побоялись отпустить меня в другую страну. Молодцы, что освоили скайп и научились писать электронные письма, и спасибо, что не обижались когда ваша пропащая дочь долго не выходила на связь. Здорово, что приехала навестить меня, моя любимая сестрича! И привезла все то, что тут не купить. Было очень круто и интересно съездить в "Нойшвайнштайн" с тобою.

I am grateful to many other people who I met during the past years.

All of you, mentioned and not mentioned here, have considerably contributed to my life development :)